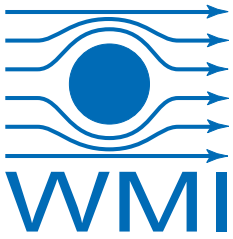

Scanning Microscopy and Momentum-Resolved Raman Scattering in Semiconductors and Oxides

Dissertation

Nitin Chelwani

May 2018

Fakultät für Physik
Technische Universität München

TECHNISCHE UNIVERSITÄT MÜNCHEN

Fakultät für Physik
Lehrstuhl E23 für Technische Physik

Walther-Meißner-Institut für Tieftemperaturforschung
der Bayerischen Akademie der Wissenschaften

Scanning Microscopy and Momentum-Resolved Raman Scattering in Semiconductors and Oxides

Nitin Chelwani

Vollständiger Abdruck der von der Fakultät für Physik der Technischen Universität München zur Erlangung des akademischen Grades eines

Doktors der Naturwissenschaften

genehmigten Dissertation.

Vorsitzender:		Prof. Dr. Martin Zacharias
Prüfer der Dissertation:	1.	Prof. Dr. Rudolf Gross
	2.	Prof. Christian Pfleiderer, Ph.D.

Die Dissertation wurde am 09.05.2018 bei der
Technischen Universität München eingereicht und durch
die Fakultät für Physik am 07.08.2018 angenommen.

To my Bhagwanji and Didiji

Abstract

This thesis comprises the description of the development of a set-up for tip-enhanced Raman spectroscopy and a comparative study of the Raman response of three CuO_2-based compounds as prototypical spin 1/2 antiferromagnets. The major innovation of the optical configuration is an off-axis parabolic mirror, the advantages and potential challenges of which were explored in detail. The symmetry-resolved spectra indicate that the line shape in B_{1g} symmetry is universal and independent of the excitation energy.

Kurzzusammenfassung

Diese Arbeit beschreibt Entwicklung und Aufbau einer Apparatur zur spitzenverstärkten Raman-Spektroskopie und eine Studie, in der die Raman-Spektren dreier Verbindungen auf CuO_2 Basis als prototypische Spin-1/2 Antiferromagneten verglichen werden. Die zentrale Innovation des Aufbaus besteht aus einem außeraxialen Parabolspiegel, dessen Herausforderungen und Chancen im Detail untersucht wurden. Die nach Symmetriekomponenten zerlegten Spektren zeigen, dass die Linienform der B_{1g} Raman-Spektren universell und unabhängig von der Anregungsenergie ist.

Contents

Chapter 1

Introduction

Inelastic light (Raman) scattering is an intensively used technique for the study of elementary excitations in solids including phonons, electron-hole pairs, and magnons. The studies include high-T_c superconductivity [1, 2], magnetism [3, 4], and semiconductor physics [5]. In superconductors, for instance, the energy gap, its anisotropies and momentum dependences of the pairing potential can be probed [6–8]. In magnets spin excitations were studied early, and a great deal of attention was paid on the cuprates [9–13]. Yet the full explanation of the line shape was only partially successful [14–16] calling for new ideas and higher spectral resolution in the experiments.

Spatial resolution is less important at first glance since most of the superconductors or magnets are considered to be rather homogeneous. However, scanning tunneling spectroscopy [17, 18] revealed nanometer scale inhomogeneities of the superconducting gap of $Bi_2Sr_2CaCu_2O_8$. More recently anomalously high conductivity was found close to grain boundaries in WO_{3-x} [19] and nanometer-sized topological objects were discovered in magnets [20]. These results show the demand for the improvement of the optical resolution beyond the diffraction limit of light, thereby accessing nano-scale spectroscopic fingerprints which may otherwise remain hidden.

Tip-enhanced Raman spectroscopy (TERS), developed about two decades ago, is a spectroscopic extension of scanning probe microscopy which provides a new avenue to access these spectroscopic fingerprints alongside the topographic information in the sub-wavelength regime [21–24]. Since the first experimental realization [25, 26], TERS has made a rapid progress to become a promising nanoscale characterization tool. New insights into the properties of molecular systems [23, 27], carbon based nanomaterials [28–30], and crystalline samples [23, 31] could be obtained.

TERS is an established technique for the near-field studies in ambient conditions.

However, TERS experiments at low temperatures are still in their infancy [31–33]. Our aim is to develop TERS with an alternative optical geometry designed to be applicable in the temperature range of 10 K−300 K. Furthermore, we aim to utilize our customized setup to study the dynamics of charge, spin, and lattice excitations in bulk crystals with nanoscale resolution.

Based on optical geometries, different variants of TERS systems have been reported. Usually, refractive objective lenses with large working distances are utilized in TERS systems due to their excellent optical imaging properties [34–36]. Alternatively, optical configurations based on an on-axis parabolic mirror were described which allow optimal focusing and minimal spot size due to the very large aperture [23, 37]. These systems suffer from two disadvantages: (i) part of the aperture is obscured by the mechanics for the tip and (ii) applying different light polarizations is difficult.

In our customized optical system, the off-axis parabolic mirror facilitates access to all polarization combinations of incoming and scattered photons to exploit the selection rules of the Raman process. The selection of different symmetries is possible by utilizing the orientation of the tip, thus enabling a finite projection of the polarization onto the sample surface. Obviously, a certain polarization leakage between the symmetries hinders the full separation of the symmetry components of the inelastically scattered light which is possible as in a conventional setup. Nevertheless, even with a single tip the symmetry projections can be accessed to some extent.

Despite of substantial progress in the experimental setup tip enhancement could not be demonstrated. Therefore, concerning TERS, the thesis is a progress report on the technical developments. Beyond that systematic studies of magnetic excitations in spin 1/2 systems have been carried out in insulating cuprates which are the parent compounds of the superconductors with the highest transition temperatures T_c at ambient conditions.

The cuprates are quasi two-dimensional materials characterized by the CuO_2 building units arranged in a layered pattern. Within these layers, copper atoms form a square lattice with oxygen atoms assembled at the bridging positions between neighboring copper atoms. The undoped parent compounds exhibit a Mott insulating phase with the Cu spins arranged antiferromagnetically. The spin dynamics of such systems are described in terms of a two-dimensional spin 1/2 Heisenberg model [11, 12, 38]. Superconductivity emerges by suppressing magnetism upon doping the parent compounds with either electrons or holes. The persistence of magnetism up

to the superconducting state indicates the interrelation between the two phenomena. This interrelation has a wide significance beyond the cuprates since essentially all unconventional superconductors are characterized by the proximity of competing phases with magnetism being the most prominent one.

Antiferromagnetic ordering in undoped cuprates has been widely studied by probing magnetic excitations. One of the frequently used techniques is inelastic neutron scattering which has unveiled the magnon dispersion in undoped cuprates [39–42]. Raman scattering has also played a pivotal role in accessing the magnetic excitations in undoped cuprates. Since the first experimental observation in La_2CuO_4 [1, 4, 11], much attention has been given to the magnetic scattering in B_{1g} symmetry. In all insulating cuprates, the B_{1g} symmetry is dominated by a broad peak originating from two-magnon scattering. A qualitative description of the two-magnon peak was obtained using the spin wave theory based on the two-dimensional $S = 1/2$ Heisenberg model including nearest-neighbor exchange interaction J [9, 14, 43]. However, the asymmetric line shape in the B_{1g} Raman response remains an open subject. Besides contributions from the multi-magnon and cyclic spin excitations or amplitude fluctuations has not been satisfactorily explored yet [13, 44–46].

Recently, the line shapes of the two-magnon B_{1g} Raman spectra in the Néel ordered state of undoped cuprates were explained using a field theoretical approach [47]. This approach is based on perturbation theory up to infinite order including the amplitude (Higgs) fluctuations of the order parameter. Analogous to the Higgs boson in particle physics [48], the Higgs modes appear as collective oscillations in a quantum many-body system as a consequence of spontaneous breaking of a continuous symmetry. Within the ordered state, the free-energy landscape has a Mexican hat structure, where the Higgs modes are decoupled from the Nambu-Goldstone modes associated with phase oscillations [49]. The theoretical fits were acquired using slightly different Higgs masses [47].

The recent theoretical results stimulate the quantitative study of the magnetic excitations and amplitude fluctuations. Since the theory predicts universal behavior it is of primary interest to compare the results from different families including La_2CuO_4 (LCO), $YBa_2Cu_3O_{6.05}$ (Y123), and $Bi_2Sr_2YCu_2O_{8+\delta}$ (Bi2212:Y). Furthermore, we compare the excitation energy dependent spectra to separate the intrinsic non-resonant line shape from a putative influence of resonant light scattering and extrinsic contributions such as luminescence. The magnetic excitations in the resonant regime have been theoretically addressed by several authors [44, 50–52]. In

addition to the usual resonance process, the triple resonance discussed by Morr and Chubukov [51] has also provided qualitative understanding of the experimental results on $YBa_2Cu_3O_{6.1}$ [53] and $PrBa_2Cu_3O_7$ [16]. Starting from the one-band Hubbard model, the triple resonance is expected when $\omega_{I,S} \sim U$ occurs simultaneously with $\omega_I - \Omega_q \sim U$ where $\omega_{I,S}$ is the energy of the incident or scattered photon, U is the Hubbard repulsion energy and Ω_q is the magnon dispersion. In the two-magnon Raman spectrum, the maximum appearing slightly below $3J$ has a resonance energy different from that of twice the maximum of the magnon dispersion $2\max(\Omega_q)$ at $4J$. It indicates that the line shape depends on the incident photon energy ω_I.

The thesis is organized as follows: Chapter 2 compiles a treatise of near-field theory. Chapter 3 summarizes the fundamental experimental and theoretical developments for TERS systems focusing on the enhancement factor. In addition, the key ingredients of the TERS setup including optical configurations, scanning probe microscopy, and tips designs are reviewed in general. Chapter 4 describes the conceptual realization of the customized TERS setup and summarizes test measurements. Chapter 5 comprises experimental results and discussions of the symmetry-resolved light scattering studies in the undoped cuprates with the focus placed on the magnetic excitation and amplitude fluctuations.

Chapter 2

Optical studies on the nanoscale

Continuous developments in the emergent fields of Nanoscience and Nanotechnology have always highlighted the requirement of new characterization tools which can perform on the true nanoscale. In the class of imaging tools, the traditional optical microscopy has played a vital role. However, the versatile use of optical microscopes in the sub-wavelength regime is restricted by the diffraction limit corresponding to approximately half of the wavelength of light [54, 55]. In order to obtain images with the sub-wavelength resolution, optical microscopy has to surpass the diffraction limit. The advancement of near-field optics has brought a variety of optical observations to a dimension below the diffraction limit.

This chapter will briefly summarize the diffraction limit of light, the fundamental properties of light propagation, and the near-field effects in the context of evanescent waves. Following this, surface plasmons and their role in enhancement mechanisms is discussed. A well-established near-field technique known as scanning near-field optical microscopy (SNOM) is described thereafter.

2.1 The diffraction limit of light

Diffraction is an optical effect where light begins to bend and disperse when passing near a barrier or through an aperture. The conceptual criterion of the diffraction limit for a microscope was first introduced by Ernst Abbé [54] which was further refined by Lord Rayleigh [55]. Rayleigh's criterion is based on a grating spectrometer and is often adopted in conjunction with optical microscopy. A detailed explanation of the diffraction theory can be found in Refs. [56–58]. In this section, an overview of the diffraction limit in the context of optical microscopy is presented.

A schematic of the diffraction-limited resolution in the case of optical microscopy

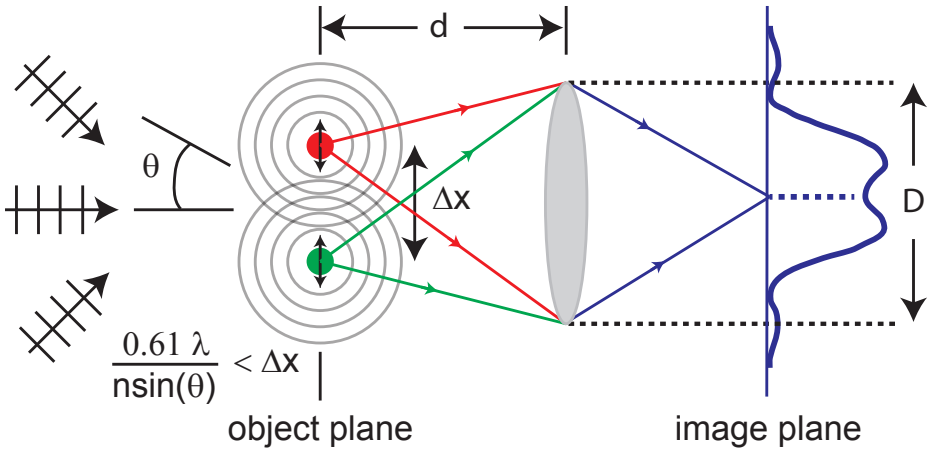

Figure 2.1: Principle of the diffraction-limited resolution in conventional optical microscopes. Two point-like objects (red and green circles) in the object plane separated by the distance Δx generate a conjugated spread function in the image plane using a glass objective located at the distance d from the point objects.

is presented in Fig. 2.1. Two point-like objects, separated by a distance Δx are exposed to the incident radiation of wavelength λ. The scattered light is collected by the glass objective ($\varnothing = \mathrm{D}$) placed at a distance d from the point objects and passed to a detector located in the far-field region. In the image plane, point objects appear as an Airy disk pattern. According to the Rayleigh criterion, two irradiated point objects can still be distinguished if the maximum of the Airy disk of one point object coincides with a minimum of the Airy pattern of the other point object. According to the Rayleigh criterion, the spatial resolution (Δx) reads

$$\Delta x_{\mathrm{min}} = 0.61 \frac{\lambda}{\mathrm{NA}}. \tag{2.1}$$

Here λ is the wavelength and $\mathrm{NA} = n \cdot \sin\theta$ is the numerical aperture of the objective lens where n represents the refractive index of the medium between the lens and the specimen (point objects) and θ is the one-half of the opening angle of the lens. Eq. 2.1 states that the two point objects separated by the distance Δx can only be resolved if they satisfy the condition of $\Delta x > 0.61 \frac{\lambda}{\mathrm{NA}}$. If two objects move closer to each other, their spread functions will start to overlap and reach to a point where they become identical and are no more resolvable. The rough estimation of the resolution criterion presented in Eq. 2.1 yields $\Delta x \approx \lambda/2$ which sets the diffraction limit for visible light to approximately 300 nm.

To understand the diffraction-limited resolution of any optical system, it is necessary to investigate how the electric field emanating from the scattering object

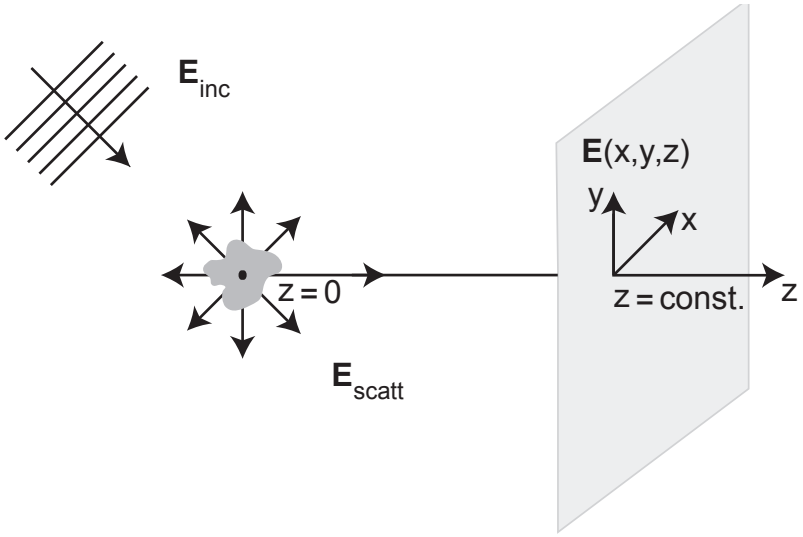

Figure 2.2: Schematic of an optical scattering configuration with arbitrarily chosen axis z. Here an object situated at $z = 0$ interacts with the incident fields ($\mathbf{E}_{\text{inc}}$). The scattered fields ($\mathbf{E}_{\text{scatt}}$) are evaluated in planes perpendicular to the z axis ($z = \text{const.}$).

spreads along a particular spatial direction. The angular spectrum representation [58] is one of the convenient mathematical techniques which allows one to study the light propagation in homogeneous media. In the following part, the behavior of electric fields emerging from any scattering object is scrutinized using the series expansion of an arbitrary field in the angular spectrum representation.

Let us consider an optical scattering environment as depicted in Fig. 2.2. When a scattering body located at $z = 0$ interacts with the incident fields, the scattering fields $\mathbf{E}(x, y, z)$ can be detected in the plane perpendicular to the arbitrary axis z. The total electric field is given by

$$\mathbf{E}(x, y, z) = \mathbf{E}_{\text{inc}} + \mathbf{E}_{\text{scatt}} \tag{2.2}$$

where $\mathbf{E}_{\text{inc}}$ and $\mathbf{E}_{\text{scatt}}$ are the incident and scattered electric fields, respectively. We assume that the electric field $\mathbf{E}$ at the scattering source $\mathbf{E}(x, y, z) = 0$ is known. In this case, the electric field at any position z can be calculated using the angular spectrum representation. In reciprocal space, the Fourier transformation of the field $\mathbf{E}$ at position z can be expressed as

$$\hat{\mathbf{E}}(k_x, k_y; z) = \frac{1}{4\pi^2} \iint_{-\infty}^{+\infty} \mathbf{E}(x, y, z) e^{-i[k_x x + k_y y]} dx dy. \tag{2.3}$$

Here x, y, and z are the Cartesian coordinates in real space and k_x, k_y, and k_z are their corresponding reciprocal coordinates. As the spatial spectrum $\hat{\mathbf{E}}$ at $z=0$ is known, we can obtain the spatial spectrum at any arbitrary point z in space by introducing a propagator. For free space, this propagator reads $e^{\pm ik_z z}$. In the case of a linear, isotropic, and homogeneous medium, the Fourier spectrum $\hat{\mathbf{E}}$ along the z direction can be written as

$$\hat{\mathbf{E}}(k_x, k_y; z) = \hat{\mathbf{E}}(k_x, k_y; 0) e^{\pm ik_z z}. \tag{2.4}$$

Eq. 2.4 includes a propagator factor $e^{\pm ik_z z}$ with $\pm$ sign indicating the direction of a wave propagation with two superimposed solutions. By combining Eq. 2.3 and Eq. 2.4, the resulting electric field $\mathbf{E}$ for arbitrary z can be obtained. This yields

$$\mathbf{E}(x, y, z) = \iint_{-\infty}^{+\infty} \hat{\mathbf{E}}(k_x, k_y, z=0) e^{i(k_x x + k_y y)} e^{\pm ik_z z} dk_x dk_y. \tag{2.5}$$

In Eq. 2.5, $\hat{\mathbf{E}}(k_x, k_y, z) = 0$ is the amplitude of the superposed harmonic waves. The wavevector $\mathbf{k}$ describes the propagation direction using wavevector components k_x, k_y, and k_z. In the case of a propagation along the z direction, the wavevector k_z can be denoted as

$$k_z = \sqrt{k^2 - k_x^2 - k_y^2}. \tag{2.6}$$

Here k is the magnitude of the wavevector which is defined as

$$k = \frac{2\pi n}{\lambda} \tag{2.7}$$

where λ is the wavelength of light and n is the refractive index of the medium. For a dielectric medium with no losses, the refractive index is a real and positive quantity. According to Eq. 2.6, we obtain two characteristic solutions of the wavevector k_z.

- If $k_x^2 + k_y^2 \leq k^2$, k_z is real with the propagator factor $e^{i|k_z|z}$. It represents an oscillatory function of the plane waves propagating along the z direction.
- If $k_x^2 + k_y^2 > k^2$, k_z is imaginary with an exponentially decaying function $\exp - |k_z|\, z$ associated with evanescent waves.

Considering the above solutions, we conclude that the spatial spectrum at any arbitrary position z is a superposition of plane and evanescent waves. The plane

waves (also known as far-field waves) are the propagating waves spreading out indefinitely in all directions. These waves are responsible for carrying the far-field information to the detector. In contrast, evanescent waves decay exponentially into a region of space forbidden for traveling waves. In the transverse (axial) plane, the larger angle between the **k**-vector and the z-axis leads to larger oscillations. For example, a plane wave propagating at 90° with respect to z provides the highest spatial oscillations in the transverse plane ($k_x^2 + k_y^2 = k^2$) covered by evanescent waves. In principle, the evanescent waves can cover an infinite spatial bandwidth, however, it is practically limited by the fact that the decay length of the evanescent field gets shorter for higher frequencies.

For any optical configuration, when the distance between an object and its image is larger than λ, the fields associated with the evanescent waves become negligible. The loss of evanescent waves leads to the diffraction-limited spatial resolution which is mainly attributed to the Fresnel diffraction (near-field diffraction). The Fresnel diffraction, in general, occurs when a wave passing through an aperture diffracts in the near field leading to the diffracted waves having short propagation length. It results in a Fresnel number F ($= d^2/l\lambda$) greater than 1 which depends on the diameter of the aperture (d), propagation length (l), and the incident wavelength (λ). In the case of increased propagation length, the diffracted waves tend to convert into planer waves.

In addition to the loss of evanescent fields, optical components of the corresponding system also limit the overall fields detected in the far-field. The limited collection efficiency of the optical elements does not allow all the plane waves to reach to the detector resulting in further loss of the fields at position z. This effect is known as Fraunhofer or far-field diffraction where diffraction patterns are observed in the image plane located at a distance larger than the size of the diffracting object. The collection efficiency of an optical component (e.g. lens) is determined by the numerical aperture (NA) as discussed in Eq. 2.1.

It is evident that the resolving power of the conventional optical system is diffraction limited and is not sufficient to characterize nano-scale objects. The resolution limit can slightly be increased by either decreasing the excitation wavelength or by filling the space between the object and the lens with a medium having a refractive index larger than 1 (Eq. 2.1) [59]. However, in order to gain a significant improvement, one must have access to the evanescent fields radiating from the sample. Without access to the evanescent fields, the diffraction limit is a hard boundary for the optical resolution.

2.2 Evanescent waves in the near-field

The main motivation behind near-field optics is to overcome the diffraction limit. Near-field optics utilizes the region in space where the evanescent waves exist. Evanescent waves occur when the light interacts with inhomogeneities (i.e. a plane interface of two materials with different refractive indices). In this section, we present an optical arrangement in order to understand how the near-field information can be retrieved in the far-field region.

The evanescent waves can be generated by total internal reflection occurring at the boundary of two dielectric media. When light propagates from an optically denser medium (refractive index n_1) into a lower density medium (refractive index n_2), the total internal reflection occurs only when $\theta_i > \theta_c$. Here $\theta_i = \arcsin(n_2/n_1)$ and θ_c are the incident and critical angles, respectively. In this case, evanescent waves are generated in the medium having lower refractive index. These waves always exist as coupled modes of the electromagnetic fields on a dielectric surface.

In order to access evanescent waves into the far-field region, we consider a simplified optical arrangement as depicted in Fig. 2.3 (a). Assume that an optical plane

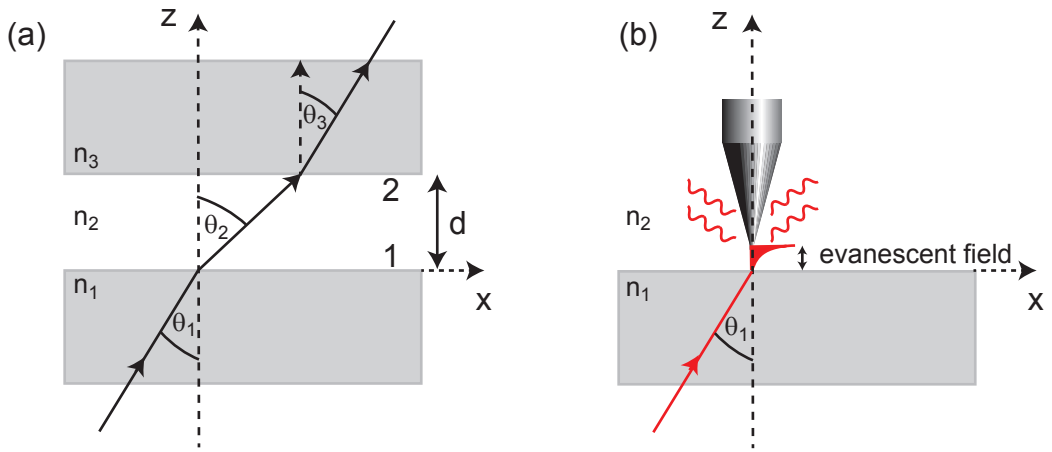

Figure 2.3: Propagation of the evanescent waves in different configurations. (a) Schematic of frustrated total internal reflection where the evanescent wave generated at interface 1 is converted into a propagating wave by the interface 2. (b) A simplified near-field optical arrangement. A tip is utilized to partly convert the evanescent waves into propagating waves. All the reflected parts are omitted for clarity.

wave is incident at the angle of total internal reflection (θ_1) on the surface of a rectangular optical element (n_1) and creates the evanescent waves at interface 1. When another optically dense medium (n_3) is brought at a distance on the order of a wavelength to the first medium, the evanescent waves couple to the interface 2 and

transmitted through the second optically dense medium. This process is referred to as the frustrated total internal reflection and can be obtained by satisfying the necessary condition of $\arcsin(n_2/n_1) < \theta_1 < \arcsin(n_3/n_1)$. The magnitude of the coupling efficiency depends on the gap d between the two dense media. The frustrated total internal reflection can be observed for any medium and do not necessarily require a planar dielectric surface.

Based on the idea of frustrated total internal reflection, the near-field optical effects can be explained. In Fig. 2.3 (b), a near-field optical setup is displayed where a tip is incorporated to scatter the evanescent fields into propagating waves detectable in the far-field. Apart from the above described phenomenon, evanescent waves can also be created and enhanced by surface plasmon polaritons at any metal-dielectric interface.

2.3 Surface plasmon polaritons

This section is dedicated to the general introduction of surface plasmons. It begins with the fundamental properties of light interactions in metals followed by the mechanisms responsible for launching surface plasmons at a planar interface.

Surface plasmons are surface-assisted waves occurring at a metal-dielectric interface. When a metal nanostructure interacts with light at optical frequencies, free electrons sustain the existence of surface and volume charge density oscillations [58]. These oscillations have distinct resonance frequencies. The properties of surface plasmons play an important role in a wide spectrum of technical applications such as biosensors, photonic devices, and near-field optics [60–63]. In the near-field optics, optical interactions are greatly influenced by the spatial extent of the surface plasmons. The surface charge oscillations coupled to electromagnetic fields are expressed in terms of surface plasmon polaritons (SPPs). SPPs are bound to the surface and do not radiate at planar interfaces. However, in the near-field regime the properties of SPPs can be altered with the geometrical modification, i.e. using a subwavelength structure. Such structures allow the SPPs to radiate locally. The SPPs exhibit a strong field confinement which together with the huge enhancement effects forms the basis of near-field techniques. These crucial effects of SPPs have been well exploited in the enhanced Raman techniques such as surface-enhanced Raman spectroscopy (SERS) [84, 102, 105] and tip-enhanced Raman spectroscopy (TERS) [22, 23, 31, 84, 175].

The phenomenon of light interaction with any metallic structure can be described

by a frequency-dependent complex dielectric function [64]. The dielectric function of a metal is given by the combined contributions from free electron $\varepsilon_{\text{Drude}}(\omega)$ and the interband transitions $\varepsilon_{\text{Interband}}(\omega)$ due to bound electrons.

The individual contributions are derived using the Drude-Sommerfeld model. The free-electrons contribution is given by the following expression:

$$\varepsilon_{\text{Drude}}(\omega) = 1 - \frac{\omega_p^2}{\omega^2 + \Gamma^2} + i\frac{\Gamma\omega_p^2}{\omega(\omega^2 + \Gamma^2)}, \tag{2.8}$$

where the plasma frequency is $\omega_p = \sqrt{\frac{ne^2}{m_e\varepsilon_0}}$. $\Gamma\,(= v_F/l)$ is the damping term which depends on the Fermi velocity (v_F) and the mean free path of the electrons (l). Eq. 2.8 is used to determine the optical properties of metals in the infrared regime. However, for the visible range, one has to also take into account the response of the bound electrons. For example, the interband transitions for gold take place from the $4d$ to the $5sp$ orbitals and the absorption edge falls in the visible range. The contribution of bound electrons to the dielectric function reads

$$\varepsilon_{\text{Interband}}(\omega) = 1 + \frac{\tilde{\omega}_p^2({\omega_0}^2 - \omega^2)}{({\omega_0}^2 - \omega^2)^2 + \gamma^2\omega^2} + i\frac{\gamma\tilde{\omega}_p^2\omega}{({\omega_0}^2 - \omega^2)^2 + \gamma^2\omega^2}. \tag{2.9}$$

It includes the plasma frequency as $\tilde{\omega}_p = \sqrt{\frac{\tilde{n}e^2}{m\varepsilon_0}}$. Typically, the plasma frequency of metals lies in the UV range. Noble metals such as gold and silver have lower plasma frequencies which make them suitable for optical applications in the visible regime [65].

Figure 2.4 shows the spectral dependence of real and imaginary parts of the dielectric function of gold (Au) as a function of wavelength over the extended visible range [58]. According to the free-electron model, we find that the real and imaginary parts of the dielectric function are negative and positive, respectively. This leads to a strong imaginary part of the refractive index $[\text{Im}(\text{n}) = \text{Im}(\sqrt{\varepsilon})]$ resulting in a low penetration depth in the metal. According to the interband contribution, a strong resonance behavior for the imaginary part is observed. On the other hand, the real part of the dielectric function shows the dispersion-like behavior.

In the following, we explore the properties of SPPs in a planar interface between two different media. Assuming that the first medium is characterized by a complex, frequency-dependent dielectric function $\varepsilon_1(\omega)$. The second medium has the real dielectric function $\varepsilon_2(\omega)$. The localization of SPPs at the interface is characterized by electromagnetic fields decaying exponentially with increasing distance from the interface. In the case of p-polarized waves (electric field vector parallel to the plane

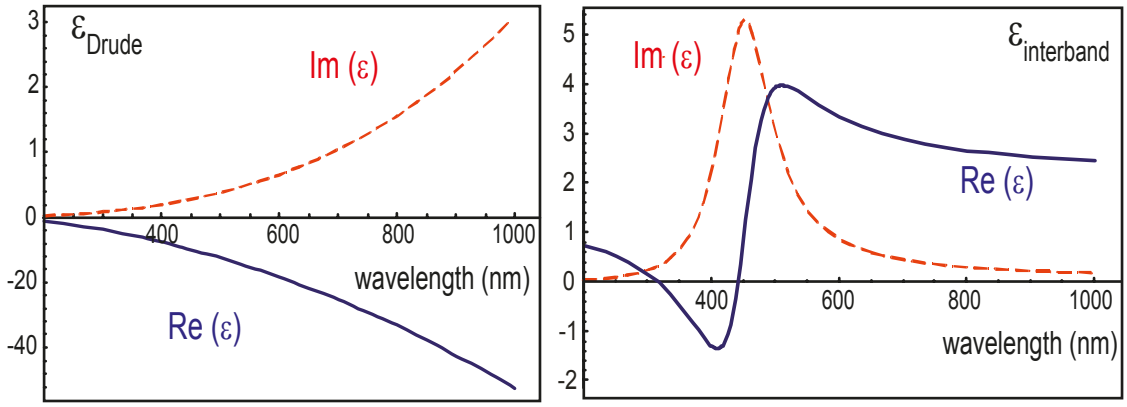

Figure 2.4: Real and imaginary parts of the dielectric function of gold. The spectral trends for the real [Re(ϵ)] and imaginary [Im(ϵ)] parts of the dielectric function are sketched for two different contributions. $\varepsilon_{\text{Drude}}$ presents the free-electron contribution with $\omega_p = 13.8\times10^{15}$ s^{-1} and $\Gamma = 1.075\times10^{14}$ s^{-1}. $\varepsilon_{\text{Interband}}$ represents the contribution from the interband transitions. The spectra are obtained using parameters $\tilde{\omega_p} = 45\times10^{14}$ s^{-1}, $\gamma = 9\times10^{14}$ s^{-1}, and $\omega_0 = 2\pi c/\lambda_0$ with $\lambda_0 = 450$ nm. Adopted from Ref. [58].

of incidence), the wavevector parallel to the interface will be conserved. The relation between wavevector components of the two media with half-spaces $j = 1$ and $j = 2$ reads as

$$k_x^2 + k_{j,z}^2 = \varepsilon_j k^2, j = 1, 2. \tag{2.10}$$

Here $k = \frac{2\pi}{\lambda}$ and λ is the wavelength. Using Eq. 2.10 dispersion relation between the wavevector and the angular frequency ω can be derived. Along the propagation direction, the dispersion relation is given by

$$k_x^2 = \frac{\varepsilon_1\varepsilon_2}{\varepsilon_1 + \varepsilon_2}k^2 = \frac{\varepsilon_1\varepsilon_2}{\varepsilon_1 + \varepsilon_2}\frac{\omega^2}{c^2}. \tag{2.11}$$

A similar solution for the normal component of the wavevector can be obtained

$$k_{j,z}^2 = \frac{\varepsilon_j^2}{\varepsilon_1 + \varepsilon_2}k^2, j = 1, 2. \tag{2.12}$$

Using Eq. 2.11 and Eq. 2.12, one can obtain the necessary conditions for the existence of an interface mode. For the propagating (plane) waves along the interface, k_x^2 should be real. According to Eq. 2.11, this condition can be fulfilled if the sum and the product of the dielectric functions are either positive or negative. To obtain a solution for the bound (evanescent) waves, the normal components of the wavevector have to be purely imaginary in both media. Thus, the overall conditions for the

existence of an interface mode are

$$\varepsilon_1(\omega) \cdot \varepsilon_2(\omega) < 0 \tag{2.13}$$

$$\varepsilon_1(\omega) + \varepsilon_2(\omega) < 0. \tag{2.14}$$

The above inequalities signify that one of the dielectric functions must be negative in order to launch the SPPs at the interface. For example, gold and silver have a large negative real part together with a small imaginary part of ε. Therefore, at the interface between any of these metals and a dielectric, localized SPP modes can exist. These modes play a vital role in the near-field effects.

In Eq. 2.11 and 2.12, $\varepsilon_1 = \varepsilon_1' + i\varepsilon_1''$ and $k_x = k_x' + ik_x''$ are complex while ε_2 is assumed to be real. The real (k_x') and imaginary (k_x'') parts of k_x can be determined using Eq. 2.11.

$$k_x' \approx \sqrt{\frac{\varepsilon_1'\varepsilon_2}{\varepsilon_1' + \varepsilon_2}}\frac{\omega}{c}, \tag{2.15}$$

$$k_x'' \approx \sqrt{\frac{\varepsilon_1'\varepsilon_2}{\varepsilon_1' + \varepsilon_2}}\frac{\varepsilon''_1\varepsilon_2}{2\varepsilon_1'(\varepsilon_1' + \varepsilon_2)}\frac{\omega}{c}. \tag{2.16}$$

Using Eq. 2.15, we obtain the wavelength of the SPP as

$$\lambda_{\mathrm{SPP}} = \frac{2\pi}{k_x'} \approx \sqrt{\frac{\varepsilon_1' + \varepsilon_2}{\varepsilon'_1\varepsilon_1}}\lambda. \tag{2.17}$$

The real part determines the wavelength of SPPs and the imaginary part gives the propagation length along the interface and is responsible for an exponential damping of the SPPs. The damping of the surface plasmon polaritons occurs due to the ohmic losses of electrons which results in the metal heating. For $\lambda = 633\,\mathrm{nm}$ and $\varepsilon_2 = 1$, the decay lengths in silver ($\varepsilon_1 = -18.2 + 0.5i$) and gold ($\varepsilon_1 = -11.6 + 1.21i$) are found to be approx. 60 and 10 µm, respectively.

Excitation of surface plasmon polaritons

The excitation of surface plasmon polaritons requires fulfilling the energy and momentum conservations. For surface plasmons, at given energy $\hbar\omega$, the wavevector k_x is larger than the wavevector of light in free space (Eq. 2.11). Due to strong coupling between the light and surface charges, the excitation of SPPs requires a wavevector component of the incident light which can be increased over its free-space. This can be achieved by the evanescent waves created at the interface between a medium

with refractive index larger than 1. There are various experimental arrangements which demonstrate the optical excitation of SPPs [66–68]. In these configurations, the SPPs are excited using the evanescent waves penetrating through the metal layers. In the near-field techniques, the evanescent fields are further enhanced using the sub-wavelength structures such as metal nanoparticles or metallic probes. In the close vicinity of the nanostructure, the excitation and propagation of SPPs lead to a locally enhanced field collected and simultaneously measured during the scanning over the sample.

2.4 Scanning near-field optical microscopy

The scanning near-field optical microscopy (SNOM) is considered as one of the valuable extensions of the classical optical microscopy. This technique is suitable for surface studies on the mesoscopic scale where confined interactions of the local probe (e.g. tip) with the specimen are employed. This section provides a brief overview of the SNOM technique including its principle and instrumentation.

The conceptual idea proposed by Edward Synge in 1928 [69] has allowed us to acquire nanoscale imaging by getting around the diffraction limit. His idea was to use an opaque metallic plate with an illuminated aperture smaller than the wavelength of the light for imaging sample surfaces with sub-wavelength resolution. If the metal plate is placed in the close vicinity of the sample (less than 100 nm), the spatial resolution will no longer be dependent on the wavelength of the light. The first experimental validation of Synge's idea was reported by Ash and Nicholls in 1972. In their experimental setup, microwave radiation with frequency of 10 GHz (~ 3 cm) was used to image an aluminum test pattern. With an aperture of 1.5 mm, a resolution of better than $\lambda/60$ was reported [70]. The realization of the near-field microscopy at optical frequencies was first demonstrated by Dieter W. Pohl [71]. The infrared scanning near-field optical microscopy (IR-SNOM) studies were also carried out by Knoll *et al.*[72]. Since then, numerous versions of the SNOM have been developed and used in a broad range of applications.

Based on the probe geometries, the SNOM is divided into two main configurations: aperture based SNOM (a-SNOM) and apertureless SNOM.

Aperture based scanning near-field optical microscopy (a-SNOM)

Figure 2.5 illustrates the working principle of aperture based SNOM. In a-SNOM configuration [73], the aperture probe with the diameter d ($d \ll \lambda$) is placed very

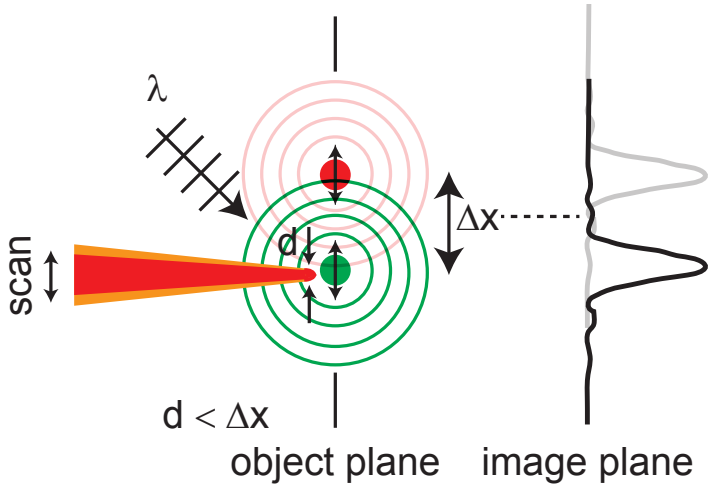

Figure 2.5: Principle of the scanning near-field optical microscope. A laser-irradiated aperture probe with diameter $d \ll \lambda$ acts as a near-field source for the point objects separated by the distance Δx. When the point object is at a distance within $\sim \lambda$, the confined source produces a propagating wave out of the evanescent field detectable in the far-field regime. The mapping of the point object is obtained in the image plane where spatial resolution is defined by the diameter of the tip (d).

close to the sample, i.e. two point objects placed at the distance Δx from each other. The incident light of wavelength λ is guided on the sample via an aperture probe producing a localized source with a confined field distribution. The probe is maintained in the near-field region of the sample by the local probing techniques (e.g. STM, AFM) and scanned over the sample. During the scan, a clearly resolved image in the form of distinguishable maxima is obtained in the image plane. In this setup, the resolution Δx is no longer restricted by the wavelength of light. Rather it is determined by the characteristic length d of the probe (in this case probe diameter d) and the probe-sample distance.

In a-SNOM setups, glass fiber based probe with a reflective coating material (e.g. aluminum) is typically used [73–76]. The key advantage of aperture based probes is to obtain the background-free imaging. However, these probes suffer from low optical throughput. When the incident light passes through the aperture probe, most of the propagating modes are cut off before reaching to the end of the aperture [77]. Therefore, only a fraction of the incident intensity leaks out as evanescent waves from the end of the aperture probe. Due to limited intensity interacting with the sample, excitation and collection through the same aperture are avoided. The near-field information is collected via conventional detectors placed in the far-field region. Apart from fiber based probes, several other variants of the aperture based probes have been developed. The geometry and fabrication process of such probes

are discussed in Refs. [78–83].

Apertureless scanning near-field optical microscopy

Apertureless SNOM has been employed for a wide range of near-field optical measurements [84, 85]. In this configuration, the aperture probe is replaced by a sharp metallic tip. The main objective of apertureless SNOM is to overcome the intensity limitations of the aperture probes.

In apertureless SNOM systems, a sharp metallic tip is irradiated with the excitation light. The incident radiation is converted into a confined field between the end of the tip and the sample in a spatial domain equivalent to the tip diameter. The maximum field confinement is accomplished by aligning the polarization parallel to the tip axis [111]. The tip is maintained in the near-field region and raster scanned over the area of the sample under investigation. The confined energy is then used to study the optical interactions in the near-field region. The localized interactions are observed at each scanned point and are guided to the far-field detector. This allows one to acquire the topography of the sample surface while recording the optical response simultaneously. Since metal tips are much sharper than the aperture based probes, one can achieve better spatial resolution. However, one encounters a few challenges. A metal tip generates a huge far-field background, thus a careful extraction of the near-field signals from the far-field background is necessary [84, 86]. Also, the tip induces topography-based artifacts which require more complex detection schemes [87].

The apertureless SNOM is categorized in two different operational modes. In the local-scattering approach, the metallic tip is used to locally perturb the fields of the laser-irradiated sample surface. The perturbation response is detected in the far-field region which comprises the waves that propagate away from the sample (propagating waves) and remain confined to the sample surface (evanescent waves). The scattering-type configurations typically have a high signal-to-noise ratio; however the scattering efficiency is very sensitive to the mechanical coupling of the tip and the sample which largely depends on the tip-sample separation. This sensitivity to the mechanical coupling complicates the data analysis and the derivation of the true optical contrast. Another mode is known as local-excitation mode where the excitation fields are confined at the tip apex locally. Using the appropriate excitation and polarization conditions, the fields near the tip apex can be strongly enhanced [88, 89]. In this approach, the measurements depend sensitively on the magnitude of the enhanced fields. This mode is commonly used in the tip-enhanced SNOM

applications.

A key component of the apertureless SNOM system is the metal tip. The tips are mostly crafted from solid wires using electrochemical etching method. This is one of the frequently used methods to fabricate the tips with high aspect ratio and better reproducibility. Electrochemically etched tips with diameters ranging between 10 and 50 nm have been reported in several publications [90–92]. There are numerous other tip designs which have been fabricated and used in different SNOM configurations. A few interesting apertureless tips are briefly discussed in subsection 3.3.3.

Chapter 3

TERS - principles and instrumentation

This chapter is aimed to summarize the essential elements of the TERS setup. Section 3.1 begins with an introduction to the conventional Raman spectroscopy. Section 3.2 discusses the working principles of TERS with the key focus on different enhancement mechanisms and their appropriate expressions. It is followed by an overview of various numerical methods that have been utilized to study the role of different parameters contributing to the overall enhancement factor. Section 3.3 succinctly describes crucial components of a TERS instrument.

3.1 Raman spectroscopy

The Raman effect, named after C. V. Raman, was co-discovered by Krishnan and Raman [93] and Landsberg and Mandelstam [94]. Raman spectroscopy is an instantaneous process in which an incident photon with the characteristic energy $\hbar\omega_{\mathrm{i}}$, momentum $\mathbf{k}_{\mathrm{i}}$, and polarization $\mathbf{e}_{\mathrm{i}}$ interacts with the target sample. Most of the photons are scattered elastically, the so-called Rayleigh scattering. Typically, a fraction of about 10^{-13} of the interacting photons is inelastically scattered from the sample. The energy $\hbar\omega_{\mathrm{s}}$ and momentum $\mathbf{k}_{\mathrm{s}}$ of inelastically scattered photons are finally analyzed. In this process, the energy Ω and momentum $\mathbf{q}$ remain in the system by satisfying the conservation laws of energy and momentum.

An inelastic scattering process from any sample is accompanied by a transition from an initial state $|I\rangle$ to a final state $|F\rangle$ via a virtual state $|\nu\rangle$. These transitions are categorized in two different processes as illustrated in Fig. 3.1. In the anti-Stokes process, the scattered photon is blue-shifted where the final state $|F\rangle$ has

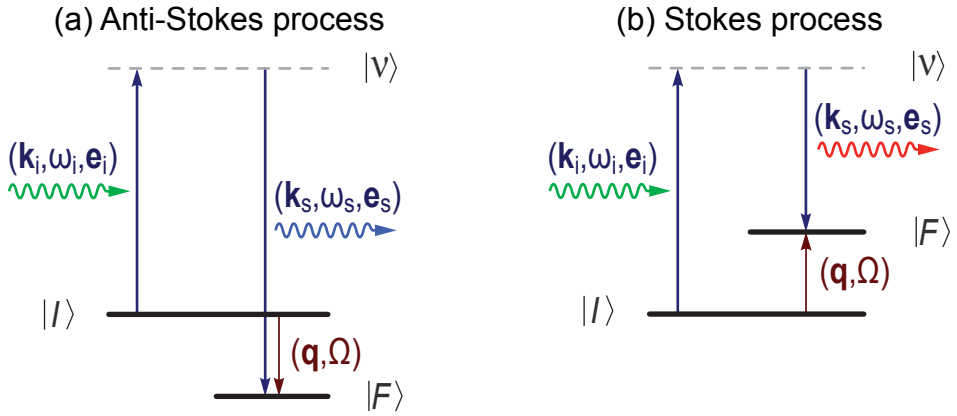

Figure 3.1: Raman scattering processes in the form of energy level diagrams: (a) Anti-Stokes process with an excitation annihilated in the sample resulting in the blue-shifted scattered photons. (b) Stokes process with an excitation created in the sample resulting in the red-shifted scattered photons. The incident and scattered photons are characterized by $(\mathbf{k}_\mathrm{i}, \omega_\mathrm{i}, \mathbf{e}_\mathrm{i})$ and $(\mathbf{k}_\mathrm{s}, \omega_\mathrm{s}, \mathbf{e}_\mathrm{s})$, respectively. Here $\mathbf{k}$, ω, and $\mathbf{e}$ define the momentum, energy, and the complex polarization vector, respectively.

lower energy than the initial state $|I\rangle$. On the other hand, when the scattered photon exhibits a red-shift, this process is termed as the Stokes process. In this process, the final state $|F\rangle$ is higher in energy than the initial state $|I\rangle$.

In the Raman process, high energies and small momenta are transferred to the system due to the dispersion nature of light, and the momentum of the probed excitation is close to zero (i.e. $\mathbf{q} \approx 0$). A sketch of a Raman spectrum is displayed in Fig. 3.2. In this spectrum, the number of scattered photons $I_\mathrm{s}(\Omega)$ is plotted as a function of the Raman shift Ω denoted in the units of wavenumber (cm^{-1}).

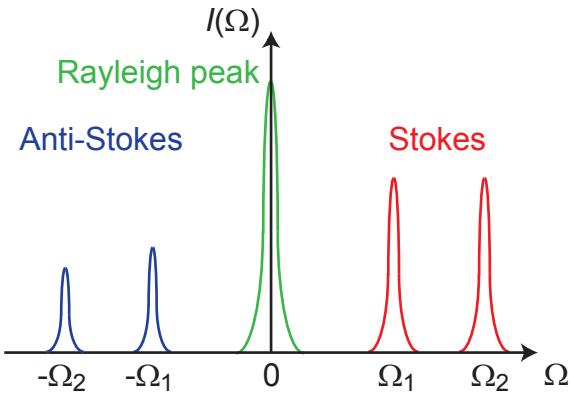

Figure 3.2: A Raman spectrum with different excitations. The Raman intensity $I(\Omega)$ is plotted as a function of the Raman shift (Ω). The peak at $\Omega = 0$ originates from elastically scattered light. The Stokes ($\Omega > 0$) lines have higher intensity in comparison to the anti-Stokes ($\Omega < 0$) lines.

The peak positioned at $\Omega = 0$ originates from the elastically scattered photons. The inelastic processes are shown on either side of the incident energy and labeled Ω_1 and Ω_2. The anti-Stokes peaks ($\Omega < 0$) have the same energy but are lower in intensity in comparison to the Stokes peaks ($\Omega > 0$). The relation between the Stokes and the anti-Stokes spectra is given by the principle of detailed balance which has the following form:

$$\frac{I_{\mathrm{AS}}}{I_{\mathrm{ST}}} = \left(\frac{\omega_i + \Omega}{\omega_i - \Omega}\right)^2 \exp\left(-\frac{\hbar\Omega}{k_B T}\right), \tag{3.1}$$

where I_{AS} and I_{ST} are the rates of photons in the anti-Stokes and the Stokes processes, respectively. k_{B} is the Boltzmann constant and T is the temperature.

In conventional Raman spectroscopy, the information averaged over the sampled volume depends on the penetration depth of light and the diffraction-limited illuminated area of the incident laser. Because of the diffraction limit, the lateral resolution cannot be better than about half a wavelength of the excitation laser. Moreover, the typically small cross sections make the observation of Raman signals very difficult in the nano-scale samples because of the reduced interactions. Tip-enhanced Raman spectroscopy (TERS) emerged as a novel spectroscopy method which provides access to the physical, chemical, and dynamical properties on a nanometer length scale. This technique exhibits a very high sensitivity with high spatial resolution down to the sub-nanometer range [32] which has led to its applications in a wide spectrum of fields such as chemistry [32, 95], material science [96, 97], surface science [98], and biology [99–101].

3.2 Working principles of TERS

TERS follows the same principles of operation as surface-enhanced Raman spectroscopy (SERS) [102–104]. The SERS system consists of assemblies of the molecules absorbed either on a roughened metal surface or a colloidal suspension of metal (e.g. gold, silver). The overall enhancement of SERS is estimated by averaging the enhancement obtained from the individual assemblies of the molecules. Despite the higher sensitivity, conventional SERS has certain limitations especially with regards to the substrates made of noble metals such as gold, silver, and copper [105] and the dependence of the total degree of surface enhancement on the interaction between absorbed molecules and substrate material [24]. TERS circumvents the above-mentioned restrictions of SERS by incorporating a metal tip, which is used to exploit the near-field effects by enhancing the electric field of the incoming laser.

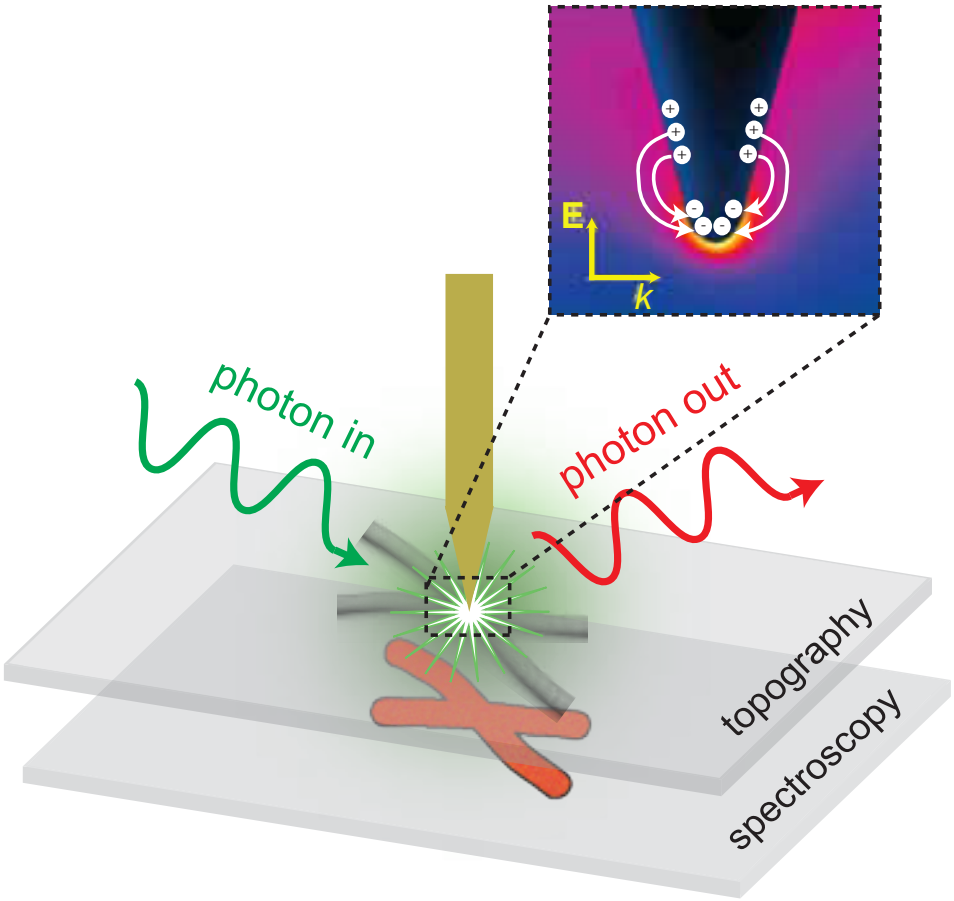

Figure 3.3: Working principle of TERS. When light (green) is focused on the tip apex, the excited surface plasmon and the antenna effect of the tip leads to an enhanced signal (red) which is collected by far-field detector. The sample and its topographic image are depicted in grey. The spectroscopic image is indicated in orange. In the inset, the electric field distribution around the metal tip apex is shown. Here, **E** and **k** represent the polarization and direction of the laser beam, respectively.

In contrast to SERS, TERS is capable to operate on any type of surface.

The working principle of a TERS system is depicted in Fig. 3.3. TERS is based on an apertureless SNOM configuration which integrates Raman spectroscopy and scanning probe microscopy (SPM). As discussed in the section 2.4, a metal tip is utilized to amplify the Raman signals from the confined area of the sample. Using the TERS configuration, spectroscopic and topographic information can be overlaid and interpreted simultaneously. Since TERS uses a tip as opposed to SERS for the enhancement, the enhanced signal can be attributed to the sub-wavelength areas of the sample under investigation.

3.2.1 Enhancement mechanisms

The enhancement mechanisms play a prominent role in any TERS system since the sensitivity and the resolution of the system are mainly interpreted in terms of measured enhancement [106]. The enhancement mechanisms for TERS are divided into two segments: the electromagnetic enhancement [107, 108] and the chemical enhancement [109, 110]. The most significant contribution to the overall TERS enhancement comes from the electromagnetic (EM) effects. These effects are usually categorized as (a) the lightning rod effect and (b) the surface plasmon effect.

The lightning rod effect

The lightning rod effect [111, 112] is a geometric phenomenon where electric charges are spatially confined at the surface of a conducting material. In TERS configurations, this effect takes place at the tip apex where the radius of curvature of the tip is much smaller than the wavelength of the excitation light. The lightning rod effect is a non-resonant effect which does not depend on the excitation wavelength. In TERS systems, the variation in the local fields (spatial confinement) due to the lighting rod effect has been studied mainly for two polarization states. The *p*-polarized state where the electric field vector of the light is parallel to the plane of incidence (along the tip axis) and the *s*-polarization state where the electric field vector is perpendicular to the tip axis.

When a sharp metallic tip is irradiated with the polarized light parallel to the tip axis, free electrons of the tip undergo induced surface charge oscillations [29]. Due to the geometrical singularity of the tip apex, the surface charge density is drastically increased underneath the tip. Thus, a strong and circumscribed electric field is generated at the end of the tip. The magnitude of the confined field is directly proportional to the tip radius. On the contrary, a tip apex illuminated with the *s*-polarized light remains uncharged due to non-localized field distributed around the edges of the tip shaft [58, 111].

Surface plasmon effect

As discussed in section 2.3, surface plasmons can be generated on the surface of the tip apex, when the wavelength of the incident light coincides with the plasma resonance of the tip material. The surface plasmons are wavelength-dependent oscillations which play a vital role in the enhancement of the TERS system. Although surface plasmon excitations have been observed for several metals, silver and gold

metals are usually preferred for TERS applications. Silver tips are better for the blue-green excitation sources whereas gold tips are mostly suited for the yellow-red laser sources [113]. Typically, the silver tips show higher field enhancement [114]. The dielectric function of silver has a smaller imaginary part which leads to decreased losses arising due to the optical absorption.

Chemical enhancement

The chemical enhancement described by Lombardi *et al.* [110] suggests that the resonance between the excitation light and the metal tip can induce a charge transfer between the molecular samples and the tip. In order to facilitate charge transfer, the tip has to be in direct contact with the sample. The chemical enhancement contributes on a smaller scale to the overall TERS enhancement with enhancement factors typically on the order of 10 - 100 [115]. This mechanism is mostly effective for molecular systems deposited on the metallic substrates.

3.2.2 Enhancement factor

The feasibility of TERS instruments largely depend on the extent of obtained enhancement which is expressed in terms of the enhancement factor. There are several ideas proposed in the literature [24, 116, 117] for a precise estimation of the enhancement factor. Here, we explore some of the important formalisms since these formalisms will be useful to interpret the performance of our system, especially while measuring thick samples such as silicon.

In TERS, the Raman enhancement factor scales with the fourth power of the field enhancement. This is due to the fact that the total enhancement is the result of the contributions from the enhanced excitation as well as the amplification of the scattered light [106, 118]. Experimentally, the TERS enhancement factor is estimated by deriving the contrast between the near- and far-field signals. The contrast (C) is defined as the ratio between the Raman intensities of near- and far-fields [25, 119].

$$C = \frac{I_{\mathrm{near-field}}}{I_{\mathrm{far-field}}}. \tag{3.2}$$

In TERS operation, the tip is placed in close proximity of the sample. Thus, the signals detected by the far-field detector not only contain the near-field information, but also consist of a far-field contribution in the form of background signals. Taking into account the far-field contributions, the near-field intensity can be defined as the

difference between the Raman intensities obtained with tip-in and tip-out modes [28, 36, 95]. This leads to a modified expression of the contrast as

$$C = \frac{I_{\mathrm{near-field}}}{I_{\mathrm{far-field}}} = \frac{I_{\mathrm{tip-in}} - I_{\mathrm{tip-out}}}{I_{\mathrm{tip-out}}} = \frac{I_{\mathrm{tip-in}}}{I_{\mathrm{tip-out}}} - 1. \tag{3.3}$$

Here $I_{\mathrm{tip-in}}$ and $I_{\mathrm{tip-out}}$ are the intensities during approach and retraction of the tip with respect to the sample surface, respectively. Now, one can derive the enhancement factor (EF) using the above definition of the contrast (Eq. 3.3). Since the interaction volumes in near- and far-field configurations are considerably different, the normalized signals have to be taken into account. An expression for the enhancement factor in the form of contrast is given by

$$EF = C \times \frac{V_{\mathrm{far-field}}}{V_{\mathrm{near-field}}} = \left(\frac{I_{\mathrm{tip-in}}}{I_{\mathrm{tip-out}}} - 1\right)\frac{V_{\mathrm{far-field}}}{V_{\mathrm{near-field}}}, \tag{3.4}$$

where the first term in the bracket is the direct measurable contrast, $V_{\mathrm{near-field}}$ and $V_{\mathrm{far-field}}$ are the volumes probed in near- and far-field configurations, respectively. Further expansion of Eq. 3.4 can be realized by defining the volumes probed by the near- and far-field sources. The focal volumes of the individual fields read

$$V_{\mathrm{near-field}} = R_{\mathrm{nf}}^2 \cdot \pi \cdot \delta_{\mathrm{nf}}, \tag{3.5}$$

$$V_{\mathrm{far-field}} = R_{\mathrm{ff}}^2 \cdot \pi \cdot \delta_{\mathrm{ff}}. \tag{3.6}$$

Here R_{nf}^2 and R_{ff}^2 are the radii of the illuminated areas, and δ_{nf} and δ_{ff} represent the penetration depths for the near- and far-field regions, respectively. Considering different volume contributions, we get another expression for the enhancement factor.

$$EF = \left(\frac{I_{\mathrm{tip-in}}}{I_{\mathrm{tip-out}}} - 1\right)\left(\frac{R_{\mathrm{ff}}^2}{R_{\mathrm{nf}}^2}\right)\left(\frac{\delta_{\mathrm{ff}}}{\delta_{\mathrm{nf}}}\right). \tag{3.7}$$

Eq. 3.7 is specifically valid for the estimation of the enhancement factor of thick samples such as silicon. For a sufficiently thin sample, one can assume approximately equal penetration depths ($\delta_{\mathrm{ff}} \sim \delta_{\mathrm{nf}}$). Using the above formula (Eq. 3.7), Steidtner and Pettinger estimated the enhancement factor for a monolayer of brilliant cresyl blue (BCB) molecules deposited on a single crystalline gold surface. The contrast and enhancement factor reported were 3900 and $\sim 1.6 \times 10^6$, respectively [23].

According to the generalized formulae discussed in this subsection, the overall enhancement depends on the parameters which are not precisely measurable, i.e.

tip radius, focal area of the incident laser, penetration depths of the near- and far-fields. This could result in substantial over- or underestimation of the TERS enhancement. Roy *et al.* [120] and Kumar *et al.* [121] have proposed different methodologies to precisely estimate the TERS enhancement factors. However, the use of specific samples (e.g. single-wall carbon nanotubes, bi-layer systems) restricts the general use of the proposed methods. In general, a good evaluation of the TERS enhancement can only be done by estimating the spectroscopic contrast and the field confinement (i.e. illuminated area, penetration depth). Hence, these quantities are of much practical relevance for the enhancement factor.

3.2.3 TERS enhancement - A theoretical consideration

To understand the underlying physical behavior of the TERS enhancement, a systematic study of different variables such as tip material, tip geometry, and tip-substrate configuration is instrumental. In this context, several numerical simulations studies have been performed in order to quantify the effects of various parameters on the enhancement. Moreover, these investigations can further be utilized as a reference for the design of a TERS system with high efficiency. Some of the frequently used simulation methods include finite difference time domain method (FDTD) [118, 122, 123], finite element method (FEM) [124, 125], and multiple multipole method (MMP) [111]. In this subsection, simulation studies of a few important parameters are presented.

Tip geometry

The optical response of a metal tip depends largely on its geometrical parameters such as tip length and shape. Figure 3.4 presents the finite element method (FEM) results of the dependence of the electric field enhancement on the curvature radius of a silver tip [125]. For all tip radii, resonance peaks close to 350 nm are observed, which essentially appear due to the plasmonic excitations. The spectra in the red and IR regimes are dominated by the lightning-rod effect. An increase of the surface charge density at the tip apex becomes prominent for sharper tips leading to a remarkable gain in the enhancement. The field enhancement is also found to be sharply increasing with the decrease of the tip radius. The effects of other parameters such as tip length and cone angle were also studied in the same report. The short truncated tips with length ranging between 200 and 500 nm are observed to produce better enhancement in comparison to longer tips (1000 - 3000 nm length) due to the

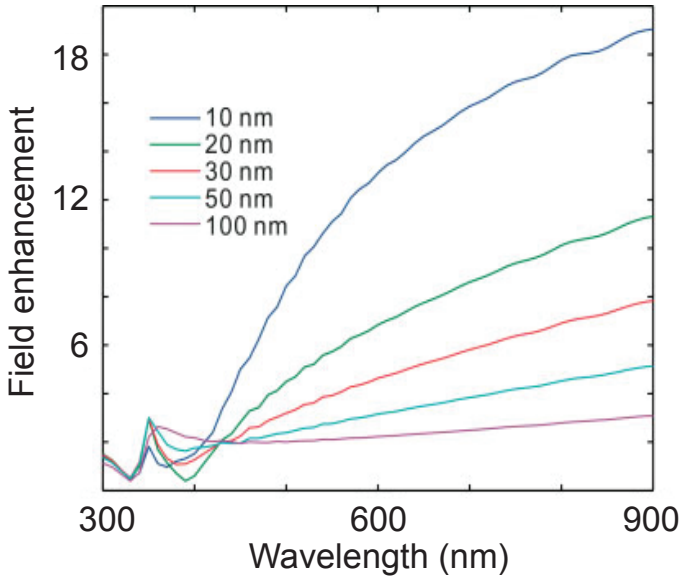

Figure 3.4: Simulations of silver tips using the finite element method (FEM). It shows the spectral variation of the localized electric field enhancement for different tip radii as indicated. For the simulations, the tip angles and tip lengths are kept constant. Adopted from Ref. [125].

excitation of the localized plasmon resonance. In the case of cone angle, the tip having a larger cone angle ($\approx 25°$) produces a slightly higher field enhancement in the IR regime.

Tip-substrate configuration

Figure 3.5 depicts the 3D-FDTD simulations of a canonical gold tip. First, we investigate the optical response of the gold tip when used with and without substrate. As illustrated in Fig. 3.5 (a) and (b), the monochromatic plane wave of $\lambda = 632.8\,\text{nm}$ is focused on a gold tip ($r = 25\,\text{nm}$) at an angle of incidence of 60°. Substrate-dependent studies show that the field enhancement can be greatly improved by introducing a plasmon-active substrate. The maximum field enhancement for the gold tip-gold substrate configuration is about 189, which is 9 times higher than the field enhancement obtained with a gold tip alone. Here, the maximum field enhancement is defined as the ratio of the local field (E_{loc}) and the incoming field (E_{in}). These results indicate that the coupling effect between the tip and the substrate plays a decisive role in the obtained enhancement.

In Fig. 3.5 (c), spectral characteristics of the dependence of the electric field enhancement on the tip-substrate separation are shown. The coupling between the tip and the substrate is found to be very sensitive to the tip-substrate separation.

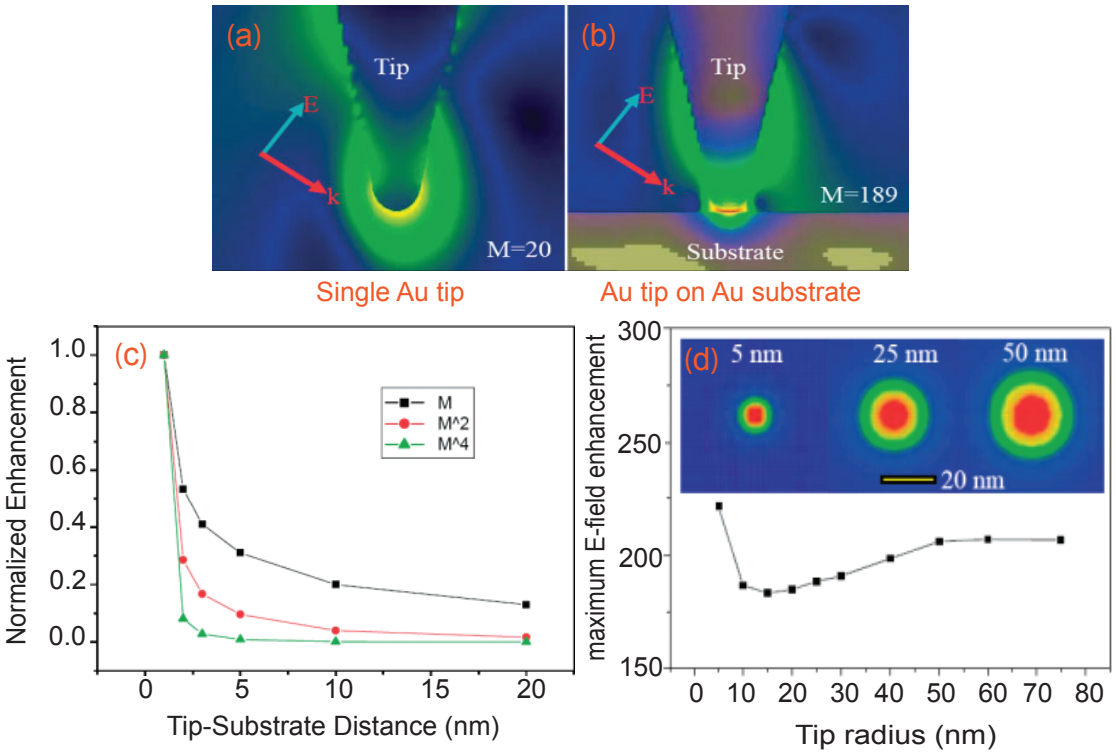

Figure 3.5: FDTD simulations of a gold tip in different configurations. The electric field distribution for a certain polarization state **E** and wave vector **k** for (a) a single gold tip (b) a gold tip and a gold substrate held at the distance of 2 nm is shown. (c) Dependence of the total field enhancement on the tip-sample distance. (d) Maximum field enhancement as a function of tip radius. Variation in the spatial resolution of TERS with respect to different tip radii is shown in the inset. Taken from Ref. [126].

When the tip-substrate distance is altered from 1 to 5 nm, the TERS enhancement decays by more than 90%. The maximum increase in the local field enhancement (M), enhancement intensity (M^2), and TERS enhancement (M^4) are observed when the tip-substrate distance was fixed to 2 nm.

In the following paragraph, we discuss the dependence of the enhancement factor and spatial resolution on the tip diameter. As illustrated in Fig. 3.5 (d), no significant variation in the field enhancement was observed for the tip radii ranging between 10 and 75 nm. However, for a smaller tip radius ($r = 5$ nm) the enhancement increases rapidly due to field line crowding (i.e. lightning rod effect) as discussed in subsection 3.2.1. Here the rapid increase in the enhancement originates from the strong confinement of the surface charge density which depends only on the radius of the tip. On the other hand, the spatial resolution is found to be strongly dependent on the tip diameter as shown in the inset of Fig. 3.5 (d). The field distribution corresponding to a tip radius of 5 nm shows the highest spatial resolution. The spatial

resolution can be estimated as directly proportional to the tip radius.

In summary, the theoretical calculations predict that the TERS enhancement is very sensitive to the geometrical parameters of the tip. Using various simulations one can effectively tune the parameters in order to achieve the maximum enhancement using any TERS system.

3.3 Key components of a TERS setup

In this section, we explore some important optical configurations, scanning probe techniques, and the probe designs which are essential for the development of our TERS setup.

3.3.1 Optical configurations

Depending on the opacity of the samples, several optical configurations have been used in various TERS systems. The main optical configurations include bottom illumination [25, 26, 28, 34, 127, 128], side illumination [27, 35, 95, 116, 129], and top illumination configurations [36, 130, 131]. Figure 3.6 represents the schematics of different optical configurations utilized in TERS systems so far. In all these optical arrangements, glass objectives are used. The glass objective based geometries are not appropriate for our customized setup, since these objectives cannot easily be used in ultra-high vacuum and low temperature applications. Our TERS setup uses a parabolic mirror as an objective. Therefore, in this subsection we focus on the TERS systems based on parabolic mirrors.

Parabolic mirror based setup

The imaging properties of a parabolic mirror having a high numerical aperture (NA) were first demonstrated for confocal microscopy [132]. Since then, parabolic mirrors have been used in numerous optical applications. In the context of TERS, the deployment of the parabolic mirror as a focusing element was recently described [23, 37, 133]. The parabolic mirror configuration, in general, has several advantages over the conventional refractive objectives. A high precision parabolic mirror can focus the incoming beams to one point without any aberration beyond diffraction. Due to the high NA of the parabolic mirror, the solid angle within which the scattered light is collected is significantly larger and reaches the theoretical limit of 2π in ideal configurations. This results in optimal focusing and minimal spot size. However,

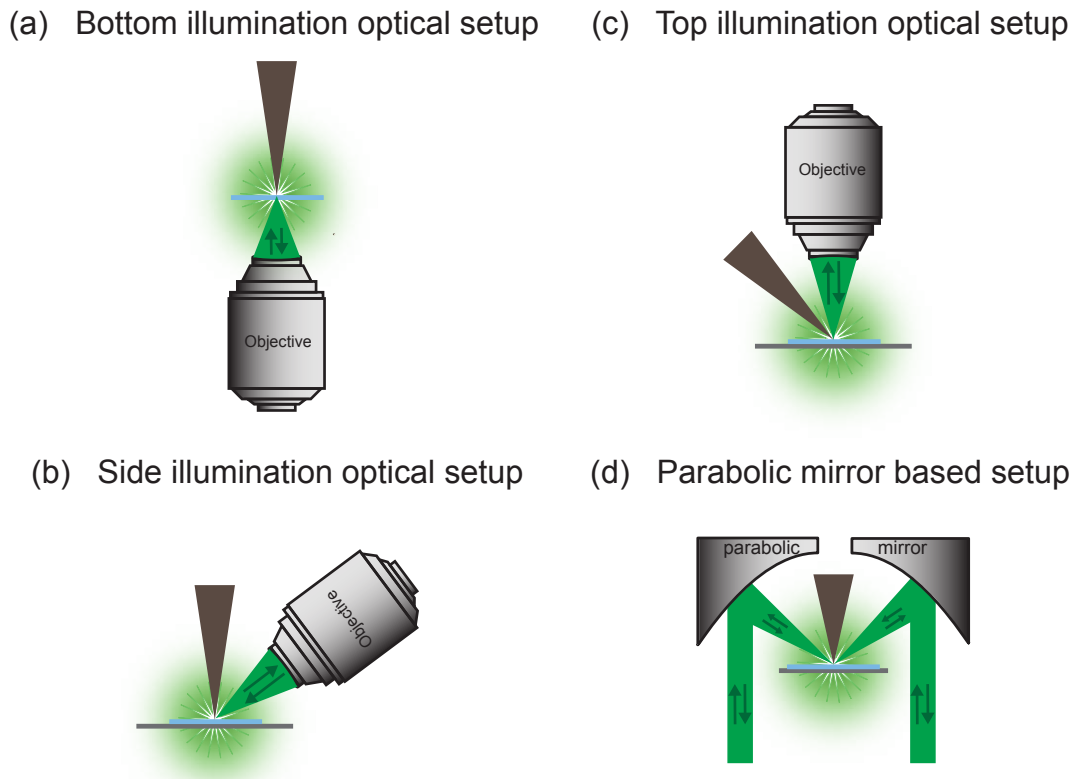

Figure 3.6: Different illumination and detection geometries for TERS systems. (a) A bottom illumination setup suitable for the transparent samples. (b) Side illumination and (c) Top illumination geometries which are appropriate for the opaque samples. (d) The parabolic mirror based geometry is a special configuration, which replaces the conventional glass objectives in the top illumination.

aberrations such as coma and astigmatism make the alignment procedure critical; the laser beam must be exactly parallel to the optical axis of the parabolic mirror [132].

The TERS configuration based on an on-axis parabolic mirror was first demonstrated by Steidtner and Pettinger [23]. In their setup, a high numerical aperture ($NA = 1$) parabolic mirror corresponding to a solid angle $\Omega = 2\pi$ was incorporated for TERS measurements in UHV conditions. The sample surface was oriented perpendicular to the optical axis of the parabolic mirror. With radially polarized light [132, 134, 135], a minimal focal spot with an exceptionally large longitudinal component of the electric field was produced. The tip was brought closer to the center of the focus through a hole in the parabolic mirror via a tuning fork based feedback system. Due to a small hole at the top of the parabolic mirror, a minor fraction of the signals was lost [see Fig. 3.6 (d)]. The successful implementation of TERS experiments in UHV conditions has further extended the applicability of TERS

instruments in extreme conditions (i.e. low temperature).

Our optical concept uses one half of a paraboloid and is intended to be used for low-temperature applications. The setup is described in section 4.3 in detail.

3.3.2 Scanning probe microscopy (SPM)

Scanning probe microscopy (SPM) is a generic term which includes a wide variety of techniques such as atomic force microscopy (AFM), scanning tunneling microscopy (STM), magnetic force microscopy (MFM), and friction force microscopy (FFM). Owing to the enhancement dependence on the tip-sample distance (subsection 3.2.3), a high accuracy distance control is necessary for TERS measurements. SPM feedback systems have accuracy required for distance control. In addition, SPM techniques could be used to independently locate the area of interest on the sample such as twin boundaries and defects. This subsection briefly recalls the fundamental operations of STM and AFM as both these techniques have been employed in our setup.

Scanning tunneling microscopy (STM)

The development of SPM started with the invention of scanning tunneling microscopy in 1982 by G. Binning and H. Röhrer at the IBM laboratories, Switzerland [136, 137]. Besides surface imaging with the spatial resolution down to atomic scale [138, 139], it has been used for various other applications such as study of superconductivity [140–144] and magnetic properties of new materials [145, 146]. Other applications of STM include molecular manipulation [147, 148], strength measurements of individual chemical bonds [149], chemical identification of atoms [150], and many other phenomena down to sub-nanometer scale.

The working principle of STM is depicted in Fig. 3.7 (a) where a metallic tip is utilized to obtain the topography of the sample surface. An atomically sharp tip is brought to within a few Å of the sample (conductor or semiconductor) using a three-dimensional piezoelectric positioner. A bias voltage is applied between the metallic tip and the conducting sample which leads to a tunneling current. The tunneling current depends exponentially on the tip-sample separation. The tip is scanned in the x-y plane above the sample. The distance between tip and sample is controlled by an actuator (Z). The scanning information is obtained by monitoring the current as a function of the position of the tip to construct a topographic image of the sample.

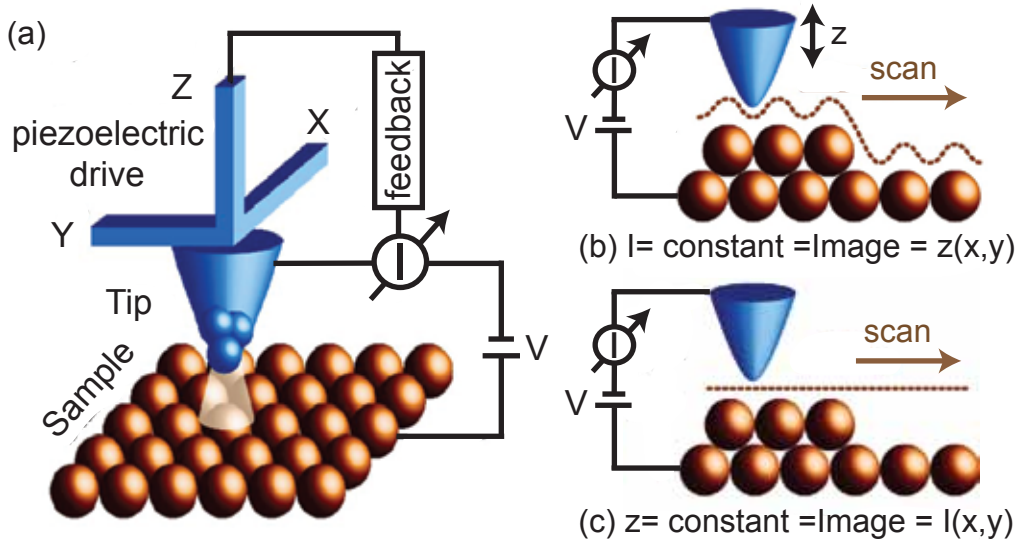

Figure 3.7: Schematic view of the working principle of an STM with the key operational modes. (a) A combination of the tip and the sample for the tunneling based imaging. (b) Constant-current STM mode. (c) Constant-height STM mode. Figures are acquired from Ref. [143]

The STM operates in two different modes: In constant-current mode [Fig. 3.7 (b)], a feedback loop is used to keep the tunneling current constant by adjusting the height of the scanner. Whenever the system detects a variation in the tunneling current, a feedback loop adjusts the piezo voltage to alter the distance between the tip and the sample. This mode is capable of measuring irregular surfaces with a very high precision. However, in this mode, scanning is slow and limited by the bandwidth of the feedback loop. In constant-height mode [Fig. 3.7 (c)], the vertical position of the tip is kept constant, equivalent to a slow or disabled feedback. The tip scans in a horizontal direction above the sample surface and the tunneling current varies depending on the local electronic properties of the sample. This mode is only appropriate for atomically flat surfaces as otherwise the tip may crash.

Atomic force microscopy (AFM)

The development of atomic force microscopy was triggered by the limitation of STM to conducting samples. The first idea of AFM was developed by G. Binnig, C. F. Quate, and C. Gerber in 1986 [151]. Since then, AFM is used as a routine imaging tool in many disciplines.

The working principle of AFM is schematically illustrated in Fig. 3.8. A cantilever, typically made of silicon (Si) or silicon nitride (Si_3N_4) with a tip radius of a

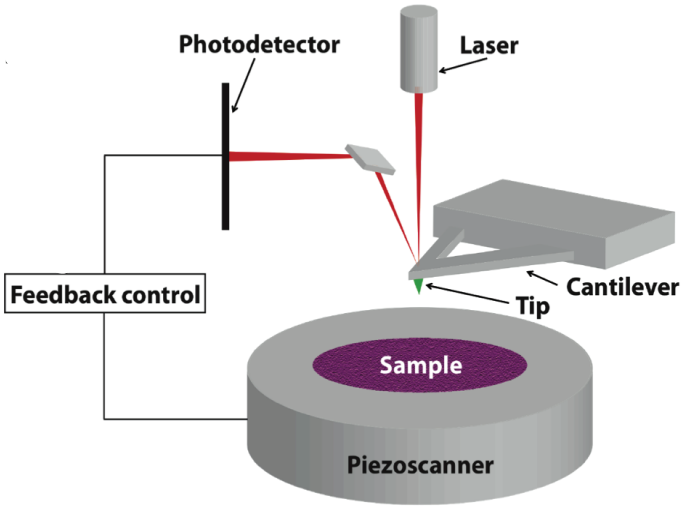

Figure 3.8: Working principle of conventional atomic force microscope (AFM) based on the laser detection scheme. Taken from Ref. [152]

few nanometers is brought sufficiently close to a surface to allow interatomic forces between tip and sample to be detected. The tip-sample interactions are studied in the form of attractive or repulsive forces. These forces are responsible for the displacement of the free-end of the cantilever. The cantilever reflects a laser beam onto a photo detector which traces the deflections of the cantilever during the scanning. These deflections are further used to map a topographic image of the sample.

AFM has three different modes of operation. In contact-mode AFM, the tip is brought in physical contact with the sample. Due to the overlap of electronic orbitals, exchange interactions between the tip and the sample give rise to predominant repulsive forces. In intermittent or tapping-mode AFM, a cantilever is driven at its fundamental resonance frequency. The variations of the oscillation amplitude are monitored to image the topography of the sample. In the non-contact mode, long range interactions (van der Waals and electrostatic forces) between the tip and the sample are responsible for acquiring the surface image. Since the tip-sample distance is larger for this mode, the area of interaction is minimized thus enabling atomic resolution.

Tuning fork based atomic force microscopy

Conventional AFM uses a cantilever-based optical detection where deflections of the laser are monitored using a location-sensitive photo detector. In the near-field optics, however, optical detection could obstruct with the observation of weaker near-field signals. Another version of AFM equipped with a tuning fork is often utilized in

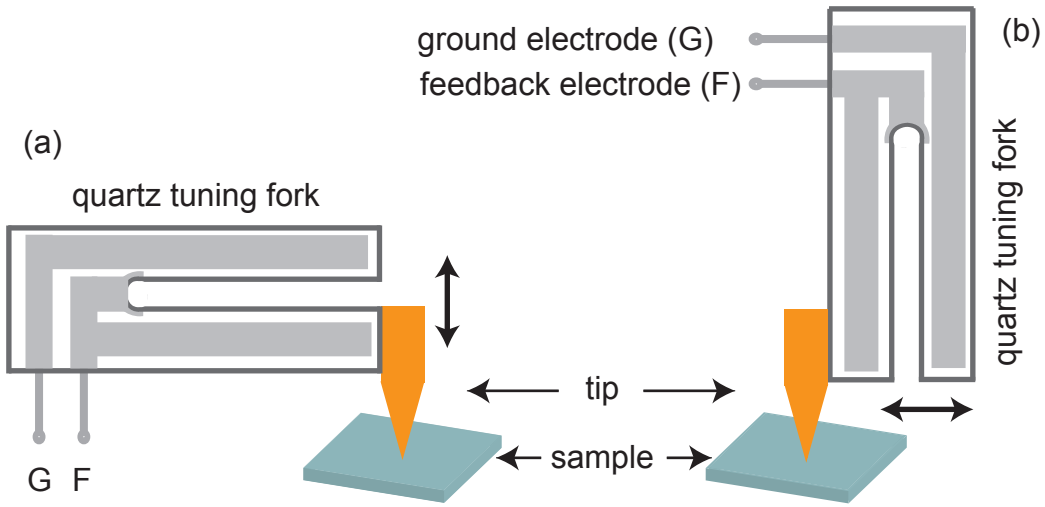

Figure 3.9: Tuning fork based feedback system in two different configurations. (a) Tapping (intermittent) mode. (b) Shear-force mode.

various near-field applications [153–155]. In this feedback system, a quartz tuning fork is used to regulate the sample-tip distance whose mechanical properties such as resonance frequency and Q-factor depend upon the interaction between the tip and sample [156]. In such systems, a tuning fork is mechanically excited at its resonance frequency and subsequently monitored for changes in frequency and oscillations amplitude. The oscillations of the tuning fork induce surface charges picked up by the electrodes and measured electronically. Typically, the resonance frequency of the quartz tuning fork is in the range of 30 - 100 kHz. A metal tip, commonly prepared using an electrochemical etching method is glued to one of the prongs of the tuning fork. As soon as the tip starts to approach the sample, the amplitude of the oscillations is reduced. While scanning, variation of the oscillating amplitude is measured at each mapped point to construct an image of the sample.

The tuning fork based AFM systems are categorized in two experimental configurations: tapping (intermittent) mode and shear-force mode. Figure 3.9 (a) shows a tuning fork based feedback system in tapping mode. It includes a tuning fork with a glued metal tip oscillating perpendicular to the sample surface. In TERS systems, the implementation of tapping mode configuration is very complex. In this mode, the tip repeatedly engages and disengages (on-off condition) with the sample surface leading to poor stability and accuracy of the tip position. Due to significant variations in the tip-sample distance, the near-field information is remarkably diminished. To overcome this issue, Ichimura *et al.* [157] proposed the idea to use

a time-gated illumination technique where the tip-sample arrangement is selectively illuminated only for a specific tip-sample distance. The tip oscillations and time gate are synchronized for a pre-selected tip-sample distance. Our custom-made TERS setup is also based on the tapping mode configuration. The detailed explanation can be found in section 4.6.

Another variant based on the principles of shear-force is depicted in Fig. 3.9 (b). In this configuration, a metal tip attached to one of the prongs of the tuning fork oscillates parallel to the sample surface. The feedback system maintains constant distance between the tip and the sample similar to the contact mode AFM. This system is advantageous for the TERS operation due to the constant distance between the tip and the sample which results in a consistent enhancement over the entire sample surface [23, 31, 37, 158].

3.3.3 TERS tips

This subsection briefly discusses various types of tips that have been used for TERS.

As a tip material, silver and gold are typically used. Regardless of dominant plasmonic response of the silver tips [113], gold tips are usually preferred. The gold tips are chemically inert and stable in ambient conditions. On the other hand, silver tips are very sensitive and can easily be oxidized in air. Thus, silver tips are required to be kept in the inert gas atmosphere and should be used immediately after preparation [159].

There are primarily two techniques for fabricating TERS tips. The fabrication technique depends largely on the feedback scheme incorporated in TERS system [160]. TERS assemblies with a cantilever-based AFM rely on metal coated tips [25, 35, 95, 123]. However, metal coating forms a granular surface resulting in inhomogeneous field enhancement. Also, it increases the diameter of the tip apex which affects the spatial resolution significantly. Prior to the deposition of the metal film, coating an AFM tip with materials of lower refractive indices such as SiO_2 and AlF_3 have shown promising improvements in the yield and the obtained enhancement [161, 162].

For TERS systems equipped with either STM or tuning fork based AFM metal tips are used. The tips are mostly fabricated by a simple, reliable, and cost-effective electrochemical etching method. The electrochemically etched silver [163–166] and gold tips [167–170] with a radius of curvature down to 5 nm have been fabricated and used in various TERS instruments. The electrochemical etching has proven advantageous for producing sufficient quality of the tips. However, fabrication of the

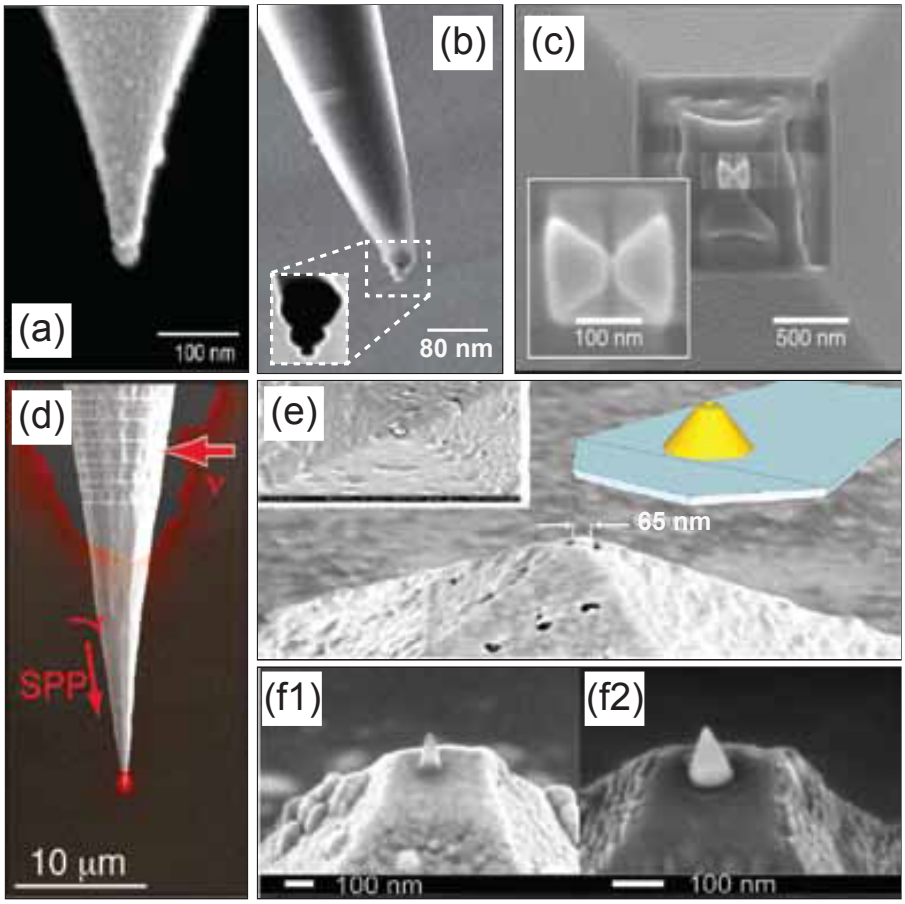

Figure 3.10: SEM micrographs of various tip geometries. (a) A tip with attached single metal nanoparticle. (b) A Gold trimer tip consists of three nanoparticles with different diameters. (c) A Bow-tie tip with a very small feed-through gap. (d) A sharp tip with the grating-like structures on the tip apex allowing a background-free illumination. (e) The coaxial tip, forming a metal-insulator-metal slit. (f1, f2) The gold nanocones.

uniform tips with a constant radius in a reproducible manner remains a challenge.

In the following, we explain some of the specialized tip designs which could be interesting for the future. Figure 3.10 (a) shows one of the non-standard tips where a single spherical nano particle is attached to the tip apex [171]. In this tip geometry, single gold or silver nanoparticle is attached using the particle picking method [171–173]. This design is capable of reproducing the enhancement, however the spatial resolution is limited which is governed by the size of the attached nanoparticle. In a similar context, Novotny *et al.* [174] demonstrated a trimer probe as shown in Fig. 3.10 (b). In this probe, three gold nanospheres with the diameters of 80, 40, and 20 nm are attached vertically. The field enhancement is confined to the smallest attached particle allowing one to achieve better resolution.

Schuck and co-workers [175] introduced a bow-tie probe having a two-particle

structure. This special antenna is made of two metallic nanotriangles facing tip to tip and separated by a small gap forming a shape of the miniature bowtie. A bowtie probe [Fig. 3.10 (c)] is fabricated either by e-beam lithography [175] or focused ion beam milling [176]. These tips are well known for their broadband performance. Another probe design based on the adiabatic plasmons was reported by Berweger *et al.* [177]. This probe was mainly designed for the complete elimination or maximal reduction of the far-field background. This is achieved by utilizing the propagation properties of the surface plasmons via nonlocal excitation. In the TERS experiments, a grating-coupler was used to launch the surface plasmons on the gold tip [Fig. 3.10 (d)].

Another probe variant known as coaxial antenna was demonstrated by Weber-Bargioni *et al.* for measuring carbon nanotubes grown on fused silica [178]. This specialized tip [Fig. 3.10 (e)] is composed of a metal-insulator-metal slit, which yields the low-loss propagation of the optical frequencies. The gold nanocones shown in Fig. 3.10 (f1 - f2)] are other promising candidate for near-field applications [179]. An individually engineered nanocone has a tip radius on the order of 10 nm. Using these probes, one can adjust the plasmon resonance frequency by varying the cone size in a controlled fashion.

All these specialized tips could play a promising role in achieving higher field enhancement with better spatial resolution. However, their sophisticated fabrication requires extraordinary special facilities for optimal results.

Chapter 4

Development of the customized TERS setup

This chapter describes details of the customized TERS setup part of which was developed during this PhD thesis. It comprises details of the instrumental layout including its unique optical geometry, the experimental setup, the fabrication of the tips, and a presentation of test measurements.

4.1 Instrument layout

A photograph of the experimental setup is shown in Fig. 4.1. The ^{4}He UHV cryostat and all novel optical elements are assembled and mounted on an optical breadboard on top of the optical table supported by vibration isolators. These isolators (Newport, S - 2000 stabilizer) have a hybrid chamber design to maximize the isolation bandwidth and the stability. This is one of the pre-requisites to perform high precision, vibration-sensitive measurements. The system is equipped with a cryogenically pumped UHV cryostat (Janis Research, CNDT series) for the low temperature measurements. The design of the cryostat is optimized for a short pumping time thus facilitating a fast sample exchange. At the bottom of the cryostat, three flanges with glass windows are available. The central flange provides optical access to the parabolic mirror and one of the side flanges is used for illuminating the sample.

The cryostat can reach a minimal pressure of 10^{-8} mbar and has an accessible temperature range of $10\,\mathrm{K} \leq \mathrm{T} \leq 300\,\mathrm{K}$. The vacuum chamber is evacuated by a turbo pumping station (Pfeiffer Vacuum, HiCube 80 Eco series). In order to accelerate the pumping speed, the chamber is flushed with dry nitrogen (N_2) gas. An appropriate nitrogen flushing setup combines a hydrosorb gas purifier cartridge

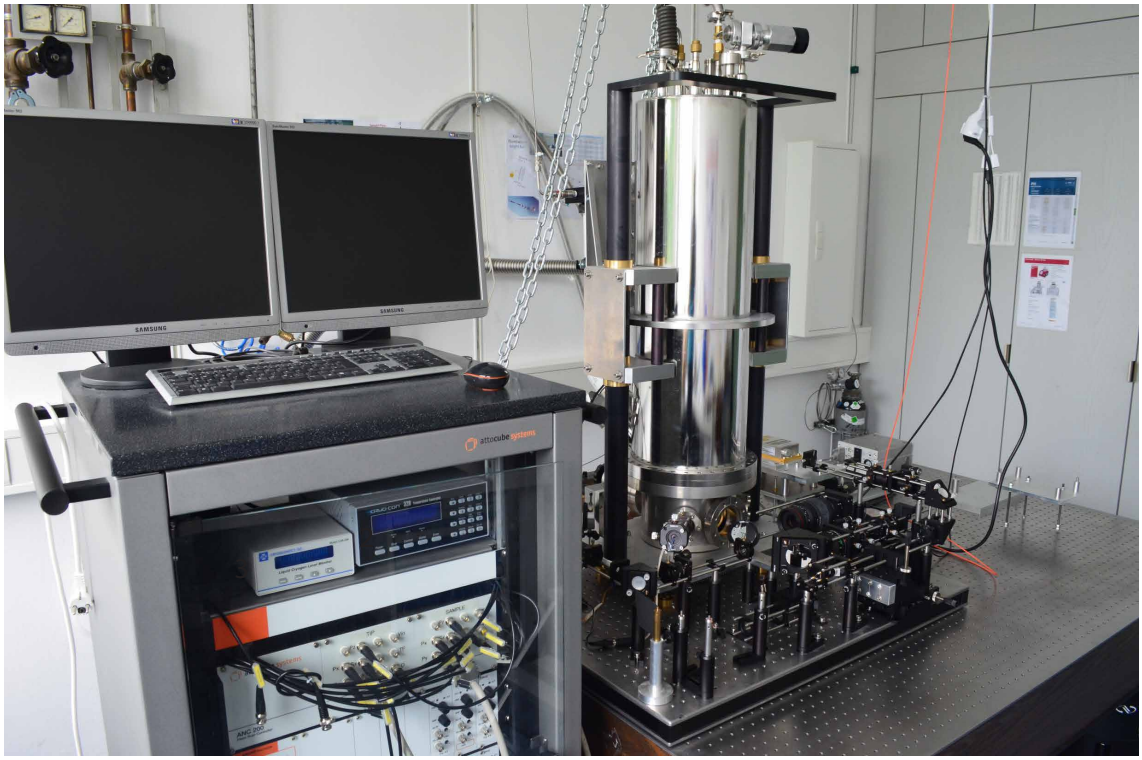

Figure 4.1: Photograph of the TERS laboratory in its current state. On the right hand side, the cryostat and the optics mounted on a breadboard are shown. On the left hand side, the electronic control unit is shown.

and a particle filter. This setup has been installed at the back of the cryostat and successfully tested. The base pressure was 10^{-5} mbar without filling in LHe. To achieve a better vacuum the cryostat may be baked prior to pumping.

A photo of the microscope unit along with the inner optical components in the open cryostat is presented in Fig. 4.2. The microscope unit is assembled on the base plate and is fixed to the cryostat in an upside down position. A side view picture of the microscopic head being located at the bottom of the cryostat is shown in Fig. 4.3. The microscope head accommodates a parabolic mirror and the scanning probe unit. The scanning probe unit consists of separate piezo stacks (positioners and scanners) for the sample and the tip, temperature sensors, sample plate, and tuning fork holder. The sample plate is attached to a slider which can easily be removed from the housing unit. The metallic contacts of the tuning fork are soldered on a printed circuit board (PCB). The tip is vertically glued to one of the prongs of the tuning fork and is perpendicular to the sample surface. All control units are assembled in the electronics rack (designed and assembled by attocube systems) next to the cryostat and can be accessed by the user-friendly computer program 'Daisy'.

The bottom part of the cryostat is attached to a base plate equipped with a

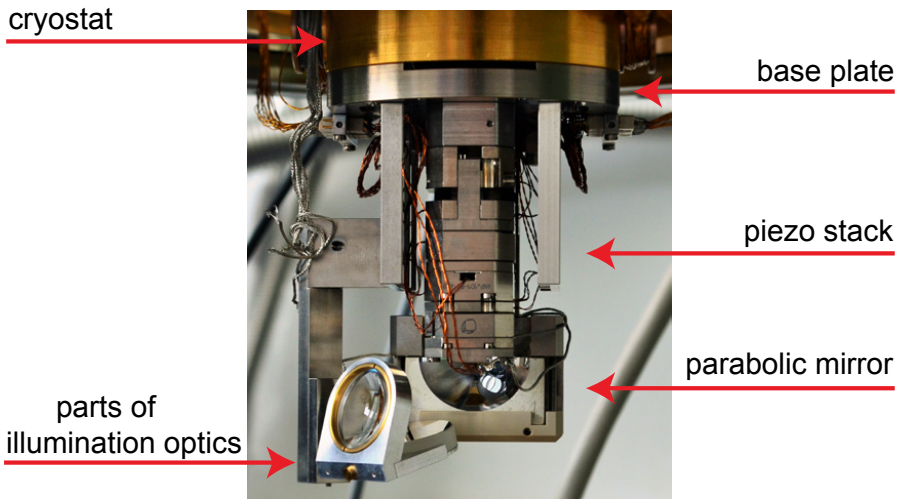

Figure 4.2: Microscope in the open cryostat. A base plate of the microscope is fixed to the cryostat. The parabolic mirror and the piezo stacks are located in the middle. Parts of the Köhler illumination setup (a plano-convex lens and a mirror) are shown on the left hand side.

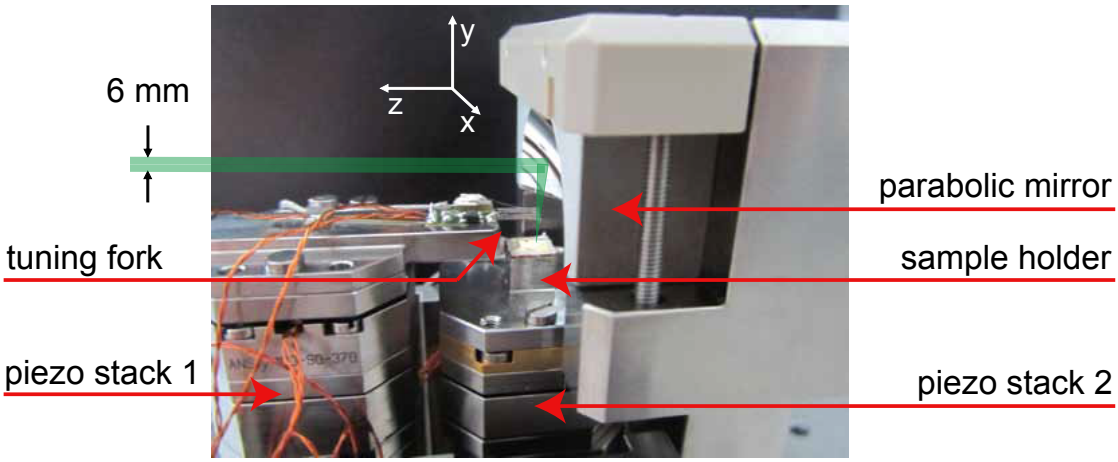

Figure 4.3: A side view picture of the microscope head (attocube systems) including the parabolic mirror and the SPM elements. Note that the picture is an upside down view of Fig. 4.2. The incident laser beam (green) is shown schematically. The tuning fork for scanning probe microscopy is mounted on stack 1 below the beam and the fork is parallel to the sample. With stack 2 the sample surface can be moved into the focus of the parabolic mirror. The coordinate system refers to laboratory system and is used to denote the polarizations of the laser beam outside the cryostat. The axis of the laser beam, the optical axis of the parabolic mirror, and the z-direction are parallel to each other.

height adjustment unit. This plate can be moved up and down in a controlled fashion with a precision of approximately 10 µm in order to compensate for the thermal contraction of the parts inside the cryostat upon cooling. Apart from the vertical adjustments, all the other adjustments need to be done via outer optics.

4.2 Experimental setup

A schematic drawing of the experimental setup is depicted in Fig. 4.4. We use two different diode-pumped solid state (DPSS) lasers emitting either at 532 nm (Coherent sapphire SF 523) or 660 nm (Laser Quantum, Ignis - FS 660). The laser heads are mounted on interchangeable base plates. The lasers emit vertically polarized light. Using a Glan-Thompson polarizer (P1) the laser power can be adjusted and the required polarization state of the incident photons can be preselected.

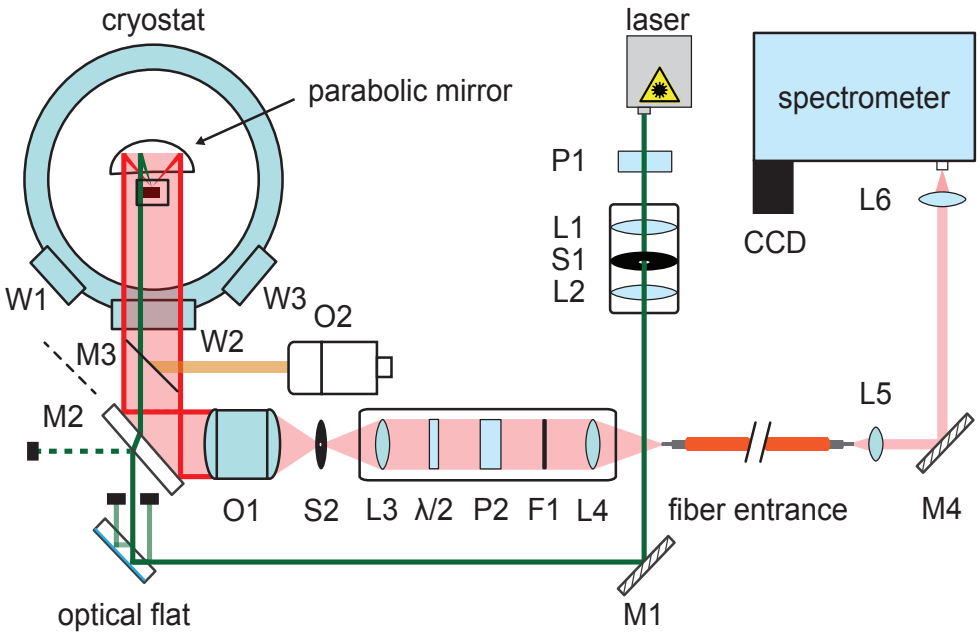

Figure 4.4: Ray diagram of our customized setup displaying the Raman light path and parts of Köhler illumination (M3, O2). Details are explained in the text.

After the polarizer P1 the beam is spatially filtered, and expanded to a diameter of approximately 6 mm resulting in a beam divergence of 2×10^{-4} mrad. The beam diameter is limited by the optical flat and the diameter of the parabolic mirror. According to Zemax simulations, the beam diameter can maximally be extended to 6.2 mm in order to avoid interference [180].

The spatial filter system consists of a set of achromatic lenses [L1, f1 = 10 mm and L2, f2 = 60 mm] and a circular aperture S1 (∅ = 30 µm). The laser beam is

directed to the optical flat via a dielectric mirror M1. The optical flat splits the laser beam into three strictly parallel beams. For aligning the laser beam parallel to the optical axis of the parabolic mirror, two side beams having approximately the same intensity are directed towards the parabolic mirror via a semitransparent mirror M2 [70:30 (R:T), plate beam splitter, transmission range 400 - 700 nm]. The most intense central beam is blocked for the initial alignment. The parabolic mirror alignment using an optical flat will be discussed in section 4.3.

For the Raman measurements, the two side beams are blocked and the central beam passes through mirror M2. The beam hits one of the quadrants of the parabolic mirror and is focused on the sample. The scattered light is collected by the parabolic mirror and reflected back in an ideally parallel fashion since it originates from a point-like spot in the focus of the parabolic mirror. The collection optics for the scattered light requires a special alignment procedure since the inelastically scattered light is too weak to be observed directly. Rather, a direct reflection of the incident beam is used for the primary alignment. The pictorial working principles of the alignment using tilted and flat silicon samples are presented in Fig. 4.5.

Firstly, the silicon sample tilted at 30° is brought into the focus of the parabolic mirror. In this case, the direct reflection hits the parabolic mirror and is reflected back parallel to the incident beam. A commercial objective lens O1 (Canon, $f = 85\,\text{mm}$, $f/D = 1.4$) collects the reflected beam via mirror M2. This reflection has enough intensity to be coupled into the multi-mode optical fiber. The optical fiber (NA = 0.22) has a core of pure silica ($\varnothing = 100\,\mu\text{m}$) with a transmission ranging from 180 to 1100 nm.

The coupling into the optical fiber is initially optimized by aligning the x-y-z translational fiber mounting unit. The transmitted light is recollected by the lens L5 and reflected into the spectrometer via mirror M4. A cylindrical lens (L6) reduces astigmatic aberrations due to the gratings inside the spectrometer. Finally, the scattered light is analyzed using a calibrated triple-stage spectrometer (Horiba Jobin-Yvon T64000) and recorded with a liquid-nitrogen cooled charge-coupled device (CCD).

Prior to measuring the Raman response from the tilted silicon, the direct reflection is blocked. The Raman intensity can be optimized by iteratively adjusting the sample and the optical fiber positions. Once the signal intensity is optimized, the flat sample placed next to the tilted silicon is brought in the focus of the parabolic mirror. One needs to follow the same procedure for the signal optimization on the flat sample before starting the tip approach.

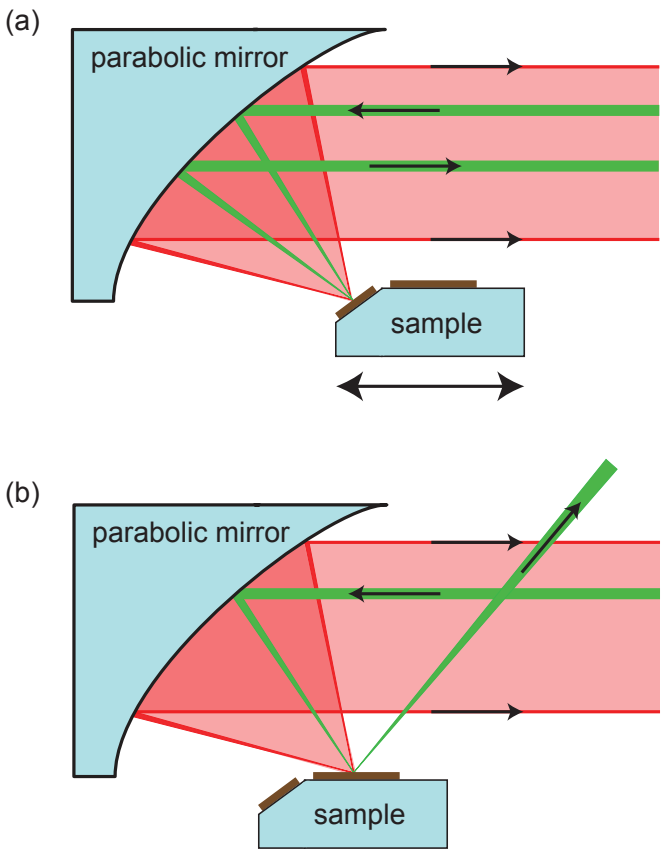

Figure 4.5: Schematics of the optical alignment using the tilted and flat samples. (a) For the tilted sample, the incident beam (green) hits the parabolic mirror and is focused on the sample. The direct reflection from the sample is reflected by the parabolic mirror. If the parabolic mirror's focus is on the sample, the directly reflected beam is parallel to the incident one and is coupled into the optical fiber. The shaded area (red) represents the inelastically scattered light. (b) For the horizontal sample, the direct reflection (green) from the sample does not hit the parabolic mirror. Instead, it hits the radiation shield. The inelastically scattered light (red shaded region) is collected by the parabolic mirror.

Between the camera objective lens O1 and the fiber, the light is filtered spatially (S2) and different polarization states can be selected. The desired linear polarizations are selected by setting the polarizer (P2) at a fixed position and rotating only the $\lambda/2$ plate. Since the waveplate has no wedge, the focus remains centered on the fiber core and the intensity is polarization independent. The elastic stray light is rejected by an edge filter F1 (Iridian Spectral Technologies, OD6) resulting in the reduced luminescence in the fiber. The optical fiber mixes all polarization states, thus unpolarized light reaches the spectrometer.

4.3 Off-axis parabolic mirror optics

The parabolic mirror (Fig. 4.3), in general, has several advantages over the conventional microscopic objective lens (see subsection 3.3.1). Hence, we implemented a new optical configuration using an off-axis parabolic mirror. Our optical configuration uses one half of a paraboloid. The parabolic mirror has a solid angle of $\Omega =$

π corresponding to a numerical aperture of ≈ 0.87. This mirror is used for several purposes. It improves the contrast between the near- and far-field signals, reduces the stray light, and is used for generating a magnified image of the sample. The surface quality of the mirror is equivalent to $\lambda/2$ at 632 nm. The diameter and focal length of the parabolic mirror are 30 mm and 8 mm, respectively. In this specific optical configuration, the sample surface is oriented parallel to the optical axis of the parabolic mirror. The choice of this specific orientation has several advantages. The direct reflection of the laser from the sample surface does not hit the parabolic mirror. Therefore, the elastic stray light is minimal as intended. This orientation also allows improved control over the polarization with little losses due to aperture reduction. Furthermore, it simplifies the application of the probe microscopic techniques enormously.

Parabolic mirror alignment using an optical flat

The introduction of a parabolic mirror in any optical configuration means a major challenge for alignment. In our case, the parabolic mirror is mounted on the base plate of the microscope. Whenever the tip and/or the sample is being changed, the parabolic mirror needs to be removed from the base plate. Thus, it becomes mandatory to align the outer optics with respect to the new position of the parabolic mirror. For the precise alignment of the excitation laser beam parallel to the optical axis of the parabolic mirror, we adopted a reference method proposed by Chen *et al.* [181] and Lee *et al.* [182]. In this method, one uses two exactly parallel laser beams which intersect in the focus of the parabolic mirror if and only if they are parallel to the optical axis of the parabolic mirror. For this purpose, we introduce a double-sided optical flat as schematically sketched in Fig. 4.6.

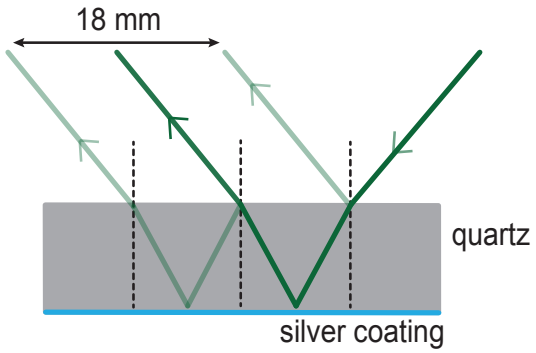

Figure 4.6: Sketch of an optical flat. The $10 \times 10 \times 40\,\mathrm{mm}^3$ block made of fused silica and coated with silver on one side. The incident laser beam is divided into three parallel beams. The central beam is the most intense beam and is used for the measurement. The two side beams are used for the alignment purpose.

A double-sided optical flat (B. Halle Nachfl., Berlin) is a rectangular cuboid made

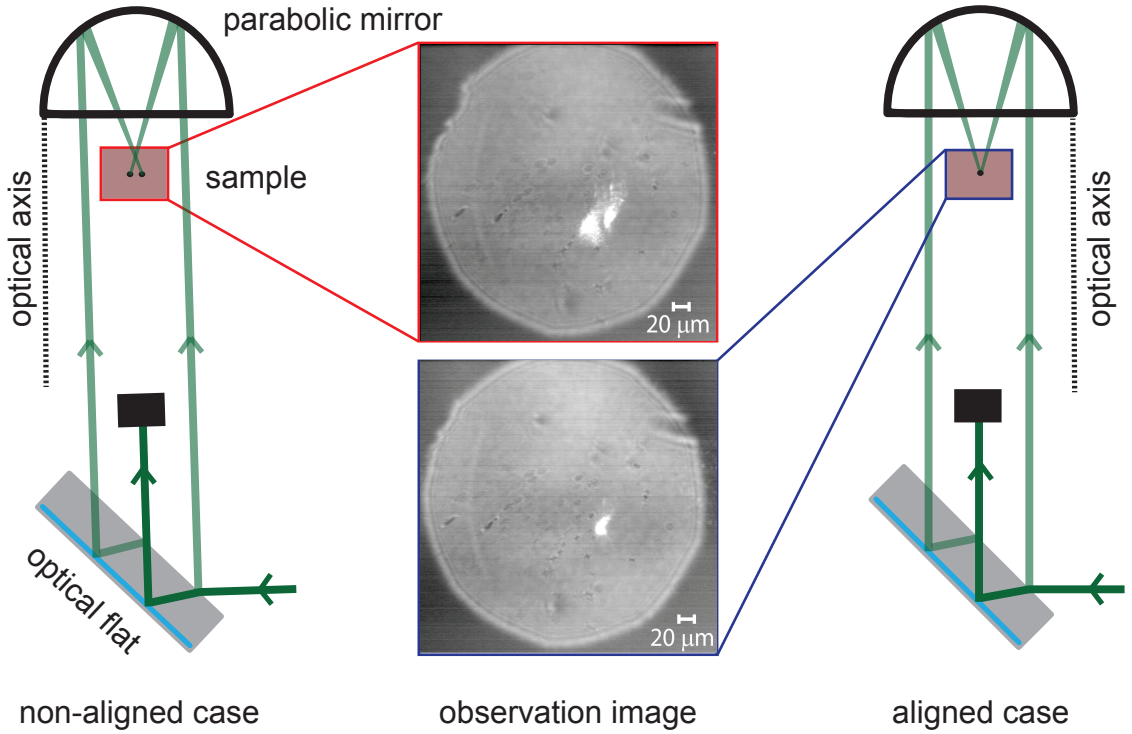

Figure 4.7: Ray diagrams of two different alignment cases. The alignment quality is determined by co-focusing of two laser beams using the optical flat. In the non-aligned case, two spots are visible in the reference image indicating that either the incident beams are not parallel to the optical axis of the parabolic mirror or the sample is not in the focus of the parabolic mirror. In the aligned case, the laser beams and the sample position are adjusted to make the two focal spots to coincide.

of fused quartz with a silver coating on the back surface. The front and back surfaces of the double-sided optical flat are parallel to within a precision of better than $\lambda/20$. The resulting error in parallelism is approximately 0.5 µrad. When an incident beam is directed towards the optical flat, it splits into three parallel beams. For $\lambda_0 > 500\,\text{nm}$, the resulting intensities of the three reflected beams are 0.040, 0.876, and 0.033, respectively. The higher order reflections are irrelevant due to very low intensities. The most intense, central beam is used for the Raman measurements. For alignment purposes, two of the side beams having similar intensities are used.

The ray diagrams of the aligned and non-aligned cases together with high-resolution reference images are depicted in Fig. 4.7. In this arrangement, the two side beams hit the parabolic mirror on two quadrants (left and right). Since it is not possible to change the position of the parabolic mirror inside the cryostat, the quality of the focusing alignment is iteratively improved by tilting and shifting the optical flat outside the cryostat. The optical flat is mounted on a mirror mount

which is equipped with fine threaded screws allowing a wobble-free movement with high accuracy and stability. A fine tuning of the screws allows one to adjust the incident beams in such a way that the two focal points coincide (image in the aligned case of Fig. 4.7). However, for a precise overlapping of the two spots, iterative tuning of the z position of the sample and screws of the optical flat mount is necessary.

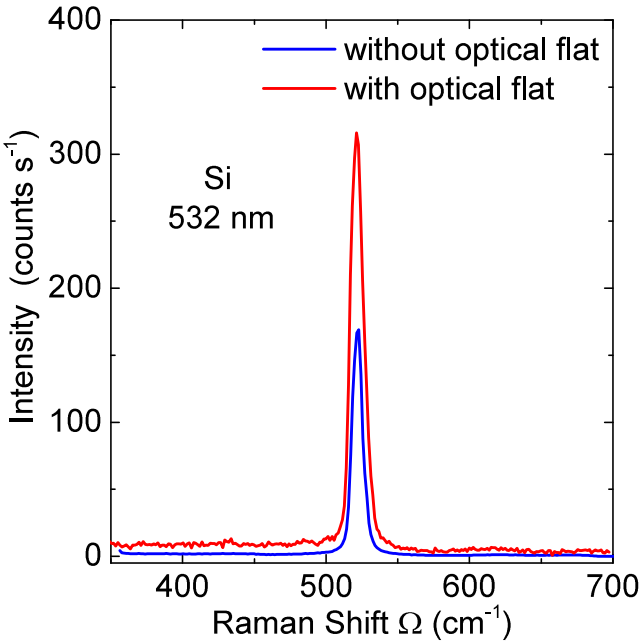

Figure 4.8: Far-field Raman spectra of silicon. When the optical flat was introduced for the alignment purpose, the intensity in the Raman spectrum of the silicon (red spectrum) could be enhanced by almost a factor of two with respect to that aligned without the optical flat (blue). The smoother background of the blue curve is due to longer acquisition time.

A measure of the alignment quality is primarily determined by the reference images. Besides the imaging, the alignment quality is characterized by the Raman measurements. Figure 4.8 presents the far-field Raman spectra of the silicon sample measured with the excitation wavelength of 532 nm. A noticeable improvement of a factor close to two in the Raman intensity was observed when the optical flat was introduced for the alignment of the laser beam.

4.4 Imaging optics

In our TERS configuration, the imaging optics provides high-resolution images (see Fig. 4.7) of the region around the focus of the parabolic mirror with a large field of view. The imaging system is also used for positioning the sample and the tip during the SPM measurements. Since the tip is first approached manually towards the sample, it is highly desirable to have visible access to the movement of the tip or the sample with reference to each other so that tip damage could be avoided.

Our customized system has an imaging setup based on the parabolic mirror as a microscope objective lens. The sample is illuminated using the principle of Köhler

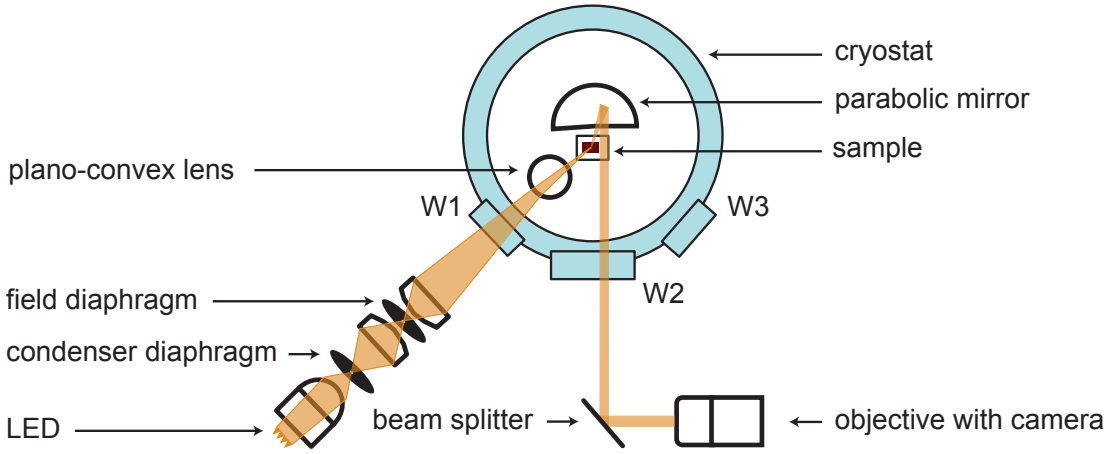

Figure 4.9: Layout of the imaging optics using bright-field Köhler illumination in combination with microscope observation optics.

illumination. It is designed by the optical ray tracing program 'Zemax'. The Köhler illumination is the best technique for isotropic sample illumination in a microscope. In the Köhler illumination, the image of the light source is defocused in the sample plane. For our TERS system, we have designed two different types of observation optics known as bright-field and dark-field illuminations. Both optical systems are intended to be used in the reflected light for opaque samples. Here, we discuss the bright-field illumination in brief as depicted in Fig. 4.9. The sample is illuminated through viewport W1. All the optical components of the illumination setup are mounted on the optical cage system inclined at 15°.

The Zemax simulation of the bright-field illumination is illustrated in Fig. 4.10. In this setup, a combination of achromatic lenses (A1 and A2) collects the light from the LED source and focuses it at the plane of the condenser aperture. The condenser aperture controls the intensity of light being transmitted to the sample. The position of the condenser aperture is adjusted in a way that the LED image fills the aperture completely. The light passing through the condenser aperture and the achromatic lens A3 produces parallel beams on the field aperture. The field aperture merely controls the illumination area on the sample surface. An achromatic lens A4 collects the light and directs it towards the plano-convex lens (L1) mounted inside the cryostat. The lens L1 recollects the light on a mirror fixed at 30° with respect to the lens. Finally, the light hits the sample. The reflected light from the sample surface is collected via the parabolic mirror.

The high-resolution observation system (O2) consists of a commercial zoom ob-

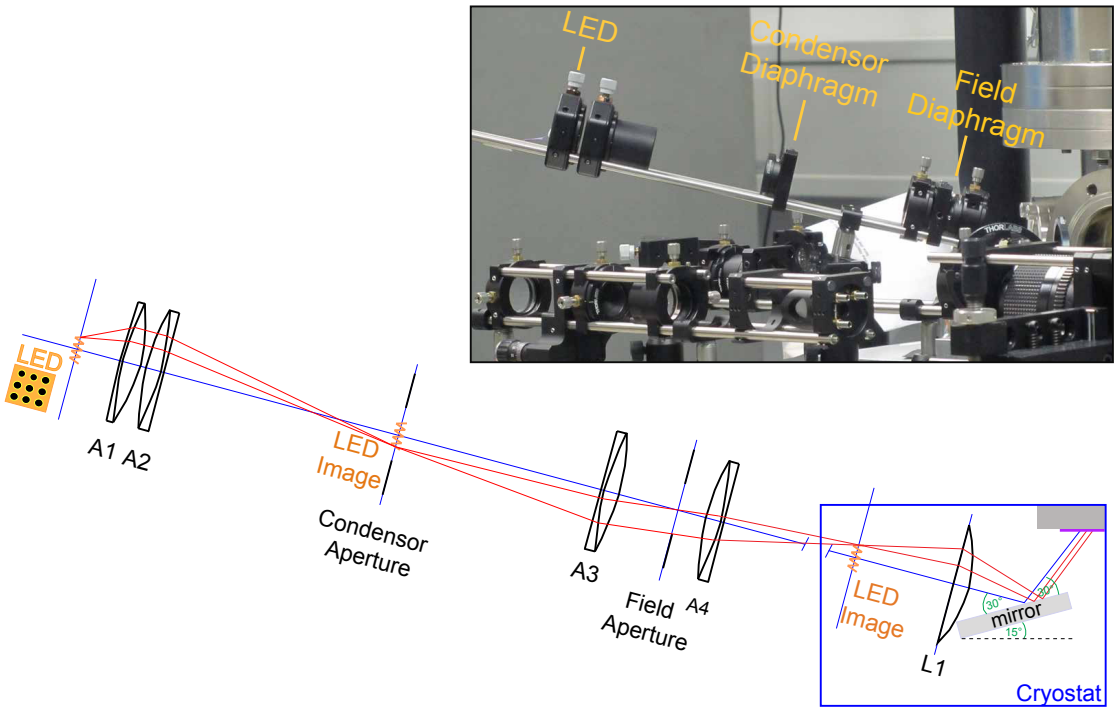

Figure 4.10: Ray diagram of the bright-field Köhler illumination with sequential arrangement of different optical elements. The top side picture portrays an assembly of the illumination system located outside the cryostat.

jective (Sigma Optics, f = 70....300 mm, f/D = 4.0....5.6) equipped with a video camera. The telephoto lens looks through an aperture of approximately 10 mm into the center of the parabolic mirror via the removable beam splitter M3. The final image is visualized on the computer screen.

To determine the optical resolution of the imaging system, several imaging tests using different resolution templates have been performed. Fig. 4.11 (a) shows a silicon sample with gold patterned pitches. The patterned sample consists of crosses (in the center) with the size of 10 µm and stripes (on the right side) with 20 µm periodicity. The maximum achievable optical resolution of the imaging system is estimated using the video images. The images of the crosses and strips are shown in Fig. 4.11 (b) and Fig. 4.11 (c), respectively. Presently, the estimated resolution of our imaging optics is approximately 2 µm. One can clearly distinguish that the resolution quality is strongly affected by the off-axis conditions of the parabolic mirror. The illuminated area associated with the exact focal region is better resolved in comparison to the remaining area. Since the curvature of the parabolic mirror across the aperture changes by almost 50%, a strong astigmatism is introduced which makes the images distorted. Although the achievable resolution is sufficient

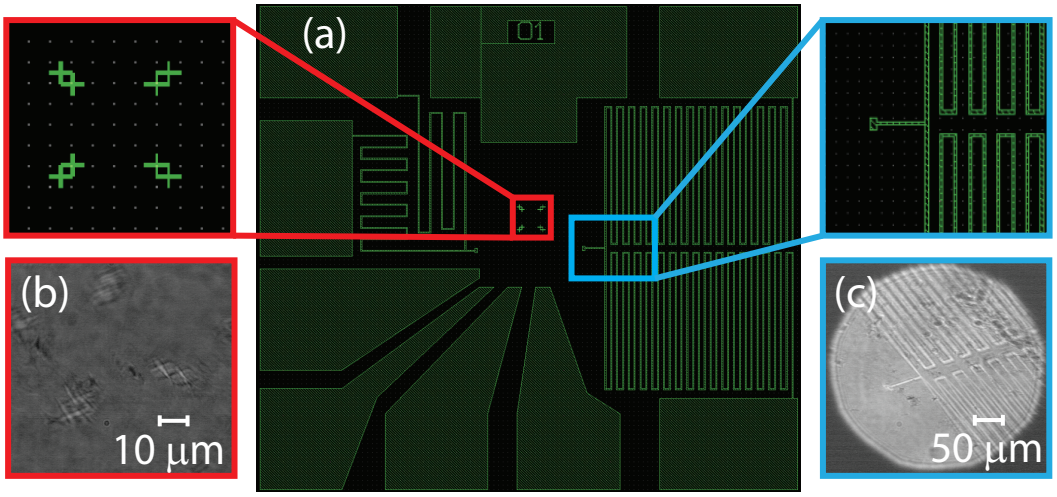

Figure 4.11: Optical resolution of our imaging optics. (a) A gold patterned silicon surface is used as a resolution test sample. On the left panel, the top zoom-in magnification of the crosses (red frame) together with the video image (b) in the bottom is displayed. On the right hand side, the zoom-in magnification of the stripe-lines (blue frame) together with the live image (c) in the bottom is shown.

for the intended purpose, a higher resolution would be beneficial for improving the alignment quality. For further improvement of the observation optics, we intend to introduce optical correction elements such as a cylindrical lens between the parabolic mirror and the objective camera.

4.5 Fabrication of tips

In this section, the fabrication of the gold tips using an electrochemical etching method is described. The etching procedure was adopted from Ref. [91] and various parameters were adjusted as per our requirements.

Gold (Au) wires of diameter 100 µm (ChemPur Germany, purity: 99.999%) are first cleaned by rinsing with acetone. After cleaning, the gold wires are annealed in air for 6 hours at 800 °C. The advantages of wire annealing prior to the etching were demonstrated by Roy *et al.* [183]. The annealing of the wire produces a single crystalline tip apex which improves the field enhancement. The tips without heat treatment contain multiple grains and grain boundaries in the tip shafts resulting in polycrystalline tip apices.

A sketch of our etching setup is shown in Fig. 4.12. A circular ring (approx. $\varnothing = 8$ mm), made of a platinum (Pt) wire of diameter 250 µm (ChemPur Germany, purity: 99.99%) is submerged about 5 mm in hydrochloric acid (HCl, 37% fuming)

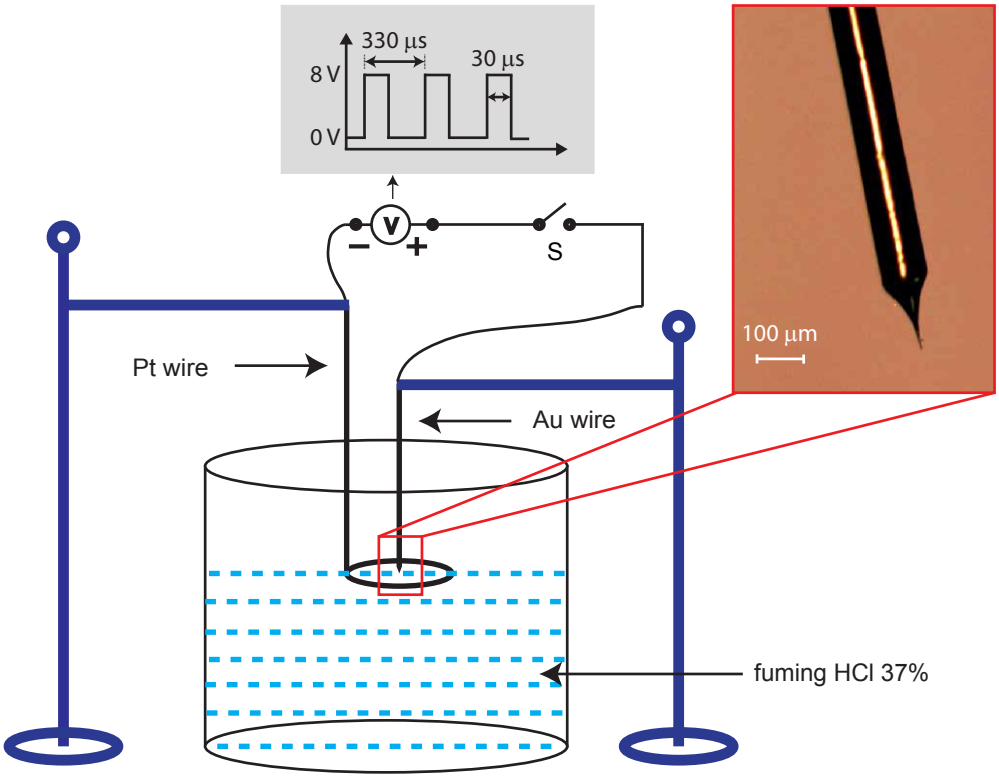

Figure 4.12: Sketch of the electrochemical tip-etching setup. The applied voltage profile is shown in the grey shaded area. In the inset, an optical image of the etched gold tip is shown.

solution. The gold wire used as an anode is fixed in the center of the platinum ring which works as a cathode. The gold wire is lowered until it touches the surface of the solution, forming a meniscus at the end. Square pulses for the duration of 30 µs at the repetition frequency rate of 3 kHz with a 10% duty cycle are applied (30 µs on, 300 µs off). The square pulses are generated by a combination of two function generators (Philips PM1538 and Voltcraft FG1617). The 8 V pulses together with the DC offset voltage of 0.4 V are applied to the system. The DC offset is determined by the diameter of the Pt wire. The optimal DC offset voltage for the Pt wires having diameters of 250 µm and 500 µm were found to be 0.4 V and 0.5 V, respectively.

Once the etching reaction is initiated via a manual switch (S), the platinum ring directs the current flux around the gold wire. This leads to a reaction indicated by the formation of bubbles on the Pt ring which determines the etching speed and hence the roughness of the tip surface. In order to reduce the bubbling effect, ethanol can be added to the etchant solution [167]. After a few seconds, the etching stops automatically indicating that the wire has been etched completely. The com-

plete process of etching takes about 20 seconds if the proper configuration of the parameters is used. At the end of the process, the etched tip is rinsed with distilled water to eradicate impurities formed during the etching reactions.

The electrochemical etching of the gold wires in hydrochloric acid solution involves several side reactions such as chloride formation, gold oxidation, and hydrogen gas evolution [91, 168]. As the etching reaction commences, a large amount of chloride ions are consumed to etch the gold wire. This leads to the depletion of chloride ions and formation of gold oxide. The oxide ions decrease the etching current dramatically because the reaction products take a longer time to diffuse. Since the etchant solution is not stirred during the etching, the etching current is further reduced. In order to increase the required current and to dissolve gold oxide, hydrochloric acid solution diffuses to the tip volume and again supplies the chloride ions. This process occurs repeatedly until the termination of the gold etching. The local fluctuations in the concentration of chloride ions during the reaction play a decisive role. These fluctuations form a shield around the gold wire and retard the rate of oxidation to control the etching.

Tips characterization

The etched tips are characterized in two steps. At first, the tips are analyzed using the optical microscope. It gives an idea about the geometry of the tip. The

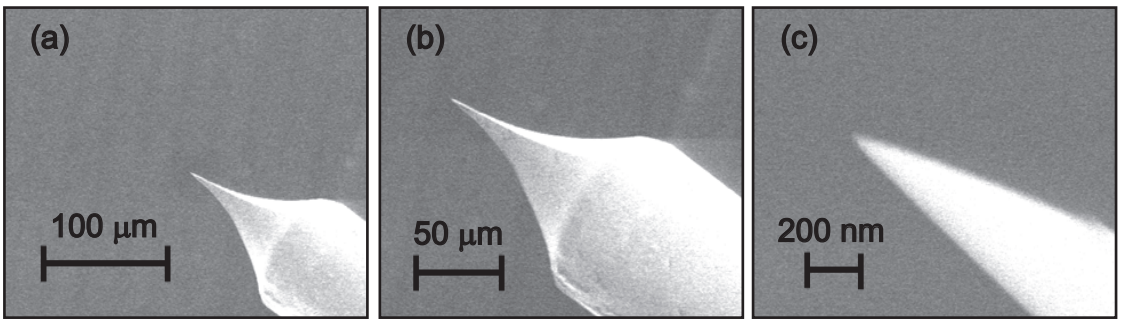

Figure 4.13: Characterization of the gold tip using scanning electron microscopy (SEM). Here, SEM pictures of a tip for three different magnifications (see scale bars) are shown.

microscope picture of the tip is shown in the inset of Fig. 4.12. Tips with satisfactory dimensions are further characterized by scanning electron microscope (SEM). This step is crucial to collect detailed information about the shape and diameter of the tip. The SEM photographs of an annealed gold tip are shown in Fig. 4.13.

The SEM micrograph [Fig. 4.13 (a)] shows a gold tip with a uniform and smooth surface. Figure 4.13 (c) can be used to estimate the diameter of the tip. The diameter of the tip is approximately 20 nm. With the optimized etching setup, we were able to fabricate gold tips with a diameter in the range of 10 - 50 nm with high reproducibility.

4.6 SPM feedback system

Our bespoke instrument allows us to work with two different scanning modes: AFM and STM. In this section, we describe the operations of these modes. Furthermore, we analyze the imaging performance of scanning modes by measuring the topography of test samples.

Our system is equipped with the tapping mode AFM where the tip-sample distance is regulated by a piezoelectric tuning fork [155, 156]. The working schematic of a tuning fork based AFM feedback system is presented in Fig. 4.14.

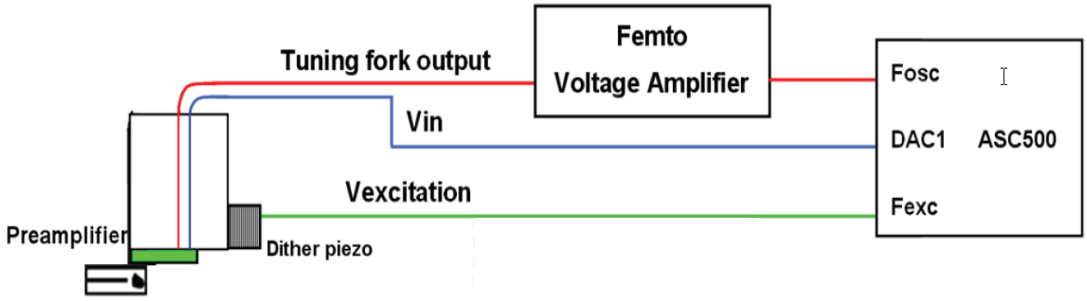

Figure 4.14: Working principle of a tuning fork based atomic force microscope. ASC500 is an electronic chamber which consists of several electronic units. For details and descriptions, see text.

A small dither piezo glued in the proximity of the tuning fork sensor, excites the tuning fork to oscillate at its resonance frequency (32.768 KHz). The excitation signals for a dither piezo are supplied by F_{exc} from the electronic unit ASC500. The oscillations of the tuning fork are converted into current signal and processed in the two-staged amplification process. The input voltage (V_{in}) for the pre-amplifying stage is provided by the digital to analog converter output (DAC1). At first, the pre-amplifier located at the PCB board converts the high impedance piezoelectric current into a voltage. Then, the voltage signals are further amplified using a FEMTO voltage amplifier. Finally, the amplified signals (F_{osc}) are fed into ASC500 unit for the coarse (auto-) approach.

Before the coarse approach is initiated, the setpoint value for the feedback system is provided which is kept constant during the coarse approach. Normally, the setpoint is the value between 80% and 90% of the undamped oscillations amplitude. As the auto-approach begins, damping of the oscillations is observed. The auto-approach monitors the z-position of the feedback system. After every coarse step, the z-scanner tube extends towards the sample surface. If the oscillations amplitude of the tuning fork remains constant, another coarse step is performed. This process is repeated till the oscillations are reduced to the setpoint amplitude. Thereafter, the auto-approach stops. At last, the feedback system is activated for scanning the areas of interest on the sample.

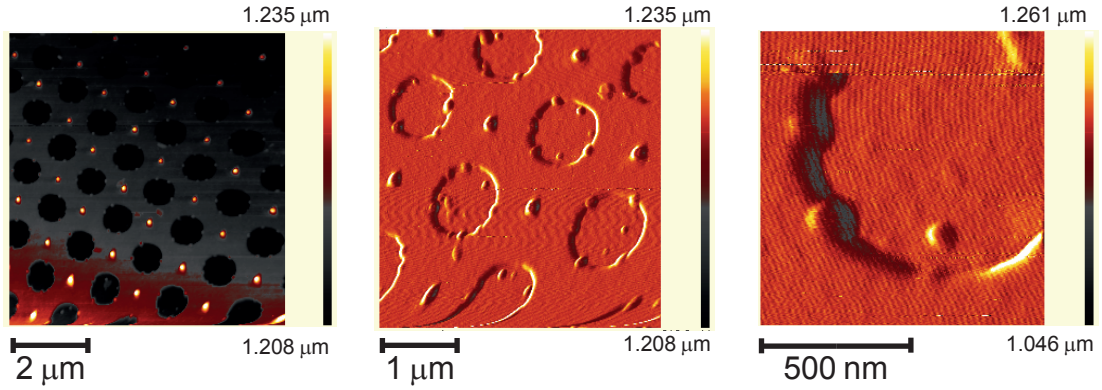

Figure 4.15: Topographic images of a resolution test grid using the tuning fork based AFM in tapping mode. The vertical scale displays the height profile with color code. The scanning patterns were obtained in the backward direction.

Figure 4.15 depicts the AFM images of a randomly selected area of the resolution grid. One can estimate the resolution to be approximately 50 nm. Since these scanning images were measured only for testing purposes, the sample tilt and artifacts (i.e. tip and scanner artifacts) were not considered. Hence we obtain the distorted images. The sample tilt can be corrected by the slope compensation, whereas artifacts can be minimized by varying the proportional (P) and the integral (I) gain values in the feedback channel.

In the following paragraph, we focus on the STM imaging using the same setup. A simplified working principle of the STM feedback is pictured in Fig. 4.16. A sharp metal tip is vertically glued to the bottom prong of the tuning fork. A loop made of platinum wire ($\varnothing = 25\,\mu m$) is knotted around the tip. Silver paste is used to make a stable contact between the tip and the loop. One of the loop ends is connected to the SMA connector of the tip via a contact pad. The sample response is obtained by another SMA connector attached to the copper plate underneath the sample. Both

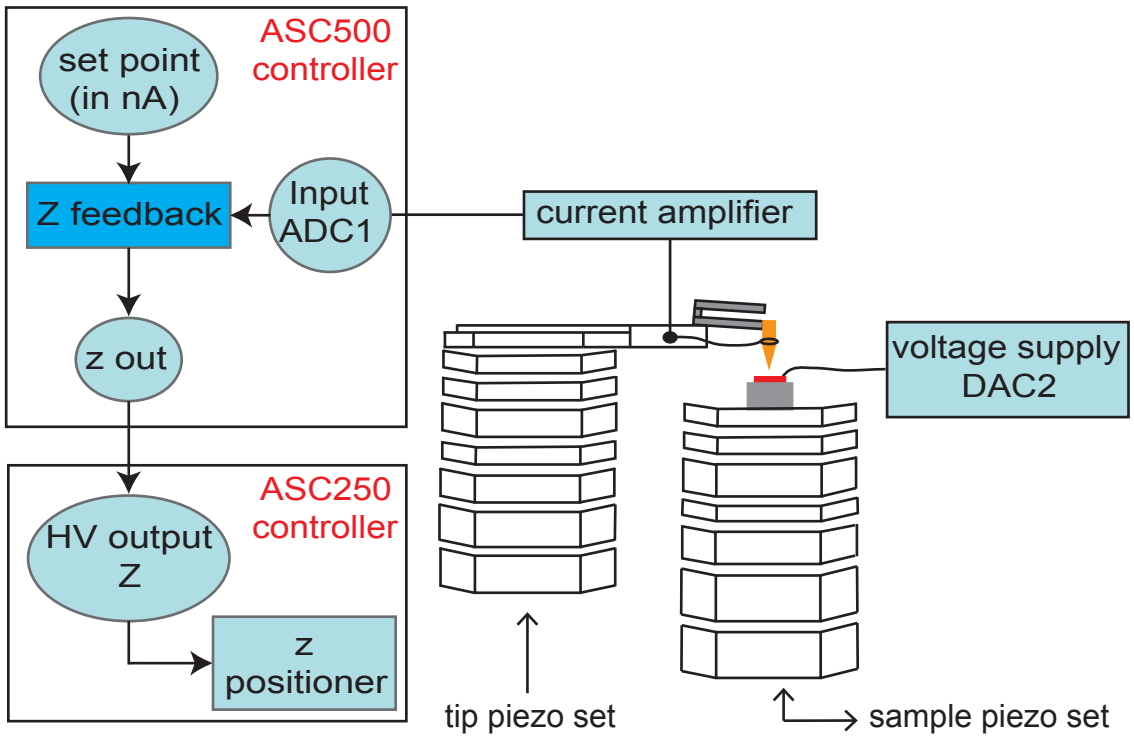

Figure 4.16: Schematic of the STM operation in our TERS setup with several essential components outlined. On the left hand side, two main electronics controlling units (ASC500 and ASC250) are shown.

connectors are coupled to the electrical feedthroughs at the back of the cryostat.

At the beginning of the auto-approach, a bias voltage is applied to the sample by a voltage source DAC2. The typical value for the bias voltage varies between a few mV and a few hundreds of mV. The coarse approach depends on the current setpoint of the z-feedback system. Initially, the set point is kept in the range of a few hundreds of picoamps (pA) for a safe approach. During the coarse approach, the current between the tip and the sample is detected. The detected current is further amplified by the current amplifier and is fed into the z feedback system via ADC1. The response of the tip is passed via z-out to the high voltage (HV) amplifier of the ASC250. The HV amplifier generates the appropriate voltage for driving the z positioner. Once the set point current is obtained, the feedback system is activated to keep the tip in the tunneling regime. Since the feedback system is very sensitive to the tunneling current, the tunneling current is increased gradually up to 5 nA.

The performance of the STM imaging was tested on a gold layer deposited on the silicon substrate via sputtering. The STM images with 100×100 data points were acquired in ambient conditions as displayed in Fig. 4.17. The applied bias voltage

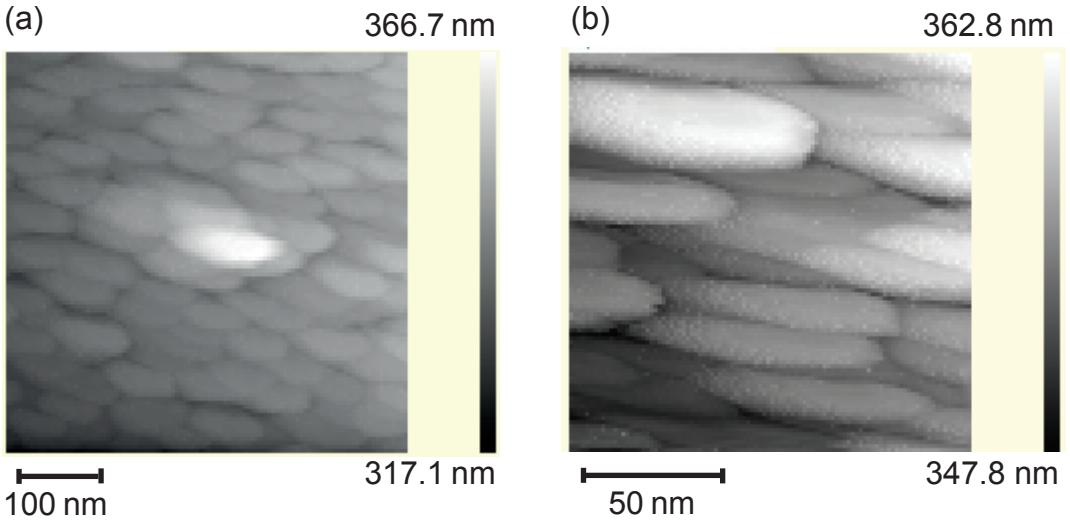

Figure 4.17: STM imaging of the gold layer deposited on the silicon. (a) An image of the random area of the sample surface. The brighter part is the cluster of gold formed during the sputtering. (b) A magnified surface image of the central part of image shown in (a). The grey scale bar represents a variation of the height profile. The image was taken at a bias voltage of 1.34 V with a current setpoint of 1 nA.

(DAC2) between the tip and the sample was 1.344 V for the current setpoint of 1 nA. In order to obtain artifacts-free images, the P and I parameters were simultaneously changed during the scanning. For this specific measurement, P and I values were set to 0 and 27 mHz, respectively. The sample tilt was corrected by inserting marginal values of x = -5% and y = 0% in the slope compensation. In Fig. 4.17 (a), an STM image of a random area of the gold-layered sample is shown. The brighter part is the uppermost cluster of the gold particles formed during the sputtering. In Fig. 4.17 (b), a higher resolution image of the central part of the Fig. 4.17 (a) is presented. Here, the resolution is on the order of 2 - 5 nm. Considering the fact that these measurements were carried out in ambient conditions, the performance of the STM system is already quite promising. Further improvement can be expected when the STM imaging is performed in the UHV conditions.

4.7 Test measurements

This section addresses the initial test measurements on a variety of samples. Furthermore, possible improvements for a successful tip-enhanced Raman study are discussed.

4.7.1 Silicon

Given the ambitious task of demonstrating tip-enhancement, we decided to first measure the enhancement on the silicon sample using STM mode. These measurements were carried out in ambient conditions unless stated otherwise. It is also important to mention that the optical elements placed between the objective (O1) and the optical fiber (see Fig. 4.4) belong to the modified optical setup and were not used for these measurements. The details of the modified optics can be found in subsection 4.7.2.

The Si spectrum (red) presented in Fig. 4.18 is the far-field spectrum measured in the retract mode. Here, the tip is far away from the sample and does not contribute to the spectrum at all. Hence, this spectrum is a result of conventional Raman process. In the tunneling regime (black), the phonon intensity is found to be decreased rather than enhanced. In addition, a significant increase in the background signals is also observed. This clearly signifies that either no enhancement is produced or it is overcompensated by other effects.

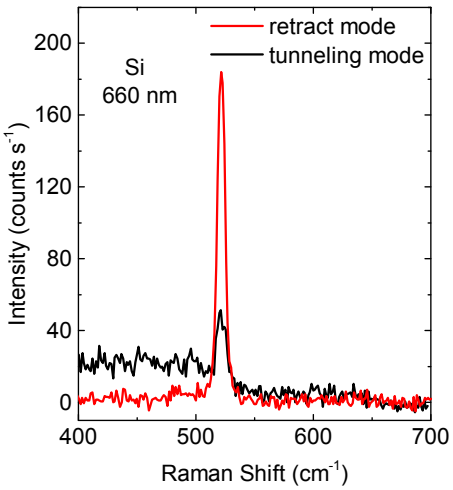

Figure 4.18: Raman spectra of silicon with an attempt of tip-enhancement. The spectra were measured with the 660 nm laser line. The retract mode spectrum (red) shows the conventional far-field spectrum of silicon with a pronounced peak at 520 cm^{-1}. The spectrum in black is associated with the tunneling mode.

After several attempts, we could assign the signatures of decreased intensity and increased background. The background signals are apparently increased due to the coupling of direct reflection in the fiber core where they cause luminescence. A decrease in the Raman intensity could be associated with the shadow effects originating from the inappropriate tip positioning. The consequences of shadow effects in the TERS geometries are elaborated by Mehtani *et al.* [95]. The luminescence effects could be reduced by using an edge filter before the optical fiber. The proper positioning of the tip can be accomplished by scanning the tip point by point in close vicinity of the area of interest with slower feedback. An individual spectrum at each pixel could provide an overview of the selected area in order to find an appropriate tip position on the sample.

Meanwhile, we realized that the choice of silicon sample for proving the principles of tip-enhancement could be a challenging task. For thick samples like silicon, contrast between the far- and near-field signals is close to unity [23]. This would require a nearly perfect focus on the sample. Also, a significant variation in the penetration depth of bulk silicon for different wavelengths could lead to additional complications. For silicon, the laser wavelengths of 514.5 and 647 nm penetrate roughly about 0.68 and 3 µm, respectively [184]. This implies that the far-field volume for the red laser is approximately 4.5 times larger than the green laser. According to the relation between the enhancement factor and penetration depth (see Eq. 3.7), such volume differences could lead to a substantial decrease in the observed enhancement.

4.7.2 $YBa_2Cu_3O_7$

Domains in materials with different lattice parameters are a common phenomenon. In materials such as $YBa_2Cu_3O_{6+x}$ and $BaFe_2As_2$, the domain size is on the order of a few tens of nanometers. There are only a few tools available enabling access to the vibrational and electronic properties of such small domains. Recent reports of local strain studies on graphene [30] and WSe_2 films [31] indicate that the TERS systems are capable of accessing such novel properties. We intended to measure an $YBa_2Cu_3O_7$ (YBCO) sample in order to gain access to its lattice and carrier dynamics. Besides that phonon characteristics of YBCO will be utilized to calibrate the spatial resolution of our system.

YBCO belongs to the family of high-temperature superconductors (HTSC). It is a bi-layer system where the crystal structure is characterized by two Cu-O planes per unit cell. In optimally doped YBCO, there is an oxygen apex vibration at 500 cm^{-1} having A_{1g} symmetry [185]. In the case the crystallographic c-axis being oriented perpendicular to the sample surface, the z direction coincides with the tip apex. Moreover, additional enhancement is expected when the electric field component of the excitation light is polarized parallel to the plane of incidence (p-polarization) with a finite projection along the tip shaft [111]. This matching configuration of light polarization and the A_{1g} phonon can offer a considerable signal gain, making YBCO an ideal choice for the proof of principles. In addition, we specifically select the A_{1g} phonon, as the far-field Raman response is very low in A_{1g} symmetry due to limited z-axis projection in the bulk. A significant difference between the intensities of far- and near-field signals could be useful to achieve higher contrast gain.

Here we estimate the contrast between the far- and near-field signals for the A_{1g}

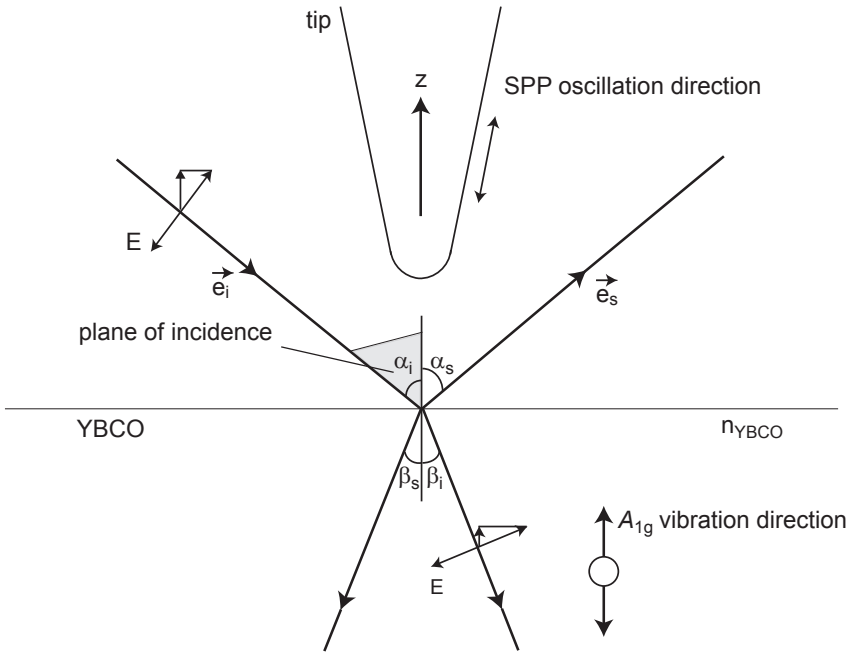

Figure 4.19: Sketch of the light polarization (p-polarization) with respect to the tip-sample geometry. The projection of the polarization vector onto the z-axis is smaller in the bulk due to that fact that, the refractive index of YBCO (n_{YBCO}) is larger than 1. Here, directions of the surface plasmon polaritons oscillations and the oxygen apex vibration are along the z-axis. This configuration leads to a higher contrast in the TERS measurements.

phonon of YBCO using the relation of the Raman intensity. An expression for the total Raman intensity reads as

$$I_\mu \propto |\vec{\mathbf{e}}_s^* R_\mu \vec{\mathbf{e}}_i|^2. \tag{4.1}$$

Here I_μ is the resultant Raman intensity, R_μ is the Raman tensor matrix of symmetry μ ($=A_{1g}$). $\mathbf{e}_i$ and $\mathbf{e}_s$ are the polarization vectors of incident and scattered photons, respectively. In the case of tetragonal-structured YBCO, the Raman tensor matrix for the A_{1g} symmetry (R_{A1g}) has the following form:

$$R_{A1g} = \begin{pmatrix} a & 0 & 0 \\ 0 & a & 0 \\ 0 & 0 & b \end{pmatrix}$$

The schematic of the p-polarized light projection with respect to the YBCO sample is depicted in Fig. 4.19. In the case of conventional far-field scattering, for simplicity we assume $|\vec{e}_i| = 1$. According to the Snell's law, the relation between the angles of incidence (α_i) and refraction (α_s) is given as

$$\frac{\sin\alpha_i}{\sin\beta_i} = n_{YBCO}, \tag{4.2}$$

where n_{YBCO} is the refractive index of YBCO and is equal to 1.69 [186]. Since $n_{YBCO} \gg 1$, the projection of the polarization vector onto the z-axis is much smaller in the bulk which results in the low A_{1g} phonon intensity. The z-components for the incident and scattered light are $z_i = \sin\beta_i$ and $z_s = \sin\beta_s$. The far-field Raman intensity is

$$I_{far} \propto |z_s b z_i|^2 = b^2 \left(\frac{\sin\alpha_i}{n_{YBCO}} \cdot \frac{\sin\alpha_s}{n_{YBCO}} \right)^2 \tag{4.3}$$

When the tip is brought closer to the sample, the directions of the SPP oscillations and the A_{1g} phonon coincide with each other leading to a higher intensity. In this case, the z-components for the incident and scattered light will be $z_i = \sin\alpha_i$ and $z_s = \sin\alpha_s$. The Raman intensity of the near-field is

$$I_{near} = b^2 (\sin\alpha_i \cdot \sin\alpha_s)^2 \tag{4.4}$$

Using Eq. 4.3 and Eq. 4.4, the contrast between the near- and far-fields for the A_{1g} phonon can be estimated. This yields

$$\frac{I_{near}}{I_{far}} = n_{YBCO}^4 \approx (1.69)^4 \approx 8.15 \tag{4.5}$$

Note that this result is independent of the angles of incidence and the scattered light. Eq. 4.5 indicates that the high contrast can be expected due to coincidence of light polarization, surface plasmon oscillations, and the A_{1g} phonon of YBCO.

Figure 4.20 shows the far-field Raman spectrum of optimally doped single crystalline YBCO. The measurement was carried out in the range of 80 to 750 cm^{-1} with a laser power of 3 mW as measured in front of the central window (W2) of the cryostat. In the spectrum, up arrows (↑) indicate the phonon peaks at 110, 147, and 339 cm^{-1}. The phonon peak at 495 cm^{-1} is also present, however its characteristic shape seems to be strongly influenced by the external effects. If we compare our results with the silica spectrum (in the inset) [187], both spectra look similar especially at the higher energy region. The coupling of the elastic stray light into the silica core of the fiber causes luminescence. In the case of YBCO, the luminescence dominates the spectrum in the higher energy region.

To prevent elastically scattered light to enter into the fiber, we have modified the collection optics by adding an edge filter in the parallel beam path of the collection

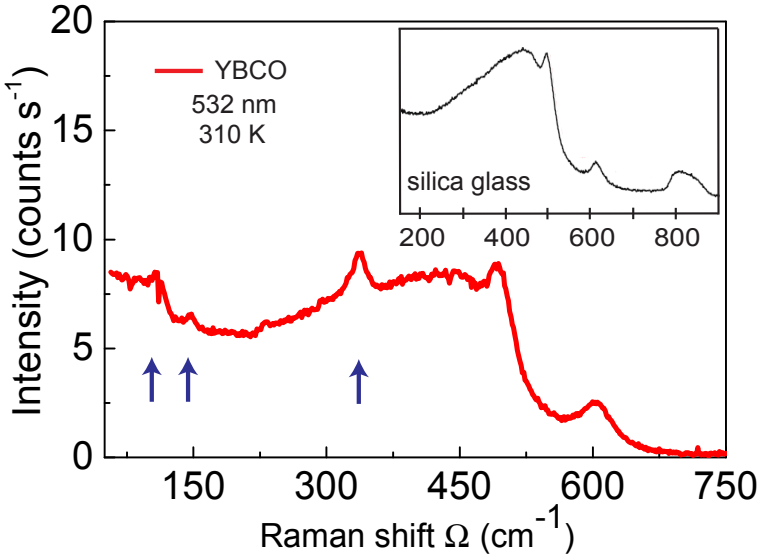

Figure 4.20: The Raman spectrum of an optimally doped YBCO. The arrow signs (↑) refer to the phonon peaks. In the inset, the Raman spectrum of silica glass is presented. The silica spectrum is adopted from Ref. [187].

optics. The ray diagram of the modified optics between the camera objective (O1) and the fiber coupling is depicted in Fig. 4.21. Here an edge filter (F1) in combination with two achromatic lenses (L3, L4; f = 19 mm) is installed. Due to the insertion of additional optical components, the intensity coupled into the fiber is reduced by approximately 35% of the total intensity.

Apart from the edge filter, a spatial aperture is incorporated in the collection optics for gaining the contrast between the far- and near-field signals. An aperture

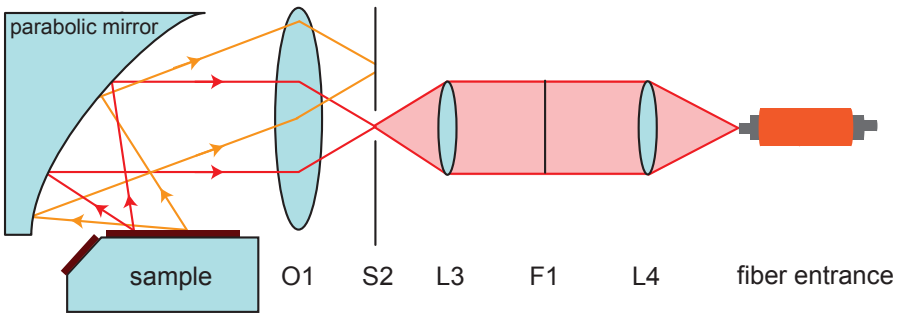

Figure 4.21: Optical arrangement of the modified optics for collecting the scattered light. The optical components S2, L3, F1, and L4 belong to the modified optics. F1 represents the edge filter. For further details, see text.

suppresses the far-field signals by blocking the scattered light coming from the outer region of the focal spot on the sample. The inelastically scattered light not originating from the exact focus of the parabolic mirror does not propagate parallel to the optical axis and is consequently blocked by the aperture. Prior to measuring the tip-enhancement, it is necessary to test the performance of the modified optical system to its limit. In this context, the influence of the modified optics on the Raman intensity was studied thoroughly and is discussed in the following paragraph.

The Raman measurements of the silicon sample using the modified optics are presented in Fig. 4.22. Since the silicon phonon has a higher Raman response, it is

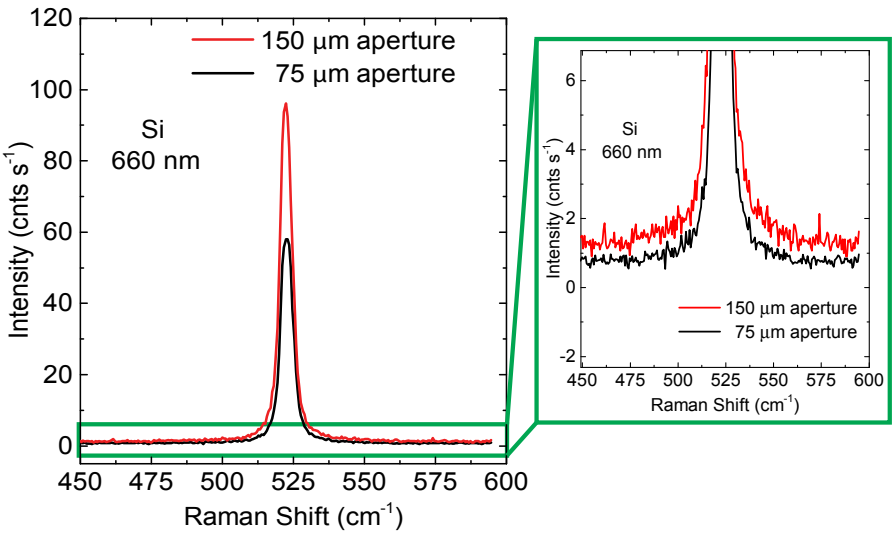

Figure 4.22: Dependence of the far-field silicon spectra on the diameter of the spatial aperture (S2). The magnified spectra show a reduction of the background signals by 30%.

an ideal choice for testing the alignment of the modified optics especially the spatial aperture (S2). The far-field spectra of silicon look promising as the control over the coupling of elastic stray light is feasible. The prominent role of the edge filter will only be visible once we measure the samples with low phonon intensities such as YBCO. However, the role of the spatial aperture is clearly observed in the silicon spectra. When the aperture diameter is reduced from 150 to 75 µm, a better control of the background signals is facilitated. From the magnified spectra (Fig. 4.22), we find that the background signals are reduced approximately by a factor of 2 in the case of smaller aperture diameter. The intensity of the silicon phonon was also decreased for the aperture diameter of 75 µm. These are only the preliminary results. Our aim is to push the limit of the aperture diameter down to 5 µm in order

to suppress the far-field signals efficiently.

4.7.3 Selection rules for silicon

The selection rules play a vital role in determining the symmetry of excitations appearing in the Raman spectrum. Since our customized TERS setup enables us to access the polarization, it is important to understand the Raman response with respect to different incoming and outgoing polarization states. Also, the polarization-dependent study is useful to improve the contrast between the near- and far-field signals. According to the definition of the contrast in Eq. 3.3, the contrast can be infinity for the case of perfect selection rules. At the current stage, the contrast gain is utmost necessary in order to demonstrate the enhancement using our system.

We perform polarized Raman scattering experiments to verify the selection rules using silicon samples. Silicon has a cubic diamond structure. For single-crystalline silicon, the Raman spectrum has a phonon peak at $520\,\mathrm{cm}^{-1}$ obeying T_{2g} symmetry. As this phonon is very pronounced and narrow, silicon is widely used for calibration purposes in Raman spectroscopy. The Raman spectrum of silicon also contains two other phonon modes (A_{1g} and E_g) at $305\,\mathrm{cm}^{-1}$ and $950\,\mathrm{cm}^{-1}$. However, these modes are not appropriate for the studies of selection rules due to their weak intensities. The Raman response is generally described using the Raman tensor which allows one to determine the projection of different symmetries depending on the polarization of incoming and scattered photons. We calculate the Raman intensity of the T_{2g} mode for two polarization states (xy and xx). The relation between the Raman intensity and polarization states is given as

$$I_{\mathrm{R}} \propto |\vec{\mathbf{e}}_s^{*} R_\mu \vec{\mathbf{e}}_i|^2. \tag{4.6}$$

Here I_{R} is the resultant Raman intensity, R_μ is the Raman tensor matrix of symmetry $\mu\,(= A_{1g}, E_g, T_{2g})$. $\mathbf{e}_{\mathrm{i}}$ and $\mathbf{e}_{\mathrm{s}}$ are the polarization vectors of incident and scattered photons, respectively. For silicon, the Raman tensor matrix for the T_{2g} symmetry (R_{T2g}) can be written as

$$R_{\mathrm{T2g}} = \begin{pmatrix} 0 & d \\ d & 0 \end{pmatrix}$$

The Raman response can now be calculated using the above expressions for different polarization configurations. For the xy polarization configuration, we obtain the

intensity of the Raman response as

$$I_{\mathrm{T2g}} \propto |\vec{\mathbf{e}}_s^{*} R_{\mathrm{T2g}} \vec{\mathbf{e}}_i|^2 = \left| \begin{pmatrix} 1 & 0 \end{pmatrix} \begin{pmatrix} 0 & d \\ d & 0 \end{pmatrix} \begin{pmatrix} 0 \\ 1 \end{pmatrix} \right|^2 = d^2. \tag{4.7}$$

Similarly, the Raman response can be extracted for the polarization combination of xx

$$I_{\mathrm{T2g}} \propto |\vec{\mathbf{e}}_s^{*} R_{\mathrm{T2g}} \vec{\mathbf{e}}_i|^2 = \left| \begin{pmatrix} 1 & 0 \end{pmatrix} \begin{pmatrix} 0 & d \\ d & 0 \end{pmatrix} \begin{pmatrix} 1 \\ 0 \end{pmatrix} \right|^2 = 0. \tag{4.8}$$

The T_{2g} mode is projected in xy configuration but not in the xx polarization. Due to the cubic crystal structure of silicon, it can be concluded that the xy, xz, and yz polarizations will provide an equal and maximum response. It is noted that the xz combination would be very important when we introduce the tip component in the selection rules as the z-component of the electric field is strongly enhanced. Similarly, in other configurations such as xx, yy, and zz, one expects no contribution from the T_{2g} mode.

In the following experiments, we measure only the far-field selection rules. Figure 4.23 summarizes the in-plane polarization projections with an arrangement of the silicon atoms together with the laboratory coordinate system. For Si, the polarization orientation xy selects T_{2g} symmetry and xx configuration gives the combined contribution from A_{1g} and E_g. The laboratory coordinate system is set with respect to the crystal axes of the sample (i.e. x is parallel to the a axis). The x and y axes are parallel and perpendicular to the silicon sample, respectively.

Figure 4.24 presents the results of the symmetry analysis of silicon using various parts of the aperture of the parabolic mirror. These measurements were carried out with the optical setup illustrated in Fig. 4.4. All spectra were measured with the excitation wavelength of 660 nm. The laser power was measured in front of the cryostat and was kept constant at 4 mW for the quantitative measurements. The acquisition time for each measurement was 60 seconds.

As shown in Fig. 4.24 (a), the xy configuration shows the prominent peak owing to the T_{2g} symmetry. From Eq. 4.8 we do not expect any response of the T_{2g} peak in xx configuration. However, we clearly see the peak having about 10% of the intensity of the xx polarization. In terms of contrast, we observe a contrast between the xy and the xx spectra with the ratio of the peak intensities being approximately 10. Similarly, in yy symmetry, we find the contribution from the T_{2g} peak with about 50% of the intensity of the xy symmetry. The contrast between yy and yx spectra is close to unity. These results suggest that the parabolic mirror does not preserve

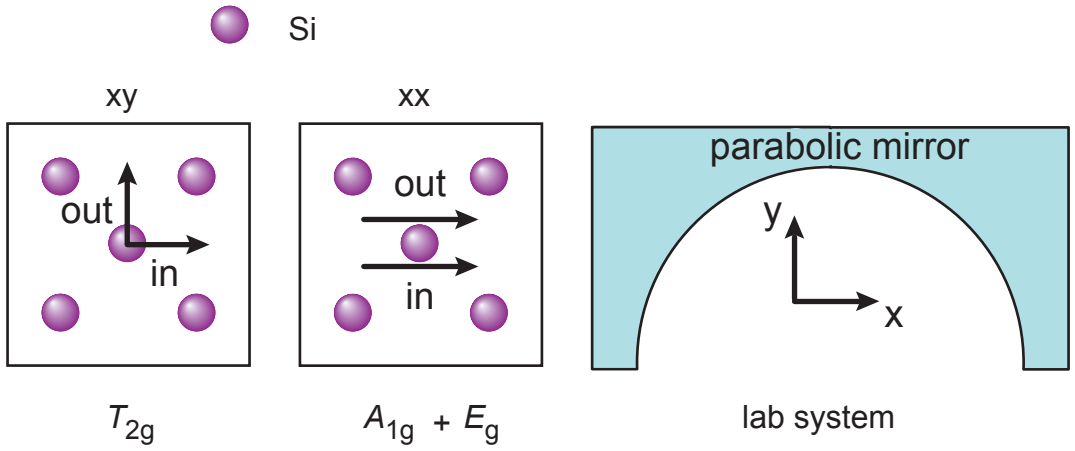

Figure 4.23: Schematic illustration of scattering geometry of incoming (in) and scattered (out) photons together with the projected symmetries with respect to crystallographic axes. x and y correspond to the coordinate system in the laboratory.

the polarization states completely. However, for some polarization combinations the selection rules can be maintained to within approximately 10%.

This can further be scrutinized by comparing the response from different areas of the parabolic mirror. Considering only the central part of the parabolic mirror, x and y polarizations outside the cryostat will be polarized parallel to x and y', respectively, on the sample. Here y' is the polarization state rotated by 45° with respect to the y polarization direction. If other sections of the parabolic mirror are also taken into consideration, several other orientations will contribute to the overall intensity profile. An incident x-polarization always projects a polarization close to x on the sample irrespective of light projection from either quadrant of the parabolic mirror. For scattered photons along the y direction, several other polarizations (between x and y) contribute resulting in a gain of the peak intensity. Similarly, for the incident y-polarized light, the polarization on the sample is between x' and y. For the scattered light polarized along the x direction the photons in the sample are always approximately polarized along the crystallographic axes in the sample for the whole area of the parabolic mirror resulting in the low intensity phonon peak.

In a second set of spectra, presented in Fig. 4.24 (b-d), contribution from selected parts of the parabolic mirror are studied. All spectra were measured by directing the incident beam in the middle of the left quadrant of the parabolic mirror. Figure 4.24 (c) and (d) show the response of right and left quadrants, respectively. In xy configuration, contribution from the left and the right quadrants are approximately equal, whereas in xx configuration the peak intensity of the left quadrant is

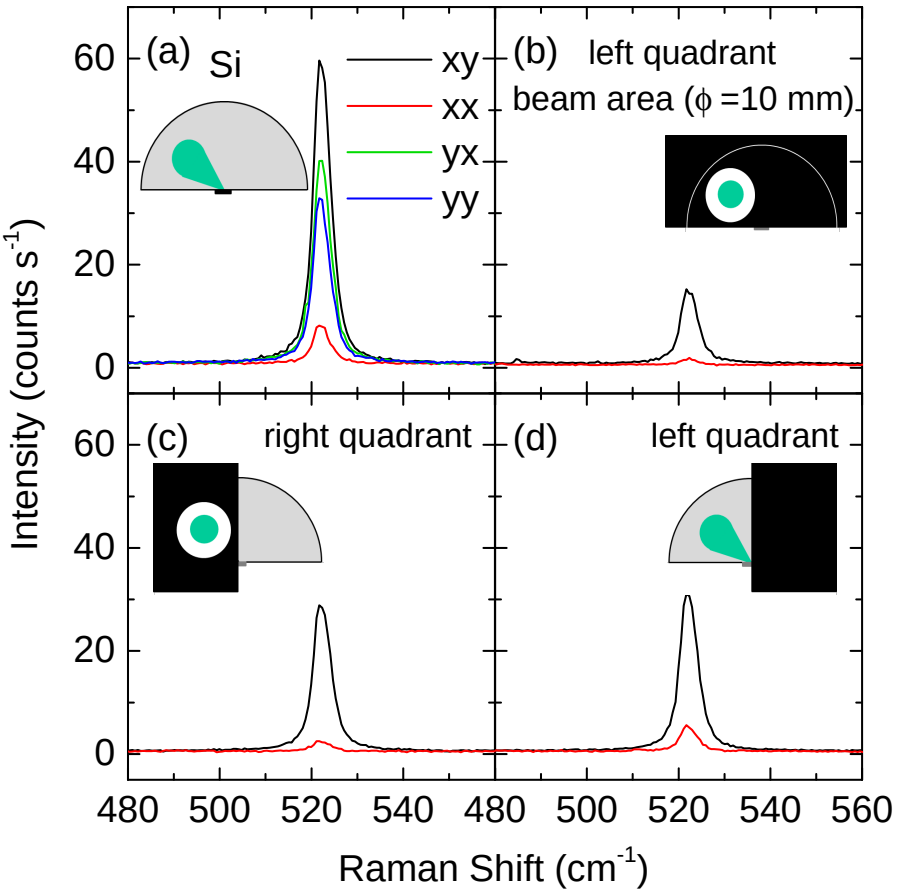

Figure 4.24: Far-field spectra of silicon. (a) Four different polarization settings of xy, yx, yy, and xx with the scattered light collected from the full parabolic mirror. The incident laser beam always hits the left quadrant of the parabolic mirror. (b)-(d) Silicon spectra with two different polarization combinations xy and xx collecting scattered light from different parts of parabolic mirror. From [188].

stronger by a factor of 2.5 than that of the right quadrant. The xx configuration from the right and left quadrants carries about 8% and 18% of the intensity, respectively compared to the xy configuration. The intensity ratios for the right and left quadrants are approximately 12 and 6, respectively. All these factors indicate that the polarization states are better preserved in the right quadrant of the parabolic mirror. In Fig. 4.24 (b), we present the results from the area reduced to an aperture with 10 mm diameter around the laser beam (left quadrant). In xy and xx configurations, the intensities are further reduced to a minimum but the contrast is restored. The intensity reduction in this case corresponds approximately to the ratio of the areas of the parabolic mirror and the aperture with 10 mm diameter.

The major effects altering the polarization of incoming and scattered light come from the geometry of the parabolic mirror which makes the validation of the se-

lection rules difficult using our TERS setup. One of the important effects includes rotation of the polarization directions after reflecting from the mirror. In this case, for the incoming x- and y-polarizations, an intensity correction would be sufficient since the polarizations are conserved with respect to the plane of incidence. However, the interpretation of the scattered light is not easy since the scattered light is collected from the entire parabolic mirror. Each scattered beam from the sample incidents at different angle on the parabolic mirror and reflected differently influencing the overall polarization of the scattered light. Another effect comprises a phase shift between the incoming and scattering light introduced due to the reflective coating (aluminium) of the parabolic mirror. A phase shift in the incoming and scattering light can generate elliptical polarizations instead of linear polarizations on the sample. In our case, the intensity gain in xx and yy symmetries could be the result of a finite elliptical polarization at the sample surface. The possible solution to treat the elliptical polarization is to use a compensator in the optical path of the incoming beam. The compensator allows one to shine elliptically polarized light on the parabolic mirror resulting in well-defined polarizations on the sample surface. In this case, one would expect to have no peak in xx and yy configurations owing to the perfect selection rules. All these effects would be necessary to further explore for the studies of the selection rules using our TERS setup.

4.8 Outlook

Due to various complex issues, tip enhancement could not be realized to date. Yet, many challenging aspects of the customized setup have been perceived. There are a few upgrades which need to be implemented prior to demonstrating the enhancement. This mainly includes redesigning parts of the optical setup, understanding the polarization issues, and selection of the appropriate samples.

At the current state, the foremost challenge is to understand the polarization issues encountered during the symmetry analysis of silicon. It requires a modification of the incident light path by adding a few optical components such as a half-wave plate and a compensator. A half-wave plate after the polarizer P1 (see Fig. 4.4) will be useful to retain the projection of the incident beam. A compensator will be useful for projecting the elliptical polarized light on the sample so that, a well-defined polarization study could be performed.

Instead of the collection optics based on the optical fiber, analysis of the scattered light using a separate spectrometer would be essential. The optical fiber is

responsible for a huge loss of the scattered intensity while transmitting the light from the TERS laboratory to the spectrometer located in another laboratory. In addition, it could play a decisive role in determining the selection rules necessary for the execution of the polarization-dependent Raman measurements.

A parabolic mirror based TERS geometry is quite challenging especially for the tip imaging. In this geometry, the accurate placement of the tip at the focal point is far more complicated in comparison to the microscopic objective based geometry. A systematic approach for finding an appropriate area of interest on the sample surface could be the tip scanning. This approach involves measuring a single spectrum at every pixel while scanning the tip all over the focal region. In this approach, one needs to deal with a lot of spectral data which makes the data evaluation more complex and time consuming. To solve this problem, it is planned to customize a software which could measure the Raman response at any interesting pixel of the scanning map. This could also provide an additional feature of mapping the intensity distribution of any particular Raman shift of interest.

Prior to making progress with the tip-enhanced measurements, the selection of the appropriate test samples is recommended. Most of the TERS literature reveals that the molecular systems are the first choice for the TERS measurements [23, 25]. These systems are capable of generating strong signals from the subwavelength volume beneath the tip shaft. For example, malachite green isothiocynate (MGITC) which is an organic green laser dye with the molecular weight of 364.92. The molecular structure of the non-fluorescent MGITC dye molecule is illustrated in Fig. 4.25 (a). It is a triarylmethane dye with good binding properties. The sample is prepared by depositing the molecular layer on the gold substrate due of the fact that, the sulfur atom of isothiocynate group binds strongly with the gold. A tendency of good binding provides a stable and well defined geometry of the absorbed molecules even for ambient conditions. Moreover, the absorption spectrum of MGITC molecule [presented in Fig. 4.25 (b)] shows a strong absorption peak that coincides well with the wavelength of the red laser and the plasmonic response of the gold tip. Summing up all the important properties, this system could be an ideal sample for a proof-of-principle TERS measurements.

The design of piezo systems embedded in the microscopic head also requires some modifications, especially the tip stack (see Fig. 4.3). In our system, the parabolic mirror collects the light from all the scattering directions. The gain in the scattered photon counts is compromised by the fact that, the plate holding the tuning fork blocks at least one third of the aperture of the parabolic mirror, leading to an in-

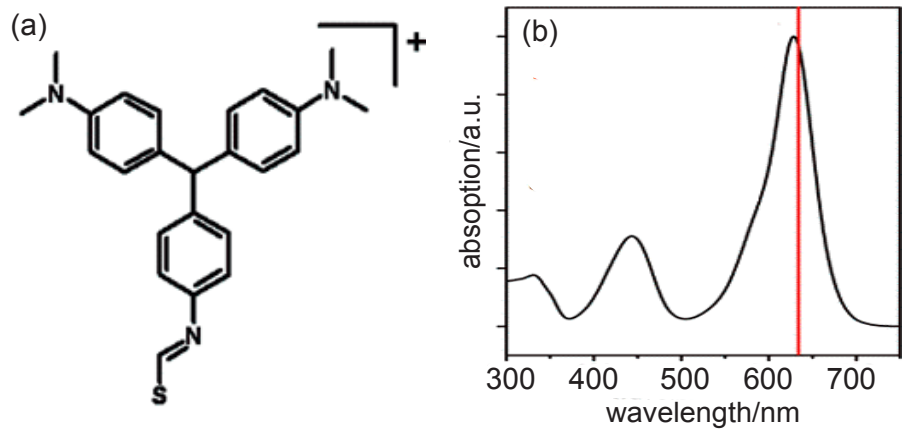

Figure 4.25: Malachite green isothiocynate (MGITC). (a) Molecular structure of MGITC. (b) Absorption spectrum of MGITC with red line indicating the maximum absorption close to 660 nm.

tensity loss. In addition to the advancements discussed above, a few more upgrades would be beneficial to perform the TERS measurements more reliably such as fabrication of silver tips. The availability of silver tips would be a useful extension to perform the TERS experiments in the broad range of wavelength. The plasmonic properties of the silver tips are favorable for the green excitation source which would allow one to cover a larger energy range due to the gratings of the spectrometer.

Chapter 5

Magnetic excitations and amplitude fluctuations in undoped cuprates

Spin order, excitations and fluctuations play a key role not only in magnetism but also in ordering phenomena such as charge modulations or superconductivity [189–192]. In the specific case of high-T_c superconductors (HTSC) with CuO_2 building units, the observation of superconductivity in the proximity of static magnetic order suggests that magnetic ordering and superconductivity are interrelated [193]. Moreover, one manifestation of strongly correlated electron systems is the insulating antiferromagnetic (AF) ground state developing at half filling when the material is expected to be metallic. Considering all the facts, the study of magnetic properties in undoped parent compounds is of fundamental importance in order to characterize the interrelation between superconductivity and magnetism.

There are a few powerful spectroscopic techniques which have been utilized to characterize spin correlations in AF phases. Frequently used methods are inelastic neutron scattering (INS) [41, 42] and resonant inelastic x-ray scattering (RIXS) [194, 195]. Among other techniques, inelastic light scattering (Raman) has also been widely used for probing magnetic excitations [1, 9, 43].

Over the years, a large amount of Raman experimental data have been amassed on the spin properties of the undoped cuprate systems starting from the first experimental results on undoped La_2CuO_4 [1, 4, 11] and Gd_2CuO_4 [13]. The results obtained so far have been proved to be robust at least in the B_{1g} symmetry channel which essentially probes the so-called two-magnon scattering, i.e. the simultaneous flip of two neighboring spins. The characteristic feature of B_{1g} symmetry in

the form of a broad and asymmetric peak is found to be almost the same in all insulating CuO_2 compounds. Apart from the observation in undoped parent compounds, the two-magnon Raman scattering also persists in materials with different doping levels. There have been reports where two-magnon scattering was observed in Y123 systems up to optimal doping [10, 15] whereas in Bi2212 samples, scattering from the two-magnon excitations was possible to observe up to the doping level of $p = 0.20$ [196]. Except for undoped cuprates, two-magnon scattering is also reported in different compositions of iron selenide [197] and some iridate compounds [198].

From a theoretical point of view, there has been a great interest to gain insight into the scattering processes by magnons and AF fluctuations especially in the insulating parent compounds [15, 43, 44, 50]. Most of the theoretical work for the magnetic properties of undoped antiferromagnetic cuprates is described by modeling the CuO_2 layers by a spin 1/2 Heisenberg model on a square lattice [14]. While most of the properties can qualitatively be described in terms of spin-wave theory in a Heisenberg model with only nearest neighbor exchange coupling, some of the anomalous features of the spin wave excitations, such as the line shape, are yet to be solved [47, 199].

In this chapter, the main emphasis is placed on the Raman study of the magnetic excitations in the series of undoped insulating cuprates as a function of polarization and excitation energy. The chapter is organized as follows: The phase diagram of the cuprate systems is discussed in section 5.1. The crystallographic and magnetic properties of the parent compounds are subsequently presented in subsections 5.1.1 and 5.1.2, respectively. Subsection 5.1.3 provides a brief introduction to the light scattering by magnons in antiferromagnetic systems which is discussed in the context of the pioneering work of Fleury and Loudon [9]. The basic preparation of the studied samples and the experimental Raman scattering setup are presented in section 5.2. Section 5.3 covers the analysis of the experimental data of three different cuprate systems: La_2CuO_4 (LCO), $YBa_2Cu_3O_{6.05}$ (Y123), and $Bi_2Sr_2YCu_2O_{8+\delta}$ (Bi2212:Y) to describe the overall (intrinsic) line shape close to the double spin-flip maximum in the B_{1g} symmetry.

5.1 The cuprates - theoretical aspects

The family of the cuprates belongs to the transition metal oxides consisting of planar CuO_2 layers sandwiched between the insulating charge reservoir layers. The layered structure of such materials comprising one or more CuO_2 planes per unit

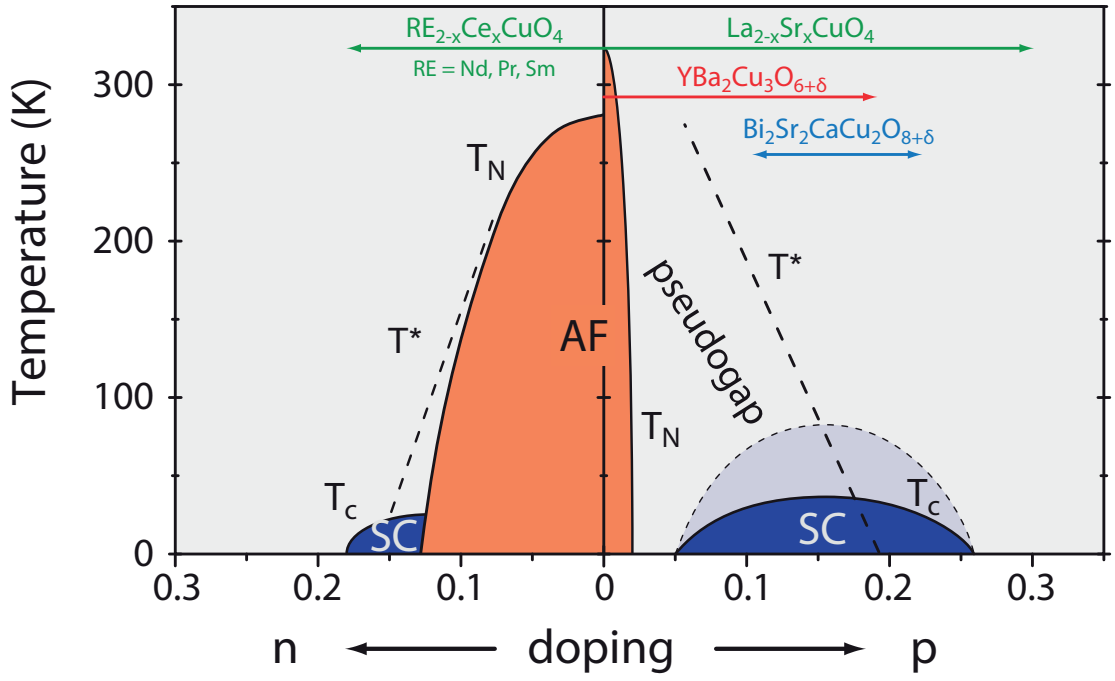

Figure 5.1: Schematic phase diagram of the copper-oxygen based superconductors displaying electron- and hole-doped regions on the left and right panels, respectively. At zero doping, an AF state emerges below the Néel temperature (T_N). The superconducting phase (SC) always emerges from a magnetically ordered state. At optimal doping ($p = 0.16$), SC has its maximum T_c. Apart from AF and SC states, several other ordering phenomena are observed which are shown in the form of different phases and crossover lines. In hole-doped cuprates, three different families LSCO, YBCO, and BSCCO are illustrated with arrows indicating the accessible doping range. Taken from Ref. [200].

cell arranged in a square lattice. The electron confinement and strong interactions take place in the CuO_2 planes due to a strong anisotropy between a-b and c-axis of the layered compounds [201]. The variation in the environment of the CuO_2 planes results in adding or removing charge carriers. Depending on the material class, the CuO_2 planes can be doped either with electrons or holes. The majority of the cuprate families belong to the hole-doped (p-type) compounds. There are also a few electron-doped materials (n-type). Doping leads to new phenomena such as superconductivity, spin and charge order, and pseudogap phenomena [202, 203] resulting in a rich phase diagram [204]. The phase diagram of the high-T_c cuprates is nearly universal and presented in Fig. 5.1. From here on, our further discussion will mainly focus on the series of hole-doped compounds.

The parent compounds are insulators with antiferromagnetic ordering highlighting an important role of the Coulomb interaction U. The Néel temperature for

these compounds is on the order of room temperature. As the hole concentration is increased, the Néel temperature decreases and the long-range antiferromagnetically ordered state vanishes completely close to $p = 0.02$ [205]. When the compounds are further doped with holes, the new states of matter appear including superconductivity, the pseudogap phenomenon and inhomogeneous phases. Superconductivity (SC) exists in the broad doping range between 0.05 and 0.27 with the maximum of the transition temperature T_c at $p = 0.16$; known as the optimal doping. Another anomalous region labeled with T^* is observed which is associated with the opening of a momentum-dependent gap known as pseudogap [206].

In the following, we explore different properties of the lanthanum copper oxide (LCO) as the main archetypical cuprate compound.

5.1.1 Crystal structure

La_2CuO_4 is the parent compound of the 214 family which belongs to one of the most studied families of high-T_c superconductors. Undoped LCO is a Mott insulator that orders antiferromegnatically with the Néel temperature of $T_N = 325\,\mathrm{K}$ [207].

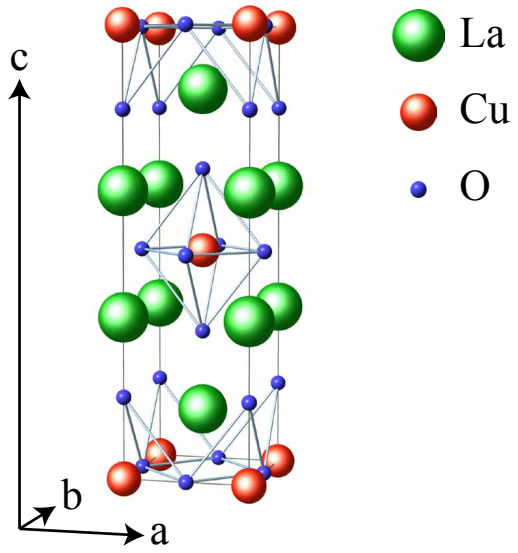

Figure 5.2: Crystal structure (T-structure) of La_2CuO_4. The conventional unit cell contains two CuO_2 planes. The copper atom (red) in the center is surrounded by four La^{3+} atoms (green) on each side. Each of the Cu atoms is surrounded by octahedra of O atoms (blue). Adopted from Ref. [209].

The crystal structure of the single layer LCO compound (also known as T-structure), as illustrated in Fig. 5.2, is characterized by a body-centered tetragonal structure (space group I4/mmm). The stoichiometric structure possesses the CuO_2

planes separated by the two LaO planes acting as a charge carrier reservoir and spacer. The lattice constants for the tetragonal phase of T-LCO are $a = b = 3.803$ Å and $c = 13.150$ Å [208].

5.1.2 Magnetic properties

In the case of undoped La_2CuO_4, the ionic configuration includes non-magnetic ions of La^{3+} and O^{2-}. In order to compensate the charge, the copper atom has to have an ionic state of Cu^{2+}. Assuming charge neutrality, the Cu^{2+} ions have an [Ar]$3d^9$ configuration. According to the band theory, this configuration predicts a metallic state due to the half-filled $3d$ shell which is expected to lead the electronic conduction. However, inclusion of the Coulomb repulsion mechanism corrects the picture where localized electrons form a Mott insulator. In the $3d^9$ configuration, LCO contains one hole per copper site where the strong 'Hubbard' U leads to insulating behavior with a charge excitation gap of approximately 2 eV [39]. The $3d^9$ shell contains one hole. It therefore carries a net spin $S = 1/2$ which is mainly responsible for the magnetic properties of the parent compounds. The spins are localized on the Cu site and can be described by a quasi two-dimensional spin $S = 1/2$ Heisenberg model. According to the Hubbard model, the superexchange interaction induces anti-parallel spin arrangements in the neighboring electrons where by second order perturbation theory an energy gain is expected for the virtual hopping [210]. The Hamiltonian for the lattice model for interacting electrons has the following form

$$H = -t \sum_{(i,j),\sigma} c^{\dagger}_{i\sigma} c_{j\sigma} + U \sum_{i} n_{i\uparrow} n_{i\downarrow}. \tag{5.1}$$

The first term of Eq. 5.1 is the kinetic energy describing electrons hopping between nearest-neighbor sites i and j with the hopping amplitude t. $c^{\dagger}_{i\sigma}$ represents the creation of an electron on site i with spin σ. The term $n_{i\sigma} = c^{\dagger}_{i\sigma} c_{j\sigma}$ counts the number of electrons on site i. The second term denotes the interaction energy $U \gg t$ between the two electrons with opposite spins on the same site. Using this model, the superexchange interaction is $J = 4t^2/U$.

Figure 5.3 (a) shows the antiferromagnetically ordered spin arrangement and the strong hybridization between in-plane Cu ($3d_{x^2-y^2}$) and O ($2p_x$, $2p_y$) orbitals. In an antiferromagnetically ordered state, the magnetic moments of the copper spins interact via intermediate oxygen atoms with a relatively strong intralayer coupling. The in-plane nearest neighbor super-exchange J acts along the Cu-O-Cu bonds. In such systems, a large anisotropy is observed between the in-plane ($J_{\parallel} = 143$ meV)

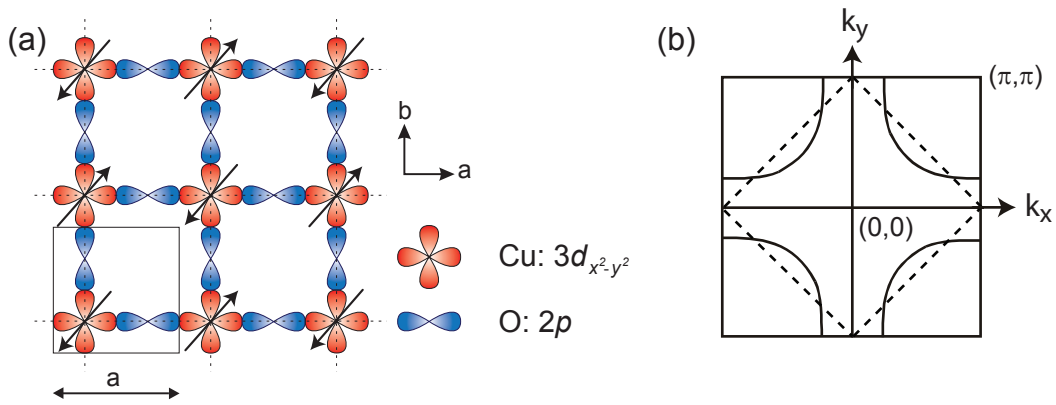

Figure 5.3: (a) An arrangement of antiferromagnetically ordered Cu spins (black arrows) in the relevant CuO_2 orbital structure of the cuprates. The unit cell is depicted with solid lines with the lattice constant a. (b) Fermi surface in the corresponding Brillouin zone. The magnetic superstructure yields the backfolded BZ (dashed lines).

[211] and out of plane ($J_\perp = 0.002\,\text{meV}$) exchange coupling which is as high as $J_\perp/J_\parallel \sim 10^{-5}$ [38, 39]. The weak interplanar coupling in LCO originates from the body-centered stacking of CuO_2 planes which completely cancels the magnetic coupling between the Cu^{2+} atoms in different planes. Due to the larger $J_\parallel$ value, long range order is developed differently in the LCO system in comparison to such as planar antiferromagnets. In LCO, the sensitivity of 3D long range order to $J_\perp$ is mainly responsible for the rapid reduction of the Néel temperature [212].

Figure 5.3 (b) shows the corresponding Fermi surface in the first Brillouin zone (solid lines) together with the magnetic Brillouin zone (dotted line). Due to the spin superexchange the magnetic Brillouin zone is rotated by 45° and only half the size of the original BZ. The particles located close to ($\pm\,\pi$, 0) and (0, $\pm\,\pi$) on the Fermi surface experience a strong effect of antiferromagnetic ordering resulting in strongly scattered particles. On the other hand, particles located close to ($\pi/2$, $\pi/2$) remain unaffected.

5.1.3 Light scattering by magnons

The spin dynamics of the cuprates is very well described by the properties of a two-dimensional (2D) Heisenberg antiferromagnet. The spin-interaction Hamiltonian can be expressed in the following form

$$H = -J \sum_{(i,j)} \boldsymbol{S}_i \cdot \boldsymbol{S}_j \tag{5.2}$$

where the sum (i, j) is restricted to the nearest neighbors in the square lattice and excludes double counting. $\boldsymbol{S}_i$ and $\boldsymbol{S}_j$ are the spin operators acting on the spins i and j belonging to the sublattice A ("up") and the sublattice B ("down") for the AF state, respectively. $\boldsymbol{S}_i \cdot \boldsymbol{S}_j$ is the interaction energy of two spins and J is the nearest-neighbor antiferromagnetic exchange constant. The condition $J>0$ favors anti-parallel orientation of two spins referring to the AF ground state.

The interaction Hamiltonian presented in Eq. 5.2 yields the AF ordered state. This state has Bloch-like excitations which are formally described by the magnon-creation and destruction operators [9]. The creation operators for $i(\downarrow)$ and $j(\uparrow)$ are $\alpha^{\dagger}_{\downarrow \boldsymbol{k}}$ and $\alpha^{\dagger}_{\uparrow \boldsymbol{k}}$, respectively. In a similar fashion, annihilation operators are defined as $\alpha_{\downarrow \boldsymbol{k}}$ and $\alpha_{\uparrow \boldsymbol{k}}$ for $i(\downarrow)$ and $j(\uparrow)$, respectively.

Since both of the spin operators ($\boldsymbol{S}_i$ and $\boldsymbol{S}_j$) participate in the magnon creation and annihilation processes, diagonalization in the magnon base is necessary which can be obtained via the Dyson-Maleev transformation [9, 14]. The relation between spin operators and magnon operators can be written in the form of the transformed Hamiltonian

$$H = \sum_{\boldsymbol{k}} \left[E_{\uparrow \boldsymbol{k}} \alpha^{\dagger}_{\uparrow \boldsymbol{k}} \alpha_{\uparrow \boldsymbol{k}} + E_{\downarrow \boldsymbol{k}} \alpha^{\dagger}_{\downarrow \boldsymbol{k}} \alpha_{\downarrow \boldsymbol{k}} \right]. \tag{5.3}$$

Here the sum over $\boldsymbol{k}$ extends to the AF Brillouin zone as shown in Fig. 5.3 (b). The expressions for the magnon energies are given by $E_{\uparrow \boldsymbol{k}} = E_{\boldsymbol{k}} - g\beta H_0$ and $E_{\downarrow \boldsymbol{k}} = E_{\boldsymbol{k}} + g\beta H_0$ with an external field H_0 and the coupling constant β. The detailed theoretical derivations are discussed in Ref. [9].

In the case of equivalent sub-lattices $(i = j)$, double degenerate eigenvalues are given by the following expression

$$E_{\boldsymbol{k}} = \hbar\omega_{\boldsymbol{k}} = 4JS[1 - \gamma^2_{\boldsymbol{k}}]^{1/2} \tag{5.4}$$

where γ_k depends on the position of the spin vectors and can be denoted as

$$\gamma_{\boldsymbol{k}} = \frac{1}{2}[\cos k_x a + \cos k_y a]. \tag{5.5}$$

For $S = 1/2$ systems, E_k is maximal at the boundaries of the magnetic BZ and reads

$$E_M = \hbar\omega_M = 2J. \tag{5.6}$$

The derived value in Eq. 5.6 can also be obtained via a simple flipping of one Cu

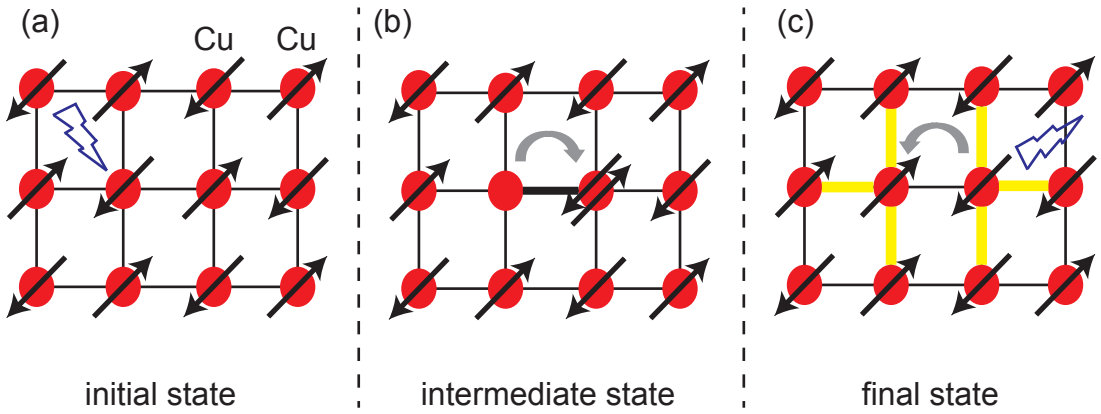

Figure 5.4: Pictorial illustration of nearest-neighbor spin-flip process in CuO_2 planes showing copper (red balls) spins (black arrows) arrangements. (a) In the initial state, the incoming photon is absorbed by the electron which results in the hopping of an electron leaving behind a hole. (b) The electron creates a virtual double occupancy in the intermediate state. (c) In the final state, an electron with opposite spin hops back to the hole site breaking six exchange bonds with an energy cost of $3J$.

spin with respect to four neighboring Cu spins. The resulting coupling constant value J can be derived as

$$E_M = \hbar\omega_M = 4 \times \frac{1}{2} \times J = 2J. \tag{5.7}$$

The excitation of a single magnon is not easy to observe due to a smaller momentum transfer in a Raman process. According to Eq. 5.5, in cuprates with one CuO_2 plane per unit cell, the magnon frequency $\omega_{\boldsymbol{k}}$ tends to zero for $k \to 0$. On the contrary, cuprates with two CuO_2 planes per unit cell generate acoustic and optical-like magnons. For example, in the case of $YBa_2Cu_3O_{6.3}$, optical magnons have been observed near $k = 0$ at 524 cm^{-1} via inelastic neutron scattering [213]. For undoped cuprates, a prominent signature of the B_{1g} symmetry is a broad peak which is attributed to the inelastic scattering from two-magnon excitations. Using Eq. 5.6 and 5.7, one can calculate the corresponding peak frequency for a two-magnon excitation to be equal to $4J$. However, since scattering is localized to nearest-neighboring spins, magnon-magnon interactions must be included [214]. In this case, the peak shifts to $3J$ by breaking six exchange bonds between the local neighbors.

In Fig. 5.4 the photon-magnon scattering involving the two-magnon process is depicted. The initial state is a 2D Heisenberg antiferromagnet. An incident polarized photon causes an electron with spin-down to hop to the neighboring site leaving behind a hole. It creates a double occupancy in the intermediate state as shown

in Fig. 5.4 (b). In this state, one electron of the double occupancy site with up-spin returns to the formerly down site in order to liberate an outgoing photon with certain energy. This hopping mechanism is responsible for a localized disturbance in the antiferromagnetically ordered state. In the final state, each of the two flipped spins breaks three neighboring copper bonds, leading to a total exchange energy of $\frac{1}{2}J \times 6 = 3J$.

The Fleury-Loudon Hamiltonian [9] provides a direct relation of light interaction with spin degrees of freedom as

$$H = J \sum_{i,j} (\hat{\mathbf{e}}_i \cdot R_{ij})(\hat{\mathbf{e}}_s \cdot R_{ij}) \boldsymbol{S}_i \cdot \boldsymbol{S}_j. \tag{5.8}$$

Here $\hat{\mathbf{e}}_\mathrm{i}$ and $\hat{\mathbf{e}}_\mathrm{s}$ are the polarization vectors for the incoming and scattered photons, respectively. J is a coupling constant. R_{ij} is a vector along the bond connecting two nearest-neighbors sites i and j. The formalism presented in Eq. 5.8 is mainly valid for the non-resonant conditions where the incident light energy does not match an optically allowed interband transition energy. The theoretical developments of the Fleury-Loudon model for the non-resonant regimes were addressed based on various analyses such as higher order spin-wave theory [14], series expansion [212], finite temperature Monte-Carlo methods [214], studies of bilayer effect [51], and ring exchange [215]. However, most of the experimental work on AF parent cuprates has been carried out in the resonant regime where the frequencies of the incoming and/or scattered photons are comparable to the charge transfer energy gap of these insulating materials. For example, the $B_{1\mathrm{g}}$ channel of two-magnon scattering in insulating parent compounds has a resonance for incident photons at energies close to 3 eV [6]. Considering the fact, further theoretical developments have been made by re-examining the Fleury-Loudon model for the resonant regime based on a spin density wave approach, the so-called triple resonance [15, 50] and using both spin and charge degrees of freedom [216]. Most of the properties of the two-magnon Raman response in $B_{1\mathrm{g}}$ symmetry have been described in terms of spin-wave theory. Despite of several attempts, the line shape could not be reproduced so far. The role of other important factors such as multi-magnon processes, cyclic spin excitations and amplitude fluctuations are not fully understood yet [45].

Recently, an alternative approach based on field theory has been introduced to describe the line shape of the two-magnon Raman spectra in $B_{1\mathrm{g}}$ symmetry. Earlier, field-theoretic approaches have been already applied to explain the results from neutron-scattering experiments [217]. The key benefit of the field theory approach

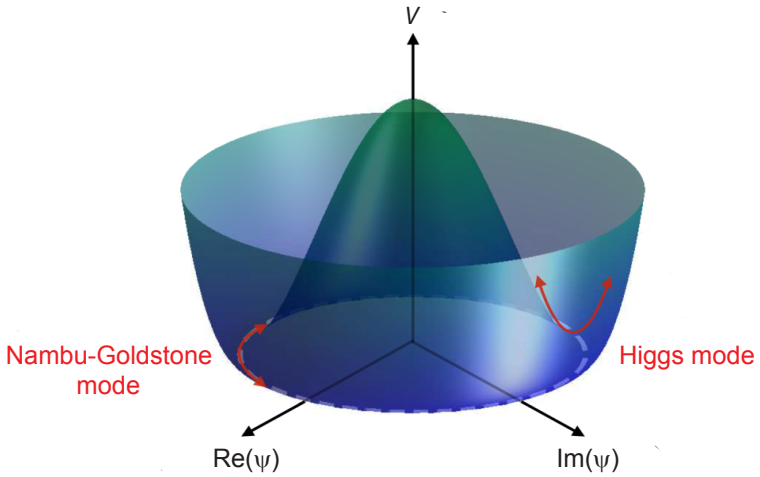

Figure 5.5: Energy density V as a function of the order parameter. Illustration of the Nambu-Goldstone and Higgs modes arising from phase and amplitude modulations, respectively. Adopted from [49].

is the possibility to separate important universal features of materials from their microscopic details. This offers a well-defined starting point for perturbation theory. In order to describe the Raman response, the field-theoretical calculations consider perturbation theory up to infinite order together with inclusion of amplitude (Higgs) fluctuations of the order parameter.

Higgs fluctuations play a crucial role in a variety of interacting systems including the standard model [46, 218] in high-energy physics [219], Bose condensates [220], super-fluidity and -conductivity [221–223] and magnetism [224]. The Higgs mode is observed as the amplitude oscillations of a quantum field in many-body systems. These oscillations appear as collective excitations due to spontaneous breaking of a continuous symmetry. In any physical system, the order parameter and its variations in space and time are given by the complex function $\Psi(\mathbf{r};\mathrm{t})$. It includes an amplitude and a phase near the phase transition between an ordered ($|\Psi|>0$) and a disordered phase ($|\Psi|=0$). Within the ordered phase, the energy potential has a Mexican hat like shape as shown in Fig. 5.5. In the minimum of the energy potential, the order parameter has a non-zero value. When the field around the ground state is expanded, two types of excitations emerge: massless Nambu-Goldstone modes related to the phase variation of Ψ and the Higgs mode associated to the amplitude mode of Ψ.

The Nambu-Goldstone modes are the gap-less phase oscillations along the circumferential direction at the bottom of the potential. The amplitude mode corresponds to the oscillations in the radial direction having a finite energy. The amplitude mode is decoupled from the phase mode. The amplitude modes, be-

ing chargeless and spinless do not couple directly to the external probe making their experimental observation difficult. There are a few experimental evidences for the observation of the amplitude mode. The observation of a Higgs mode in the antiferromagnetically ordered phase of $TlCuCl_3$ at high pressure via neutron scattering was reported in 2008 [224]. Recently, free oscillations of the Higgs mode of the superconducting order parameter were observed in s-wave superconductors $Nb_{1-x}Ti_xN$ using nonlinear terahertz (THz) spectroscopy [225]. In the case of 2D quantum antiferromagnets, direct observation of the amplitude mode is possible via Raman scattering because of the fact that the response functions couple to the square of the order parameter [46].

Weidinger and Zwerger [47] performed a detailed calculation of the response and expressed the transition rate ($\mathcal{R}$) of Raman scattering in terms of correlation functions of spin operators. The Raman spectrum of undoped cuprates is determined by incorporating two parameters: the exchange coupling constant J and a dimensionless Higgs mass m_0. Within the Néel ordered state, the Raman response of the AF ordered cuprates is described by the combined contributions from the two-magnon and the two-Higgs modes. Experimentally, the contribution of the amplitude mode has not been observed as a separate peak so far. In spite of that, the amplitude mode seems to play a role in explaining the shape of the Raman spectra of undoped cuprates. In field-theoretical calculations, the Raman susceptibility is expressed as the sum of the individual contributions from scattering processes involving pure magnons and Higgs modes. An expression for the Raman susceptibility is given by

$$\chi''_{\mathrm{Raman}} = \chi''_{\mathrm{M}} + \chi''_{\mathrm{H}}. \tag{5.9}$$

Here χ''_{M} and χ''_{H} are the two-magnon and two-Higgs susceptibilities, respectively. The two-magnon response to the leading order in the coupling g has been calculated using the correlation function

$$\chi''_{\mathrm{M}} = \frac{g^2 B^2 \hbar^3 S^4}{12 c_s} \omega^3 \theta(2c_s\Lambda - \omega) + O(g^3) \tag{5.10}$$

where g is the dimensionless coupling constant, B is equal to $\sim t^2/(U - \hbar\omega_i)$. S and c_s are the spin operator and the spin wave velocity, respectively. Λ is the momentum cutoff. $O(g^3)$ involves the square gradient of the magnon field. Assuming only the case of nearest-neighbor coupling J, the above equation corresponds to

$$2c_s\Lambda = 2\pi\hbar J \tag{5.11}$$

Similarly, contributions from longitudinal fluctuations of the order parameters are derived using the correlation function of the two-Higgs operator,

$$\chi''_{\mathrm{H}} = \frac{g^2 B^2 \hbar^3 S^4}{12 c_s \omega} \left[\left(\frac{\omega}{2}\right)^2 - c_s^2 m_0^2 \right]^2 \theta\Big(\omega - 2c_s m_0) \times \theta(2c_s \sqrt{\Lambda^2 + m_0^2} - \omega\Big) + O(g^3) \quad (5.12)$$

where $\tilde{m}_0$ is the Higgs mass. The overall Raman response depends sensitively on the precise values of the Higgs mass. For an $S = 1/2$ system, the Raman spectra for three different values of the Higgs mass are thoroughly studied in Ref. [47]. In the cases of a light ($\tilde{m}_0 = 0.25$) and a heavy mass ($\tilde{m}_0 = 0.9$), the Raman spectra are found to be dominated by the two-magnon response. They do not show any distinct feature due to a Higgs mass contribution. However, for an intermediate mass ($\tilde{m}_0 = 0.65$), a sharp shoulder appears above the two-magnon maximum as an onset of the Higgs mode. The variation in the value of Higgs mass has also allowed the observation of the influence of the Higgs mass on the two-magnon response.

The above field-theoretical formalism is used to reproduce the line shape of the strongest scattering B_{1g} symmetry for two undoped compounds: La_2CuO_4 (LCO) and $YBa_2Cu_3O_{6.05}$ (Y123). We intend to utilize these calculations to quantitatively assess our measurements by facilitating the precise extraction of the Heisenberg coupling J. Apart from it, we study an important role of amplitude fluctuations [2, 226].

5.2 Experimental details

This section is intended to be a brief compilation of the relevant scattering processes and experimental details. First, electronic Raman scattering is described in general including polarization configurations to elucidate different symmetry channels. Furthermore, the investigated samples and the experimental setup are explained in brief.

5.2.1 Electronic Raman scattering

Raman scattering is an invaluable spectroscopic tool which allows one to investigate the dynamics of strongly correlated electrons. When an incident light is coupled to the electronic charges in solid material, it induces variations in the electronic charge density leading to the inelastic scattering from various types of excitations.

With this technique, the response of a system to an external perturbation (photons) is obtained by measuring the total cross section for scattered electrons from the illuminated area of the sample. The differential cross section is directly proportional to the measured rate of photons $\dot{N}(\omega, T)$. The differential cross section is determined by the probability for an incident photon with frequency ω_{i} to scatter into the solid angle interval between Ω and $d\Omega$ and a frequency window between ω_{s} and $d\omega_{\mathrm{s}}$ per second. An expression for the differential cross section is given by [6]

$$\dot{N}(\omega, T) \propto \frac{\partial^2 \sigma}{\partial\Omega\, \partial\omega_s} = \hbar r_0^2 \frac{\omega_s}{\omega_i} \mathcal{R}, \tag{5.13}$$

where r_0 is the Thomson radius of an electron and is written as $r_0 = e^2/mc^2$. The notations e, m, and c are the elementary charge of the electron, the electron mass, and the speed of light, respectively. The transition rate of the scattering process is denoted by $\mathcal{R}$ which is the main element to obtain the scattering cross section. It is determined via Fermi's golden rule and can be expressed as follows:

$$\mathcal{R} = \frac{1}{\mathcal{Z}} \sum_{I,F} \exp[-\beta E_I] \left| M_{F,I} \right|^2 \delta(E_F - E_I - \hbar\Omega), \tag{5.14}$$

where $\mathcal{Z}$ is the partition function, $\beta = 1/k_{\mathrm{B}}T$, and $M_{F,I} = \langle F| \, M \, |I\rangle$ is the transition matrix element. The effective light-scattering operator M describes the electron-photon interaction. $\Omega = \omega_i - \omega_s$ is the transferred frequency referred as the Raman shift. An in-depth introduction to the subject is available in the review article by Devereaux and Hackl [6]. Several other authors have also elaborated the theoretical treatments of electronic Raman scattering with the key focus on semiconductor [227] and superconductors with applications towards cuprates [228, 229].

5.2.2 Polarization configurations

The polarization configurations are very important to understand the response from excitations having different symmetries. For the material class of the cuprates, polarization vectors x and y are oriented along the direction of the Cu-O bonds. The commonly used polarization configurations include linear combinations of xx and xy, the primed linear combinations of $x'x'$ and $x'y'$, and the circular combinations of RR and RL. Here $x' = 1/\sqrt{2}(\hat{x} + \hat{y})$ and $y' = 1/\sqrt{2}(\hat{x} - \hat{y})$ are rotated by 45° with respect to the x and y polarizations, respectively. $R, L = 1/\sqrt{2}(\hat{x} \pm i\hat{y})$ defines the right and left circular polarizations. Each set of polarizations allows to access the sum of two symmetries. The projected sets of symmetries with respect to the polarization

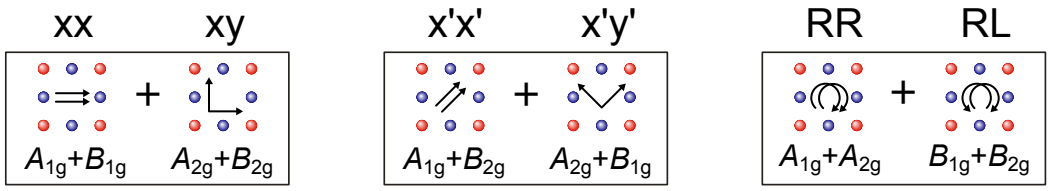

Figure 5.6: Illustration of six different polarization configurations. The black arrows indicate the polarization vectors of the incident and scattered light for each CuO_2 plane. Each polarization configuration results as the sum of two symmetry components. The red and blue solid circles denote copper and oxygen atoms, respectively.

combinations are illustrated in Fig. 5.6. In this figure, six CuO_2 plaquettes are shown where each plaquette shows one polarization combination using the arrows in the center. For example, the xy polarization configuration where x belongs to the incoming polarization ($\mathbf{e}_\mathrm{i}$) and y defines the scattered polarization ($\mathbf{e}_\mathrm{s}$).

$$\begin{aligned} I_{\mathrm{A1g}} &= (1/3)[(xx + x'x' + RR) - (1/2)\,(xy + x'y' + RL)], \\ I_{\mathrm{A2g}} &= (1/3)[(xy + x'y' + RR) - (1/2)\,(xx + x'x' + RL)], \\ I_{\mathrm{B1g}} &= (1/3)[(xx + x'y' + RL) - (1/2)\,(xy + x'x' + RR)], \\ I_{\mathrm{B2g}} &= (1/3)[(xy + x'x' + RL) - (1/2)\,(xx + x'y' + RR)]. \end{aligned} \tag{5.15}$$

From Fig. 5.6, one can observe that pure symmetries cannot be accessed by a single set of polarization configuration. To gain insight from an individual symmetry one has to measure at least four polarization configurations with an inclusion of the circular polarization. The linear combinations presented in Eq. 5.15 can be utilized to extract the single symmetry.

5.2.3 Samples

In this work, three different cuprate systems, LCO, Y123, and Bi2212:Y have been studied using Raman scattering. One of the necessary conditions to probe intrinsic features via Raman scattering is the availability of high quality, single crystalline samples with a minimal size of approximately $1 \times 1\,\mathrm{mm}^2$. Prior to the experiments, information about the quality of the sample is important to interpret the spectroscopic behavior correctly. In order to fabricate high quality samples, several different synthesis routes have been utilized in combination with the post-annealing treatments.

LCO was synthesized in an image furnace by the traveling-solvent floating zone

(TSFZ) method. The as-grown crystals of LCO had a Néel temperature (T_N) of 270 K. The as-grown crystals were further annealed in Ar atmosphere at 920 °C for 50 hours. Afterwards, the crystals were cooled down to 500 °C in 50 hours and were brought to ambient temperature in another 50 hours. After the annealing, T_N was as high as 325 K [2] which has not been exceeded as of now [39]. The cleaving of these materials is very difficult, thus all of the Raman measurements were performed on a polished sample. The Y123 sample was prepared in $BaZrO_3$ crucibles [230] which is the best technique to obtain samples with high purity [231]. In order to fabricate the best crystal quality and the lowest possible oxygen content (approx. 6.05), as-grown material was annealed in Ar atmosphere at 900 °C and then slowly cooled down to room temperature. Bi2212:Y was grown by a flux method in ZrO_2 crucibles [232].

For the Raman measurements, as-grown annealed sample of Y123 was used whereas the Bi2212:Y sample with freshly cleaved surface was utilized. In the case of LCO, a sample of an approximate size of $2 \times 2\,\mathrm{mm}^2$ was prepared by polishing the surface in the crystal laboratory of the Technical University of Munich (TUM) using a diamond paste with a grain size down to 0.3 µm. In order to make sure that the polishing does not influence the intrinsic properties of the sample, we performed test measurements with the cleaved LCO sample. The results obtained from the cleaved and the polished surfaces are compared in the subsequent section.

5.2.4 Surface treatment

Raman scattering is sensitive to the roughness of the sample surface. In order to reduce contributions from elastically scattered stray light mirror-like surfaces are required. For LCO, the desired surface quality can be obtained by either polishing or cleaving the sample surface. For quantitative measurements, samples with a sufficiently large area are required which can only be obtained by polishing. However, polishing of the surface leads to damage in the range of the penetration depth influencing the spectral characteristics. On the other hand, cleaved surfaces provide usually reliable results. Since LCO does not have a cleavage plane only small flat areas can be obtained which are too small for quantitative measurements. We compared the B_{1g} spectra in order to be sure that polishing worked in the case of LCO.

The spectral comparison between polished and cleaved LCO samples in $x'y'$ (A_{2g}+B_{1g}) configuration is shown in Fig. 5.7. These spectra were measured at room temperature (310 K) with an excitation wavelength of 458 nm in the energy range between 50 and 6000 cm^{-1}. We observe small differences between the spectra of the

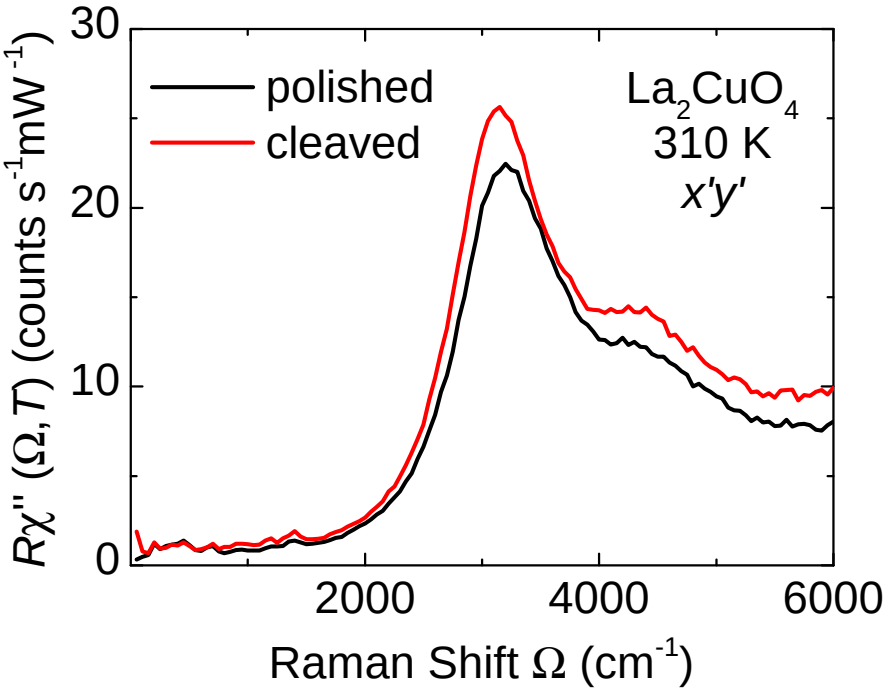

Figure 5.7: Effect of the surface treatment in LCO. The spectra are measured with $x'y'$ polarization at 310 K. A small intensity difference is observed between the spectra of the polished (black) and the cleaved (red) surfaces.

polished and cleaved LCO. In contrast to the polished sample, the intensity profile of the spectrum of the cleaved surface is slightly higher. The positions of the prominent characteristic features at 3300 and 4600 cm^{-1} as well as the relative spectral weights are identical in both spectra. There are statistically significant differences which can at least partially be traced back to the surface. Otherwise the prominent features can be considered equal.

5.2.5 Experimental setup

The Raman experiments were performed with a calibrated setup. The schematic sketch of the experimental configuration is illustrated in Fig. 5.8. The excitation laser module comprises an Ar^+ laser (Coherent Innova 304C) with discrete laser lines in the range 458 nm $\leq \lambda_{\mathrm{exc}} \leq$ 528 nm and a diode-pumped solid state laser (DPSS-Coherent Genesis MX SLM 577-500) emitting at 575 nm. Depending on the measurements, the appropriate laser can be selected using mirror M1. Initially, the optical system is configured according to the beam diameter of the ion laser ($\varnothing = 1.6$ mm). In order to use the same optical system for the solid-state laser, having a smaller beam diameter ($\varnothing = 0.8$ mm), the beam has to be expanded. For this

purpose, a beam expansion unit [assembly of two achromatic lenses L1 ($f_1 = 30\,\mathrm{mm}$) and L2 ($f_2 = 60\,\mathrm{mm}$)] is installed directly after the DPSS laser.

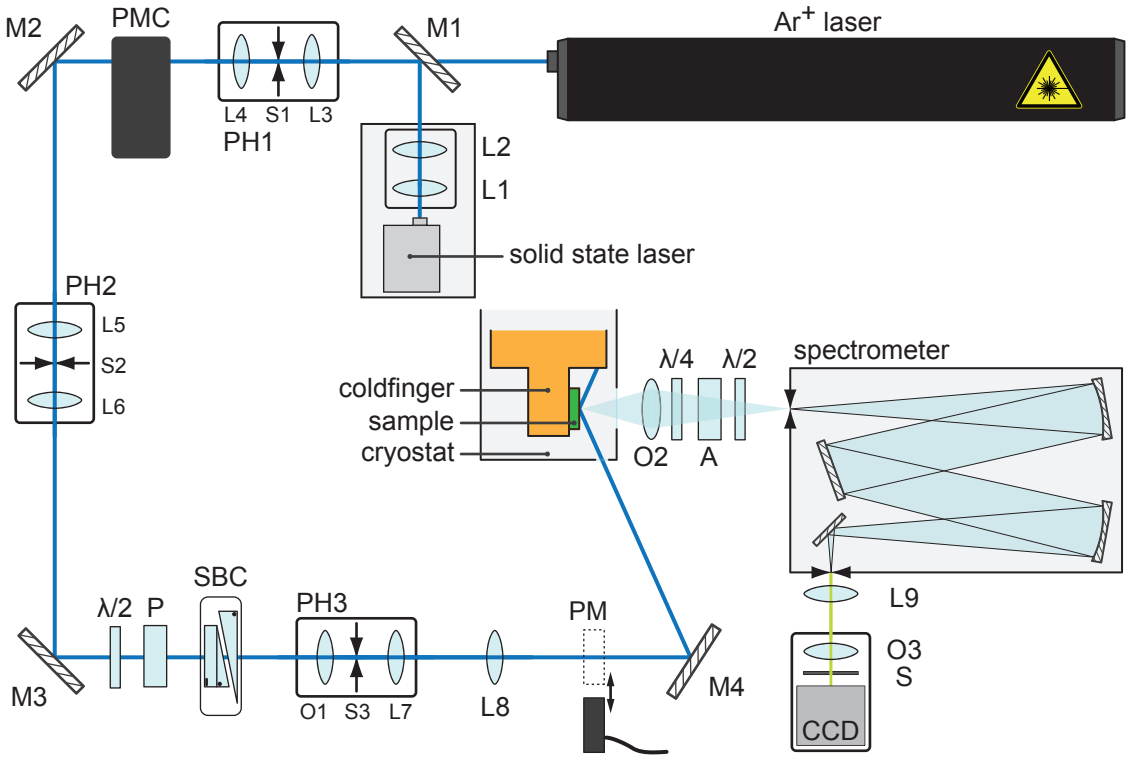

Figure 5.8: Schematic layout of the light path for Raman experiments consisting of several novel optical components. Each optical configuration is discussed in detail in the text. Adopted from [200].

The spatial filter system (PH1), a combination of two achromatic lenses (L3 and L4) and a circular aperture S1 ($\varnothing = 30\,\mu\mathrm{m}$), is used for filtering divergent components of the laser beam. The prism monochromator (PMC) filters out the plasma lines by dispersing the laser light onto slit S2. Plasma lines with wavelengths different by more than $25\,\mathrm{cm}^{-1}$ from that of the selected laser line are blocked. The monochromatic laser light is directed towards the second spatial filter system (PH2) via mirror M2. The second spatial filter system consists of two achromatic lenses (L5 and L6) and an adjustable slit (S2). This configuration is the exit slit of the PMC. Finally, the laser beam is directed towards the half-wave plate ($\lambda/2$) via mirror M3. The half-wave plate modulates the laser power. The desired polarization state of the incident laser beam is set by the combined configuration of a Glan-Thompson polarizer (P) and a Soleil-Babinet compensator (SBC) offering control over the polarization and phase of the light. The last spatial filter (PH3) after the compensator is used to prepare a Gaussian beam. It configures with an objective lens (O1), an

achromatic lens (L7), and a circular aperture (S3) with 10 µm diameter. This system finally determines the quality of the beam which is focused on the sample via an achromatic lens L8. The laser beam is directed onto the sample via mirror M4.

Before the scattered light is directed into the spectrometer, it is essential to select the polarization of scattered photons. To this end a quarter wave-plate ($\lambda/4$) and an analyzer (A) are used. The half-wave retardation plate ($\lambda/2$) next to the analyzer facilitates the rotation of the selected linear polarization along the x-axis of the laboratory system, which is also the preferred direction of maximal transmission in the spectrometer. The wavelength of the scattered photons is selected by a double monochromator (Jarell-Ash 25-100). The window of the selected wavelength can be set manually. The CCD camera (Princeton Instruments, PyLoN:100BR eXcelon) counts the photons which acts as a single channel detector allowing one to acquire the spectra point by point. The two- and three-dimensional layouts of the spectrometer are depicted in Fig. 5.9.

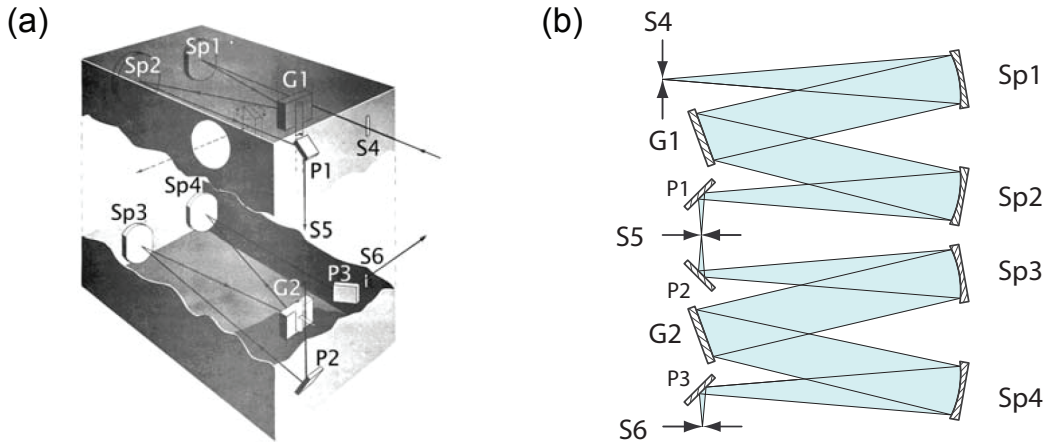

Figure 5.9: Ray diagrams of double monochromator based spectrometer incorporated for the Raman measurements. Illustration in (a) 3D and (b) 2D view. It accommodates two symmetrically-coupled monochromatic stages where each stage is composed of two spherical mirrors and one grating.

The samples are mounted on the cold finger of a cryogenically pumped ^{4}He flow cryostat. The cryostat operates at a vacuum level of better than 10^{-6} mbar with an accessible temperature range of $1.8\,\mathrm{K} \leq T \leq 340\,\mathrm{K}$. The well-defined orientation of the sample with respect to the laboratory system is crucial (see subsection 5.2.2). Therefore, the orientation of the crystallographic axes a and b is determined via a standard Laue diffraction experiment.

5.3 Experimental results

This section summarizes the results of the inelastic scattering light experiments on undoped compounds of three different cuprate families.

5.3.1 Symmetry analysis of La_2CuO_4

The intensity of the Raman spectra presented in this section is given in absolute units (counts s^{-1} mW^{-1}) unless stated otherwise. All spectra are corrected for the sensitivity of the instrument and divided by the Bose-Einstein thermal factor $\{1 + n(\Omega, T)\}$. The data are multiplied by the factor ω_i/ω_s (see Eq. 5.13) leading to the final spectral data for the Raman response function $R\chi''(\Omega, T)$.

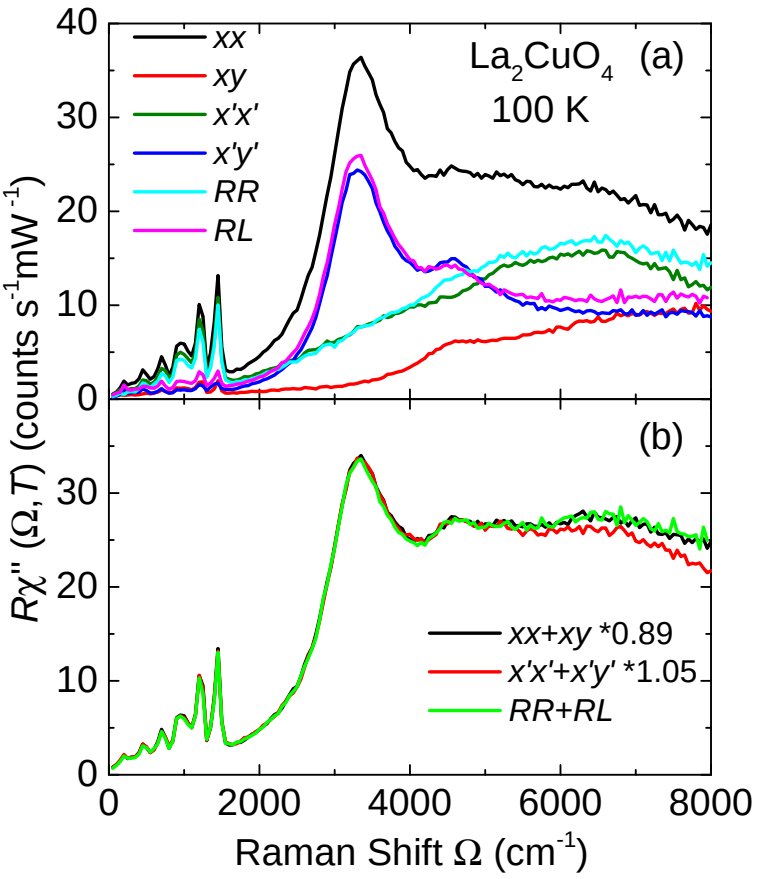

Figure 5.10: Raman response of La_2CuO_4 at 100 K. (a) A set of six different polarization configurations where each spectrum comprises two symmetries. (b) Each sum of two spectra projecting all four in-plane symmetries.

We first describe the results of the Raman response for La_2CuO_4. The measurements were carried out on a polished sample [2] at a temperature of 100 K with an

excitation wavelength of 458 nm. Figure 5.10 (a) shows a compilation of the raw data of LCO measured with six different polarization configurations xx, xy, $x'x'$, $x'y'$, RR, and RL. The major part of the energy range up to 2000 cm^{-1} is dominated by phononic excitations. A contribution from phonons is observed especially in xx, $x'x'$, and RR configurations. Since phonons are not of interest here, we measure the Raman spectra with lower resolution. A pronounced and broad peak at about 3300 cm^{-1} (409.4 meV) is observed in three polarization configurations of xx, $x'y'$, and RL. Another prominent mode adjacent to this peak is present at 4600 cm^{-1} which is present in four different configurations of xx, xy, $x'y'$, and RL originating from either A_{2g} or B_{1g} symmetry. The spectra in $x'x'$ and RR are featureless between 2000 and 4000 cm^{-1} and then begin to pile up in the energy range between 4000 and 8000 cm^{-1}.

Each of the measured polarization combinations in Fig. 5.10 (a) involves the sum of two symmetries. As pointed out before the over-determination of the spectra can be used to check the consistency of the experiments. Figure 5.10 (b) demonstrates the quantitative check of consistency in the form of three different sum spectra. The xx+xy and $x'x'$+$x'y'$ spectra are multiplied by the factors 0.89 and 1.05 respectively, to match the intensities with those of the $RR + RL$ configuration. We find that the three spectral sets agree well within the statistical error up to 5000 cm^{-1}. These small corrections result from the experimental errors such as insufficient adjustment of the absorbed laser power on the sample and/or improper settings of incoming and outgoing photon polarizations. The energy range above 5000 cm^{-1} shows a deviation between the spectra on the order of 10% or less. These deviations are observed mainly in the sum spectra of $x'x'$ and $x'y'$ (red spectrum). Luminescence may play a role in this case and cannot easily be controlled. Apart from it, surface layer accumulation could also be responsible for the difference between the spectra.

Now we determine the symmetry projections. In Fig. 5.11, we plot the Raman response of LCO for all four symmetries in the wide energy range from 50 to 8000 cm^{-1}.

At low energies up to 2000 cm^{-1}, we observe the contribution of the phonons in A_{1g}, B_{1g}, and B_{2g} symmetries. In the A_{1g} channel, there are two broad features between 3000 and 4000 cm^{-1} and between 5000 and 7000 cm^{-1}. The latter one consists of two sub-features and is stronger than the first one. In the A_{2g} channel, the intensity up to 3000 cm^{-1} is negligible. However, it becomes comparable with the intensity of the spectra in other symmetries at higher energies. As a remarkable observation, a well-resolved peak at 4600 cm^{-1} is present in A_{2g} symmetry. In

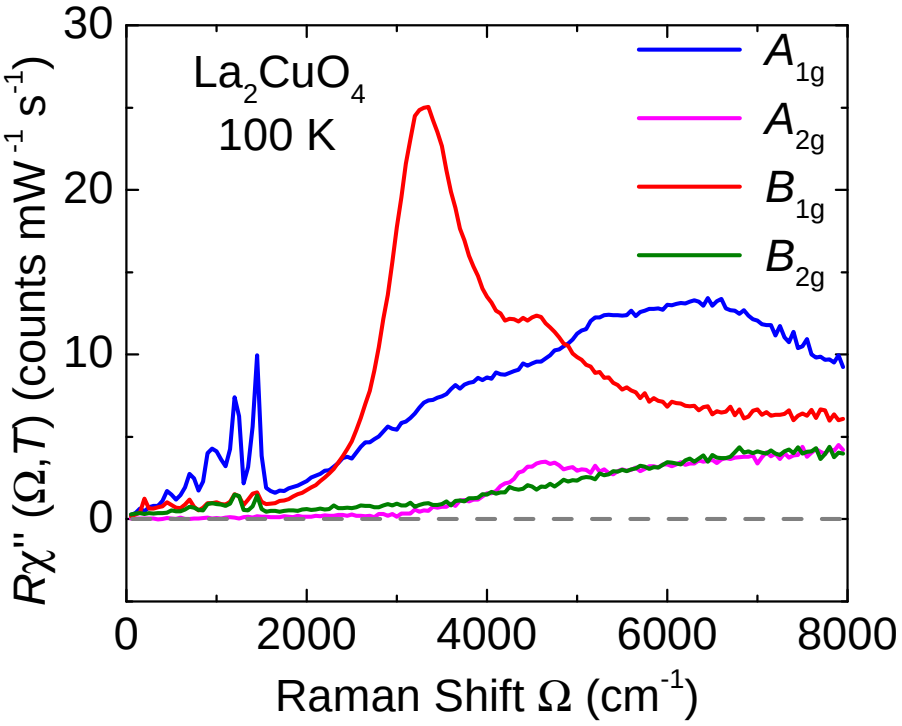

Figure 5.11: Raman spectra of four pure symmetries (A_{1g}, A_{2g}, B_{1g}, and B_{2g}) observed in the ab-plane of La_2CuO_4 in the AF state at 100 K.

the B_{1g} channel, the spectrum has the highest intensity in the range from 2000 to 4000 cm^{-1}. The maximum of the most prominent peak is found to be at approximately 3300 cm^{-1}. Above the maximum, the intensity of the peak decays slowly making the peak rather asymmetric. Above 4000 cm^{-1}, a secondary maximum is observed at about 4600 cm^{-1} which resembles closely to the feature observed at the same energy in the A_{2g} channel. Above the secondary peak, the spectral intensity decreases towards 8000 cm^{-1}. The B_{2g} spectrum has weak phonon contributions, and the rest of the spectrum is completely featureless.

In order to get a better insight into the identification of the various features, we compare the symmetry-resolved spectra of three cuprate families, LCO, Y123, and Bi2212:Y as displayed in Fig. 5.12. The Raman spectra of Y123 and Bi2212:Y samples were measured at 200 K.

In all three samples, the B_{1g} spectra have the highest intensity in the range of 2000 to 4000 cm^{-1}. A broad and distinct peak can be observed in this range which essentially probes the simultaneous spin-flip on two neighboring Cu atoms [4, 9]. The peak maxima of Y123, Bi2212:Y, and LCO are observed at 2750, 2900, and 3300 cm^{-1}, respectively. Below the maximum a strong energy-dependent behavior

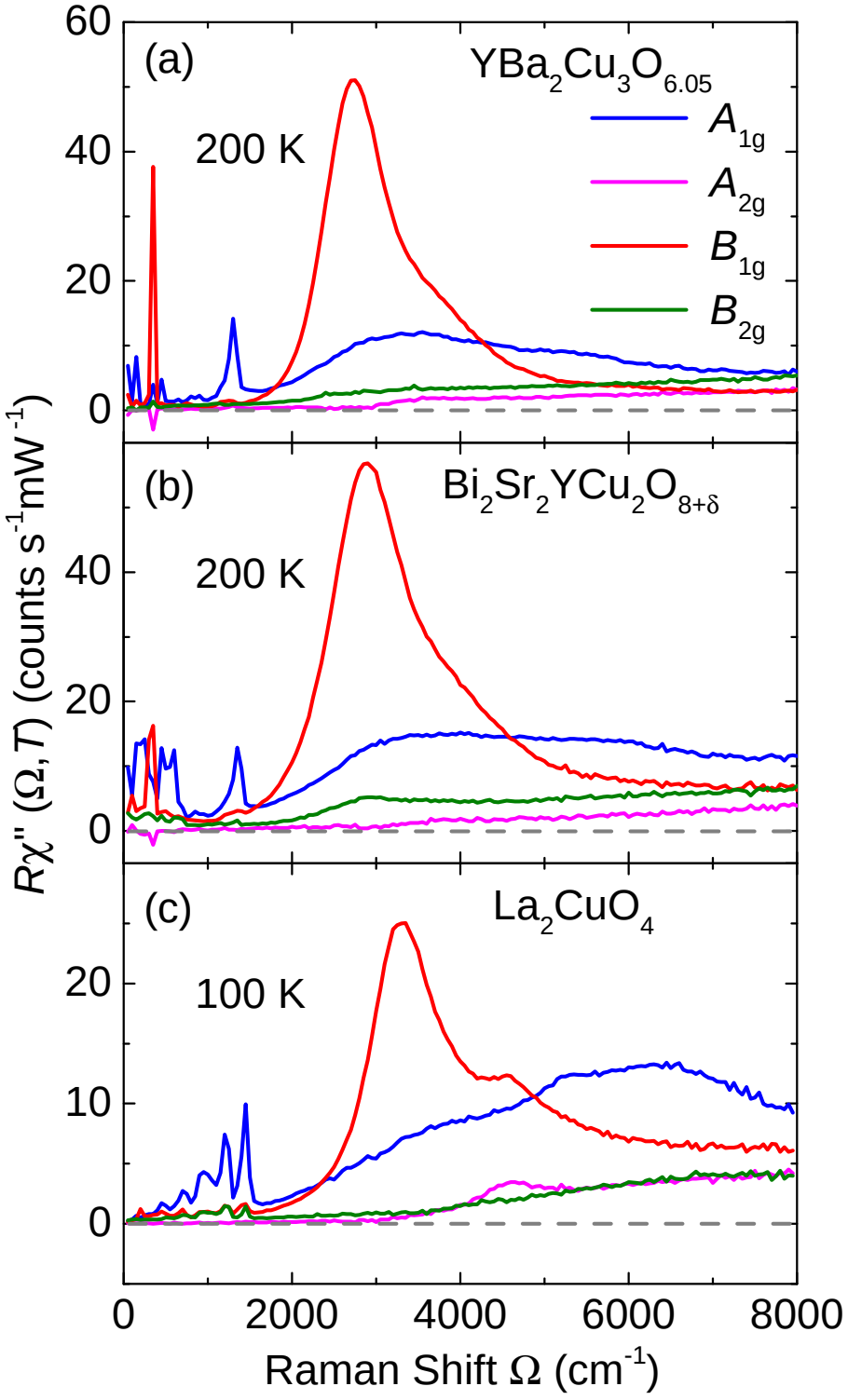

Figure 5.12: Symmetry-resolved Raman response of three different cuprate families. (a) Bi-layer $YBa_2Cu_3O_{6.05}$ (Y123) at 200K. (b) Bi-layer $Bi_2Sr_2YCu_2O_{8+\delta}$ (B12212:Y) at 200K. (c) Single layer La_2CuO_4 (LCO) measured at 100K.

could be observed. For low energies, the Ω^3 power law could not directly be observed as predicted theoretically [46, 47]. This deviation can partially be traced back to the contributions from phonons and particle-hole excitations which cannot reliably be subtracted. Above the maximum the intensity decreases slowly which makes the peak asymmetric. Except for the low energy regime, the B_{1g} spectra of Y123 and Bi2212:Y are similar. In contrast, the B_{1g} spectrum of LCO shows significant differences in the form of a well-defined secondary maximum at 4600 cm^{-1} followed by an increase of intensity in the higher energy region above the secondary peak.

The A_{1g} spectra in all three samples show dominant phonon contributions at low energy. In all materials, there is a broad maximum between 3000 and 5000 cm^{-1} which does not correspond to the position and shape of the B_{1g} peak. In addition, the LCO spectrum exhibits a shoulder between 5000 and 7000 cm^{-1} composed of two sub-features. In Y123 and Bi2212:Y, we find a weaker shoulder in this energy range. In the case of A_{2g} symmetry, the intensity vanishes to within the experimental resolution for energies up to the B_{1g} maximum. The onset above this energy is well defined and nearly abrupt. In the LCO sample, a well-resolved peak is found at 4600 cm^{-1}, appearing at energies similar to the secondary maximum observed in the B_{1g} spectrum. The spectra in B_{2g} symmetry are featureless for all three compounds except for a small peak present in the Bi2212:Y sample. This peak is located exactly at the position of the two-magnon peak observed in the B_{1g} channel. Here, polarization leakage could be responsible.

The B_{1g} Raman spectra reveal double spin-flip excitation. Since the high-energy parts of the B_{1g} spectra are not universal neither close to the maximum nor at higher energies, it becomes necessary to explore the possible origin of these differences. To this end, we studied the resonance behavior using different excitation wavelengths. In resonance condition, the overall intensity varies whereas the shapes may or may not change. The resonance studies of three undoped samples have been carried out with blue (458 nm) and green (514 nm, 528 nm) laser lines. The Raman response for three samples in $x'y'$ configuration as a function of excitation energy is illustrated in Fig. 5.13.

Figure 5.13 (a)-(c) displays the raw data. The spectra with $\lambda_{\mathrm{exc}} = 458\,\mathrm{nm}$ were measured up to 8000 cm^{-1}. The spectra taken with the laser wavelength $\lambda_{\mathrm{exc}} = 514\,\mathrm{nm}$ were measured up to 5600 cm^{-1} due to the limited range of the spectrometer. The scattering cross sections for Y123 [Fig. 5.13 (a)] and Bi2212:Y [Fig. 5.13 (b)] are significantly larger for $\lambda_{\mathrm{exc}} = 458\,\mathrm{nm}$. In contrast, the LCO spectrum [Fig. 5.13 (c)] with $\lambda_{\mathrm{exc}} = 514\,\mathrm{nm}$ lies above the one with $\lambda_{\mathrm{exc}} = 458\,\mathrm{nm}$. In LCO the phonons res-

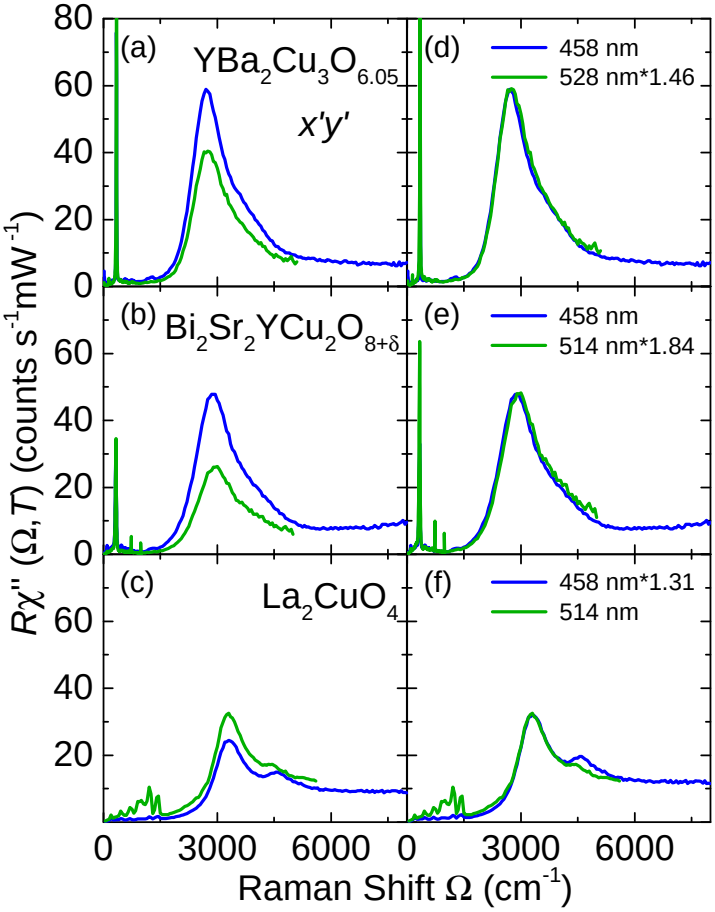

Figure 5.13: Excitation energy dependent Raman response of three undoped cuprates. (a)-(c) Raw data for Y123, Bi2212:Y, and LCO, respectively in $x'y'$ polarization geometry. (d)-(e) Multiplied spectra to scale the intensities of blue and green excitation energies. The appropriate multiplicative factors are as indicated.

onate strongly up to 1500 cm^{-1}. The panels in Fig. 5.13 (d)-(f) present the spectra multiplied by the appropriate constants to match the peak intensities. The spectra of Y123 and Bi2212:Y measured with the green excitation lines (514 nm and 528 nm) are multiplied by the factors 1.46 and 1.84, respectively. In the case of LCO, the blue spectrum is multiplied by 1.31. We find that the line shapes are identical to within the experimental accuracy for a wide energy range in all three samples. In contrast to Y123 and Bi2212:Y, the two-magnon peak in LCO does not resonate in the blue but in the green. In LCO, the small peak above the two-magnon peak is weaker for 514 nm and consequently moves closer to the two-magnon peak.

The data show that the B_{1g} spectra have universal features such as the functional dependence at low energy and around the peak maximum. The high-energy parts are surprisingly similar in Y123 and Bi2212:Y but different for LCO. In the following

section, we address the putative universality and possible microscopic descriptions.

5.3.2 Discussion

In Fig. 5.14 the energy and intensity axes of the spectra of Y123, Bi2212:Y, and LCO are normalized. The energy axis is scaled in a way that the maxima of the two-magnon peaks collapse on the canonical value of 2.84 J derived recently using field-theoretical methods [47]. The intensities are normalized to the spectrum of Bi2212:Y using multiplicative factors of 1.11 and 2.27 for the spectra of Y123 and LCO, respectively.

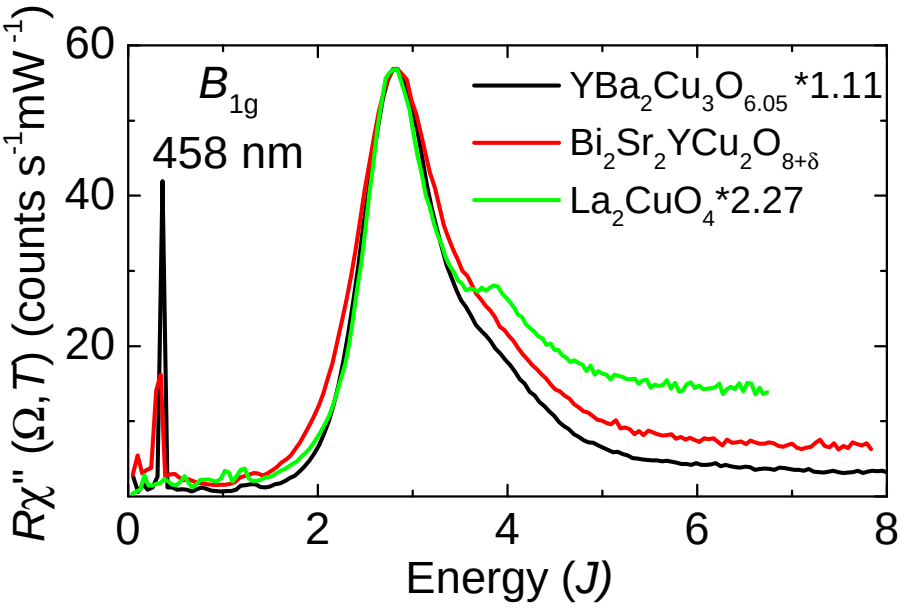

Figure 5.14: Normalized intensity and energy profile of pure B_{1g} symmetry channel for $YBa_2Cu_3O_{6.05}$ (black), $Bi_2Sr_2YCu_2O_{8+\delta}$ (red), and La_2CuO_4 (green). The intensities are scaled by factors as indicated. The energy axis is denoted in units of the exchange coupling constant J. The position of the two-magnon peak matches with the theoretically predicted energy of 2.84 J [47].

At first glance, close to the peak maximum between 2.5 and 3.5 J, the line shapes in all samples look similar. From the position of the two-magnon peak, one can derive the exchange coupling constant J to be 119, 126, and 144 meV for Y123, Bi2212:Y, and LCO, respectively. Our J values for Y123 and LCO are in good agreement with the values of 120 and 143 meV respectively, obtained from neutron scattering experiments [211, 213].

Figure 5.14 shows that Y123 has the smallest line width and the lowest intensity in the high energy regime. This suggests that the Y123 is the cleanest sample and has

the best crystal structure of the three. In the vicinity of the two-magnon peak the spectra of LCO and Y123 match nearly perfectly. However, deviations are observed at low and high energies. Above the two-magnon peak, the LCO spectrum has a secondary maximum at $3.85\,J$. This shoulder depends on the excitation wavelength as discussed in the resonance studies illustrated in Fig. 5.13. We also found that the secondary peak is most likely an intrinsic property since it is independent of the surface preparation method (see section 5.2.4). In the energy region above $5\,J$, the spectra essentially saturate at a constant intensity. However, this intensity varies by more than a factor of 3 for the three samples. The high intensity of the tail of the LCO suggests a contribution from luminescence. For clarification, further work is needed. Bi2212:Y has the broadest two-magnon peak. Otherwise the spectrum looks very similar to that of Y123. The larger width of the two-magnon peak could result from the substantially off-stoichiometric composition of Bi2212:Y and the resulting local variation of the exchange coupling J (inhomogeneous broadening).

The recent field-theoretical calculations have satisfactorily explained the B_{1g} spectra of undoped cuprates [47]. The inclusion of multi-magnon processes and amplitude ("Higgs") fluctuations of the magnetization leads to an improved description of the overall line shapes.

The comparison between experimental data and theoretical calculations for two undoped materials (Y123 and LCO) is presented in Fig. 5.15. These spectra are directly obtained from Ref. [47]. The Raman spectra used for the theoretical fits were measured in 2009 using an excitation wavelength of 458 nm [2]. The experimental data are fitted to a function of the form $A\chi''(\omega/(c_s\Lambda))$. In this expression, A is the overall prefactor which remains undetermined and does not influence the relative weight of the Raman spectrum. The energy scale of the two-magnon response is set by the characteristic frequency $c_s\Lambda$ as discussed in section 5.1.3. The fits to the Raman spectra depend only on two physical quantities: the frequency scale related to J, $c_s\Lambda = \pi\hbar J$ (Eq. 5.11) and the Higgs mass $\tilde{m}_0$ (Eq. 5.12).

Figure 5.15 (a) shows the experimental data and theoretical prediction for Y123. The Raman spectrum (red) is fitted with the theoretical model for two different cases: with and without including the Higgs contribution. The characteristic peak of the two-magnon excitation in B_{1g} symmetry is very well reproduced using a Higgs mass of $\tilde{m}_0 = 0.25$ (blue solid line). When the contribution of the Higgs mass is not included in the calculations, the theoretical curve (blue dashed line) misses a substantial segment of the spectrum between 3500 and 5000 cm^{-1}. The value for the exchange coupling constant J is 126 meV. It matches well with 120 meV obtained

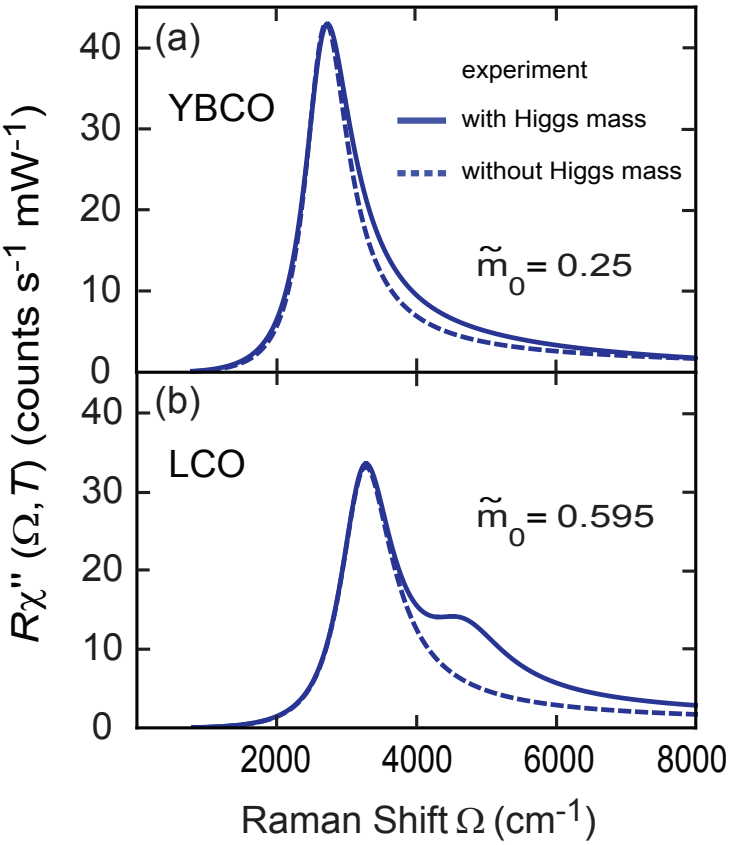

Figure 5.15: Raman response in B_{1g} symmetry for (a) YBCO and (b) LCO. In each case, the experimental results (red squares) are compared with theoretical fits including Higgs contribution (solid blue line) and without Higgs contribution (dashed blue line). $\tilde{m}_0$ is the dimensionless Higgs mass used for the fitted curves. Adopted from Ref. [47].

from neutron scattering [213].

The theoretical fits for LCO are displayed in Fig. 5.15 (b). The spectral comparison reveals that the two-magnon peak is fitted well with the J value of 149 meV close to 143 meV as obtained by neutron scattering [211]. The agreement for the secondary peak at 4600 cm^{-1} could be improved by selecting an intermediate value for the Higgs mass. The solid blue line spectrum reproduces the secondary maximum using a Higgs mass value of $\tilde{m}_0 = 0.595$. The theory prediction underestimates the experimental data thus indicating the contributions from scattering processes other than spin excitations. The computation time is significantly longer if the Higgs corrections are included. Hence, the theoretical curves were obtained by setting a few plausible values for the Higgs mass rather than using a least square fitting procedure which may improve the agreement between theory and experiment.

For Y123, $\tilde{m}_0$ is significantly smaller than for LCO. For the smaller value of the

Higgs mass the spectrum does not exhibit a separate peak. Rather it gives rise to a broad continuum above the dominant two-magnon peak. In the case of LCO, the contribution from the Higgs mode results in a separate peak. A possible origin for the smaller value of the Higgs mass could be associated with the increased quantum fluctuations in the layered system. In bi-layer systems such as Y123, two CuO_2 layers are reasonably close to each other with an AF interlayer exchange coupling of 0.1 [53]. When the interlayer coupling is increased in such systems, a quantum phase transition takes place where a phase of two weakly coupled AF layers transforms into a gapped singlet phase. However, in the phase where two layers possess AF order, the interlayer coupling leads to increased quantum fluctuations resulting in a smaller Higgs mass.

In conclusion, the major part of the B_{1g} spectrum could be explained quantitatively by a recent field-theoretic approach for a spin $S = 1/2$ system. The line shape of the two-magnon peak together with a high energy shoulder could be described well by including magnon-magnon interactions and the amplitude mode. However, there are still a few questions which require further investigations. In LCO, the dependence of the secondary peak at $4600\,\mathrm{cm}^{-1}$ on the excitation lines cannot be described without explicitly including the material's properties, i.e. the electronic structure. The substantial variation upon changing the excitation energy casts doubt on an explanation in terms of amplitude fluctuations alone. In fact, spin excitations and amplitude fluctuations are resonating for different photon energies [Fig. 5.13 (c) and (f)]. The two-magnon peak has a resonance with the excitation wavelength of 514 nm whereas the secondary maximum shows the resonance at 458 nm. In general, one would expect spins and amplitude fluctuations to resonate with the same photon energy since the spins and the amplitude fluctuations are excited via the same intermediate electronic states.

The symmetry-resolved Raman response of LCO shows an extra peak in A_{2g} which is missing in the other compounds (Fig. 5.12). The origin of the A_{2g} maximum could be explained in terms of chiral excitations or multi-magnon excitations that could couple to high-energy electronic states different from those coupling to the double spin-flip excitations. Another possible origin of the high energy shoulder could be explained in terms of triple resonances as discussed by Morr and Chubukov [51]. This phenomenon explains a change in the line shape, however, the dependence of the spectra on high energies could not be predicted using the triple resonance mechanism. The effects obtained in LCO were not present in two other samples. In Y123 and Bi2212:Y, the line shapes do not depend on the excitation energy within

the experimental accuracy. In contrast, the spectral shape of LCO depends slightly on the photon energies.

The study of the magnetic excitations and amplitude fluctuations in the series of three undoped cuprates has revealed a universal line shape close to the double spin-flip maximum in B_{1g} symmetry. The variation of the low-energy response, the nearly Lorentzian variation above the peak and the shoulder between 3.2 and 4.4 J in Y123 and Bi2212:Y found an almost quantitative explanation. In addition, the differences to LCO can at least partially be traced back to a variation of the coupling constant of the Higgs mode. The best agreement between theory and experimental results on the high-energy side could possibly be achieved if the amplitude fluctuations of the magnetization are included. Prior to an improved understanding the exact resonance behavior needs to be studied and the contributions to the inelastic light scattering spectra have to be disentangled.

Chapter 6

Summary

The work described in this thesis is split into two parts. In the first part the progress achieved in assembling and optimizing the setup for tip-enhanced Raman scattering (TERS) is discussed. The second part describes a systematic light scattering study of the spin response in three insulating cuprate systems being prototypical planar spin 1/2 Heisenberg antiferromagnets.

The major part of the work is devoted to the development of the experimental setup of TERS for the temperature range 10 - 300 K. It describes the technical details and challenges of the customized setup. TERS is always a combination of scanning techniques such as atomic force and/or scanning tunneling microscopy (AFM/STM) and light scattering (Raman) spectroscopy. The innovative optical arrangement here is based on an off-axis parabolic mirror where the sample surface is oriented parallel to the optical axis of the mirror. This unconventional orientation enables us to fully control the light polarizations and to minimize the losses due to the aperture reduction. The parabolic mirror is kept at the same temperature as the sample.

The major challenges, arising from the unconventional orientation of the parabolic mirror, include the alignment of the incoming laser beam and of the collection optics with respect to the parabola axis and the efficient illumination of the sample. The two issues could be solved entirely and facilitated the reproducible optimization of the efficiency. In addition, the setup for preparing gold tips for the scanning probes and for tip-enhanced Raman scattering was built up from the scratch.

In a series of measurements, far-field spectra were collected on silicon and YBCO. The silicon spectrum can be recorded with sufficient quality. In contrast, the spectrum of YBCO suffers from a high background signal due to luminescence in the core of the optical fiber. In addition, Raman spectra of silicon were measured in order to test the polarization selection rules upon using the parabolic mirror. The

investigation revealed that the polarization leakage could be suppressed well below 7% when the full aperture of the parabolic mirror is used. It indicates the capabilities of our system to derive the symmetry components of the scattered light while maintaining a high collection efficiency.

The second part of the thesis covers the study of magnetic excitations in CuO_2 systems as a function of light polarization and energy (resonance effects). In three different insulating cuprate systems, La_2CuO_4 (LCO), $YBa_2Cu_3O_{6.05}$ (Y123), and $Bi_2Sr_2YCu_2O_{8+\delta}$ (Bi2212:Y), the symmetry dependence and resonance behavior of the spectral scattering cross section is studied systematically. The spectra in B_{1g} symmetry, as opposed to the other symmetries, are essentially universal. The results obtained in B_{1g} symmetry were compared with the recent field-theoretical calculations based on the microscopic Fleury-Loudon Hamiltonian.

In the symmetry-resolved Raman spectra of all these materials, the B_{1g} channel exhibits a broad and asymmetric two-magnon profile peaking at material-dependent energies. For Y123, Bi2212:Y, and LCO, the peak maxima are observed to be at 2735, 2890, and 3300 cm^{-1} respectively. The quantitative agreement with the predictions of field theory facilitates the precise extraction of the exchange coupling constant J. The J values derived for Y123 and LCO agree to within a few percent with the results derived from the neutron scattering experiments. The line shapes in Y123 and Bi2212:Y are independent of the excitation energies.

In LCO, a prominent secondary maximum is observed at 4600 cm^{-1} which does not show up in Y123 and Bi2212:Y. Yet, the secondary maximum in LCO and the asymmetric line shapes in Y123 and Bi2212:Y can be reproduced theoretically if the amplitude fluctuations of the magnetization (Higgs mode) are included. The weak spectral dependence of the secondary peak on the excitation energies indicates that additional contributions such as multi-magnon process or a triple resonance could also play a role.

Bibliography

[1] K. B. Lyons, P. A. Fleury, J. P. Remeika, A. S. Cooper, and T. J. Negran, *Dynamics of spin fluctuations in lanthanum cuprate*, Phys. Rev. B **37**, 2353 (1988).

[2] B. Muschler, W. Prestel, L. Tassini, R. Hackl, M. Lambacher, A. Erb, S. Komiya, Y. Ando, D. Peets, W. Hardy, R. Liang, and D. Bonn, *Electron interactions and charge ordering in CuO_2 compounds*, Eur. Phys. J. Special Topics **188**, 131 (2010).

[3] J. Ji, A. Zhang, J. Fan, Y. Li, X. Wang, J. Zhang, E. W. Plummer, and Q. Zhang, *Giant magneto-optical Raman effect in a layered transition metal compound*, PNAS **113**, 2349 (2016).

[4] P. E. Sulewski, P. A. Fleury, K. B. Lyons, S.-W. Cheong, and Z. Fisk, *Light scattering from quantum spin fluctuations in R_2CuO_4 (R=La, Nd, Sm)*, Phys. Rev. B **41**, 225 (1990).

[5] B. Schreder, C. Dem, M. Schmitt, A. Materny, W. Kiefer, U. Winkler, and E. Umbach, *Raman spectroscopy of II-VI semiconductor nanostructures: CdS quantum dots*, J. Raman Spectrosc. **34**, 100 (2003).

[6] T. P. Devereaux and R. Hackl, *Inelastic light scattering from correlated electrons*, Rev. Mod. Phys. **79**, 175 (2007).

[7] D. J. Scalapino and T. P. Devereaux, *Collective d-wave exciton modes in the calculated Raman spectrum of Fe-based superconductors*, Phys. Rev. B **80**, 140512 (2009).

[8] T. Böhm, A. F. Kemper, B. Moritz, F. Kretzschmar, B. Muschler, H. M. Eiter, R. Hackl, T. P. Devereaux, D. J. Scalapino, and H.-H. Wen, *Balancing act: Evidence for a strong subdominant d-wave pairing channel in $Ba_{0.6}K_{0.4}Fe_2As_2$*, Phys. Rev. X **4**, 041046 (2014).

[9] P. A. Fleury and R. Loudon, *Scattering of light by one- and two-magnon excitations*, Physical Review **166**, 514 (1968).

[10] K. B. Lyons, P. A. Fleury, L. F. Schneemeyer, and J. V. Waszczak, *Spin fluctuations and superconductivity in* $Ba_2Cu_3O_{6+\delta}$, Phys. Rev. Lett. **60**, 732 (1988).

[11] K. B. Lyons, P. E. Sulewski, P. A. Fleury, H. L. Carter, A. S. Cooper, G. P. Espinosa, Z. Fisk, and S.-W. Cheong, *High-energy spin and charge excitations in* La_2CuO_4, Phys. Rev. B **39**, 9693 (1989).

[12] S. Sugai, M. Sato, T. Kobayashi, J. Akimitsu, T. Ito, H. Takagi, S. Uchida, S. Hosoya, T. Kajitani, and T. Fukuda, *High-energy spin excitations in the insulating phases of high-*T_c *superconducting cuprates and* La_2NiO_4, Phys. Rev. B **42**, 1045 (1990).

[13] P. E. Sulewski, P. A. Fleury, K. B. Lyons, and S.-W. Cheong, *Observation of chiral spin fluctuations in insulating planar cuprates*, Phys. Rev. Lett. **67**, 3864 (1991).

[14] C. M. Canali and S. M. Girvin, *Theory of Raman scattering in layered cuprate materials*, Phys. Rev. B **45**, 7127 (1992).

[15] A. V. Chubukov and D. M. Frenke, *Resonant two-magnon Raman scattering in antiferromagnetic insulators*, Phys. Rev. Lett. **74**, 3057 (1995).

[16] M. Rübhausen, N. Dieckmann, A. Bock, and U. Merkt, *Line-shape analyses of magnon Raman spectra of a* $Pr_2Cu_{2.7}Al_{0.3}O_7$ *single crystal*, Phys. Rev. B **54**, 14967 (1996).

[17] K. M. Lang, V. Madhavan, J. E. Hoffman, E. W. Hudson, H. Eisaki, S. Uchida, and J. C. Davis, *Imaging the granular structure of high-*T_c *superconductivity in underdoped* $Bi_2Sr_2CaCu_2O_{8+\delta}$, Nature **415**, 412 (2002).

[18] A. N. Pasupathy, A. Pushp, K. K. Gomes, C. V. Parker, J. Wen, Z. Xu, G. Gu, S. Ono, Y. Ando, and A. Yazdani, *Electronic origin of the inhomogeneous pairing interaction in the high-*T_c *superconductor* $Bi_2Sr_2CaCu2O_{8+\delta}$, Science **320**, 196 (2008).

[19] Y. Kim, M. Alexe, and E. K. H. Salje, *Nanoscale properties of thin twin walls and surface layers in piezoelectric* WO_{3-x}, Appl. Phys. Lett. **96**, 032904 (2010).

[20] S. Mühlbauer, B. Binz, F. Jonietz, C. Pfleiderer, A. Rosch, A. Neubauer, R. Georgii, and P. Böni, *Skyrmion lattice in a chiral magnet*, Science **323**, 915 (2009).

[21] J. Wessel, *Surface-enhanced optical microscopy*, J. Opt. Soc. Am. **2**, 1538 (1985).

[22] A. Hartschuh, *Tip-enhanced near-field optical microscopy*, Angew. Chem. Int. Ed. **47**, 8178 (2008).

[23] J. Steidtner and B. Pettinger, *High-resolution microscope for tip-enhanced optical processes in ultrahigh vacuum*, Rev. Sci. Instrum. **78**, 103104 (2007).

[24] B. Pettinger, P. Schambach, C. J. Villagomez, and N. Scott, *Tip-enhanced Raman spectroscopy: Near-fields acting on a few molecules*, Annu. Rev. Phys. Chem. **63**, 379 (2012).

[25] R. M. Stöckle, Y. D. Suh, V. Deckert, and R. Zenobi, *Nanoscale chemical analysis by tip-enhanced Raman spectroscopy*, Chem. Phys. Lett. **318**, 131 (2000).

[26] M. S. Anderson, *Locally enhanced Raman spectroscopy with an atomic force microscope*, Appl. Phys. Lett. **76**, 3130 (2000).

[27] B. Pettinger, G. Picardi, R. Schuster, and G. Ertl, *Surface-enhanced and STM tip-enhanced Raman spectroscopy of CN− ions at gold surfaces*, J. Electroanal. Chem. **554**, 293 (2003).

[28] A. Hartschuh, E. J. Sánchez, X. S. Xie, and L. Novotny, *High-resolution near-field Raman microscopy of single-walled carbon nanotubes*, Phys. Rev. Lett. **90**, 095503 (2003).

[29] L. G. Cancado, A. Hartschuh, and L. Novotny, *Tip-enhanced Raman spectroscopy of carbon nanotubes*, J. Raman Spectrosc. **40**, 1420 (2009).

[30] R. Beams, L. G. Cancado, A. Jorio, A. N. Vamivakas, and L. Novotny, *Tip-enhanced Raman mapping of local strain in graphene*, Nanotechnology **26**, 175702 (2015).

[31] K.-D. Park, O. Khatib, V. Kravtsov, G. Clark, X. Xu, and M. B. Raschke, *Hybrid tip-enhanced nanospectroscopy and nanoimaging of monolayer WSe_2 with local strain control*, Nano Lett. **16**, 2621 (2016).

[32] R. Zhang, Y. Zhang, Z. C. Dong, S. Jiang, C. Zhang, L. G. Chen, L. Zhang, Y. Liao, J. Aizpurua, Y. Luo, J. L. Yang, and J. G.Hou, *Chemical mapping of a single molecule by plasmon-enhanced Raman scattering*, Nature **498**, 82 (2013).

[33] J. M. Klingsporn, N. Jiang, E. A. Pozzi, M. D. Sonntag, D. Chulhai, T. Seideman, L. Jensen, M. C. Hersam, and R. P. V. Duyne, *Intramolecular insight into adsorbate-substrate interactions via low-temperature, ultrahigh-vacuum tip-enhanced Raman spectroscopy*, J. Am. Chem. Soc. **136**, 3881 (2014).

[34] J. J. Wang, D. A. Smith, D. N. Batchelder, Y. Saito, J. Kirkham, C. . Robinson, K. Baldwin, G. Li, and B. Bennett, *Apertureless near-field Raman spectroscopy*, J. Microsc. **210**, 330 (2003).

[35] N. Hayazawa, A. Tarun, Y. Inouye, and S. Kawata, *Near-field enhanced Raman spectroscopy using side illumination optics*, J. Appl. Phys. **92**, 6983 (2002).

[36] W. Sun and Z. Shen, *A practical nanoscopic Raman imaging technique realized by near-field enhancement*, Materials Physics and Mechanics **4**, 17 (2001).

[37] M. Sackrow, C. Stanciu, M. A. Lieb, and A. J. Meixner, *Imaging nanometre-sized hot spots on smooth Au films with high-resolution tip-enhanced luminescence and Raman near-field optical microscopy*, ChemPhysChem **9**, 316 (2008).

[38] S. Chakravarty, B. I. Halperin, and D. R. Nelson, *Two-dimensional quantum Heisenberg antiferromagnet at low temperatures*, Phys. Rev. B **39**, 2344 (1989).

[39] M. A. Kastner, R. J. Birgeneau, G. Shirane, and Y. Endoh, *Magnetic, transport, and optical properties of monolayer copper oxides*, Rev. Mod. Phys. **70**, 897 (1998).

[40] R. Coldea, S. M. Hayden, G. Aeppli, T. G. Perring, C. D. Frost, T. E. Mason, S. W. Cheong, and Z. Fisk, *Spin waves and electronic interactions in La_2CuO_4*, Phys. Rev. Lett. **86**, 5377 (2001).

[41] B. Keimer, P. Bourges, H. F. Fong, G. D. Gu, H. He, A. Ivanov, N. Koshizuka, B. Liang, C. T. Lin, L. P. Regnault, Y. Sidis, and E. Schoenherr, *Spin excitations in cuprates: From underdoped to overdoped state*, Physica C: Superconductivity **341-348**, 2113 (2000).

[42] J. M. Tranquada, *Spins, stripes, and superconductivity in hole-doped cuprates*, AIP Conference Proceedings **1550**, 114 (2013).

[43] P. Knoll, C. Thomsen, M. Cardona, and P. Murugaraj, *Temperature-dependent lifetime of spin excitations in $RBa_2Cu_3O_6$ (R=Eu, Y)*, Phys. Rev. B **42**, 4842 (1990).

[44] B. S. Shastry and B. I. Shraiman, *Theory of Raman scattering in Mott-Hubbard systems*, Phys. Rev. Lett. **65**, 1068 (1990).

[45] F. H. Vernay, M. J. P. Gingras, and T. P. Devereaux, *Momentum-dependent light scattering in insulating cuprates*, Phys. Rev. B **75**, 020403 (2007).

[46] D. Podolsky, A. Auerbach, and D. P. Arovas, *Visibility of the amplitude (Higgs) mode in condensed matter*, Phys. Rev. B **84**, 174522 (2011).

[47] S. A. Weidinger and W. Zwerger, *Higgs mode and magnon interactions in 2D quantum antiferromagnets from Raman scattering*, Eur. Phys. J. B **88**, 237 (2015).

[48] R. N. Cahn, *The Higgs boson*, Rep. Prog. Phys. **52**, 389 (1989).

[49] G. M. Bruun, *Long-lived Higgs mode in a two-dimensional confined Fermi system*, Phys. Rev. A **90**, 023621 (2014).

[50] A. V. Chubukov and D. M. Frenkel, *Resonant two-magnon Raman scattering in parent compounds of high-T_c superconductors*, Phys. Rev. B **52**, 9760 (1995).

[51] D. K. Morr and A. V. Chubukov, *Resonant Raman scattering in antiferromagnets*, Phys. Rev. B **56**, 9134 (1997).

[52] W. Brenig, P. Knoll, and M. Mayer, *Resonant two-magnon Raman efficiency of the antiferromagnetic cuprates: Theory and experiment*, Physica B **237**, 95 (1997).

[53] G. Blumberg, P. Abbamonte, M. V. Klein, W. C. Lee, D. M. Ginsberg, L. L. Miller, and A. Zibold, *Resonant two-magnon Raman scattering in cuprate antiferromagnetic insulators*, Phys. Rev. B **53**, R11930 (1996).

[54] E. Abbé, *Beitrläge zur Theorie des Mikroskops und der mikroskopischen Wahrnehmung*, Archiv für Mikroskopische Anatomie **9**, 413 (1873).

[55] L. Rayleigh, *Investigations in optics, with special reference to the spectroscope*, The London, Edinburgh, and Dublin Philosophical Magazine and Journal of Science **8**, 261 (1879).

[56] J. J. Greffet and R. Carminati, *Image formation in near-field optics*, Prog. Surf. Sci. **56**, 133 (1997).

[57] M. Born and E. Wolf, *Principles of Optics* (Cambridge University Press, ADDRESS, 1999).

[58] L. Novotny and B. Hecht, *Principles of Nano-Optics* (Cambridge University Press, ADDRESS, 2006).

[59] S. W. Hell, E. H. K. Stelzer, S. Lindek, and C. Cremer, *Confocal microscopy with an increased detection aperture: type-B 4Pi confocal microscopy*, Opt. Lett. **19**, 222 (1994).

[60] J. N. Anker, W. P. Hall, O. Lyandres, N. C. Shah, J. Zhao, and R. P. V. Duyne, *Biosensing with plasmonic nanosensors*, Nat. Mater. **7**, 442 (2008).

[61] D. K. Gramotnev and S. I. Bozhevolnyi, *Plasmonics beyond the diffraction limit*, Nat. Photonics **4**, 83 (2010).

[62] T. Zhang and F. Shan, *Development and application of surface plasmon polaritons on optical amplification*, Journal of Nanomaterials **2014**, 1 (2014).

[63] P. Johns, K. Yu, M. S. Devadas, and G. V. Hartland, *Role of resonances in the transmission of surface plasmon polaritons between nanostructures*, ACS Nano **10**, 3375 (2016).

[64] N. W. Ashcroft and N. D. Mermin, *Solid State Physics* (Philadelphia: Saunders College Publishing, ADDRESS, 1976).

[65] H. Ehrenreich and H. R. Philipp, *Optical properties of Ag and Cu*, Phys. Rev. **128**, 1622 (1962).

[66] A. Otto, *Excitation of nonradiative surface plasma waves in silver by the method of frustrated total reflection*, Zeitschrift für Physik **216**, 398 (1968).

[67] E. Kretschmann, *Die Bestimmung optischer Konstanten von Metallen durch Anregung von Oberflächenplasmaschwingungen*, Zeitschrift für Physik **241**, 313 (1971).

[68] B. Hecht, H. Bielefeldt, L. Novotny, Y. Inouye, and D. W. Pohl, *Local excitation, scattering and interference of surface plasmons*, Phys. Rev. Lett. **77**, 1889 (1996).

[69] H. Synge, *A suggested model for extending microscopic resolution into the ultra-microscopic region*, Philos. Mag. **6**, 356 (1928).

[70] A. Ash and G. Nicholls, *Super-resolution aperture scanning microscope*, Nature **237**, 510 (1972).

[71] D. Pohl, W. Denk, and M. Lanz, *Optical stethoscopy: Image recording with resolution λ/20*, Appl. Phys. Lett. **44**, 651 (1984).

[72] B. Knoll and F. Keilmann, *Near-field probing of vibrational absorption for chemical microscopy*, Nature **399**, 134 (1999).

[73] B. Hecht, B. Sick, U. P. Wild, V. Deckert, R. Zenobi, O. J. F. Martin, and D. W. Pohl, *Scanning near-field optical microscopy with aperture probes: Fundamentals and applications*, J. Chem. Phys. **112**, 7761 (2000).

[74] B. I. Yakobson and M. A. Paesler, *Kinetics, morphology and pulling regimes for sensing tips in near-field microscopy*, Ultramicroscopy **57**, 241 (1995).

[75] B. A. F. Puygranier and P. Dawson, *Chemical etching of optical fibre tips-experiment and model*, Ultramicroscopy **85**, 235 (2000).

[76] M. Ohtsu, *Photon STM: from imaging to fabrication*, Optoelectronics- Devices and Technologies **10**, 147 (1995).

[77] L. Novotny and C. Hafner, *Light propagation in a cylindrical waveguide with a complex, metallic, dielectric function*, Phys. Rev. E **50**, 4094 (1994).

[78] T. H. Taminiau, R. J. Moerland, F. B. Segerink, L. Kuipers, and N. F. van Hulst, *Resonance of an optical monopole antenna probed by single molecule fluorescence*, Nano Lett. **7**, 28 (2007).

[79] L. Neumann, Y. Pang, A. Houyou, M. L. Juan, R. Gordon, and N. F. van Hulst, *Extraordinary optical transmission brightens near-field fiber probe*, Nano Lett. **11**, 355 (2011).

[80] W. Bao, M. Melli, N. Caselli, F. Riboli, D. S. Wiersma, M. Staffaroni, H. Choo, D. F. Ogletree, S. Aloni, J. Bokor, S. Cabrini, F. Intonti, M. B. Salmeron,

E. Yablonovitch, P. J. Schuck, and A. Weber-Bargioni, *Mapping local charge recombination heterogeneity by multidimensional nanospectroscopic imaging*, Science **338**, 1317 (2012).

[81] M. Fleischer, *Near-field scanning optical microscopy nanoprobes*, Nanotechnology Reviews **1**, 313 (2012).

[82] A. L. Lereu, A. Passian, and P. Dumas, *Near field optical microscopy: A brief review*, Int. J. Nanotechnol. **9**, 488 (2012).

[83] P. J. Schuck, A. Weber-Bargioni, P. D. Ashby, D. F. Ogletree, A. Schwartzberg, and S. Cabrini, *Life beyond diffraction: Opening new routes to materials characterization with next-generation optical near-field approaches*, Adv. Funct. Mater. **23**, 2539 (2013).

[84] L. Novotny and S. J. Stranick, *Near-field optical microscopy and spectroscopy with pointed probes*, Annu. Rev. Phys. Chem. **57**, 303 (2006).

[85] A. Bek, R. Vogelgesang, and K. Kern, *Apertureless scanning near field optical microscope with sub-10 nm resolution*, Rev. Sci. Instrum. **77**, 043703 (2006).

[86] M. Schnell, A. G.-Etxarri, J. Alkorta, J. Aizpurua, and R. Hillenbrand, *Phase-resolved mapping of the near-field vector and polarization state in nanoscale antenna gaps*, Nano Lett. **10**, 3524 (2010).

[87] B. Hecht, H. Bielefeldt, Y. Inouye, and D. W. Pohl, *Facts and artifacts in near-field optical microscopy*, J. Appl. Phys. **81**, 2492 (1997).

[88] L. Novotny, E. J. Sanchez, and X. S. Xie, *Near-field optical imaging using metal tips illuminated by higher-order Hermite-Gaussian beams*, Ultramicroscopy **71**, 21 (1998).

[89] N. Mauser and A. Hartschuh, *Tip-enhanced near-field optical microscopy*, Chem. Soc. Rev. **43**, 1248 (2014).

[90] L. Eligal, F. Culfaz, V. McCaughan, N. I. Cade, and D. Richards, *Etching gold tips suitable for tip-enhanced near-field optical microscopy*, Rev. Sci. Instrum. **80**, 033701 (2009).

[91] C. Williams and D. Roy, *Fabrication of gold tips suitable for tip-enhanced Raman spectroscopy*, J. Vac. Sci. Technol. B **26**, 1761 (2008).

[92] W. Zhang, B. S. Yeo, T. Schmid, and R. Zenobi, *Single molecule tip-enhanced Raman spectroscopy with silver tips*, J. Phys. Chem. C **111**, 1733 (2007).

[93] C. V. Raman and K. S. Krishnan, *A new type of secondary radiation*, Nature **121**, 501 (1928).

[94] G. Landsberg and L. Mandelstam, *Über die Lichtzerstreuung in Kristallen*, Zeitschrift für Physik **50**, 769 (1928).

[95] D. Mehtani, N. Lee, R. D. Hartschuh, A. Kisliuk, M. D. Foster, A. P. Sokolov, and J. F. Maguire, *Nano-Raman spectroscopy with side-illumination optics*, J. Raman Spectrosc. **36**, 1068 (2005).

[96] C. Georgi and A. Hartschuh, *Tip enhanced Raman spectroscopic imaging of localized defects in carbon nanotubes*, Appl. Phys. Lett. **97**, 143117 (2010).

[97] N. Mauser, D. Piatkowski, T. Mancabelli, M. Nyk, S. Mackowski, and A. Hartschuh, *Tip enhancement of upconversion photoluminescence from rare earth ion doped nanocrystals*, ACS Nano **9**, 3617 (2015).

[98] M. Chaigneau, G. Picardi, and R. Ossikovski, *Tip enhanced Raman spectroscopy evidence for amorphous carbon contamination on gold surfaces*, Surf. Sci. **604**, 701 (2010).

[99] A. Rasmussen and V. Deckert, *Surface and tip enhanced Raman scattering of DNA components*, J. Raman Spectrosc. **37**, 311 (2006).

[100] R. Boehme, D. Cialla, M. Richter, P. Roesch, J. Popp, and V. Deckert, *Biochemical imaging below the diffraction limit-probing cellular membrane related structures by tip-enhanced Raman spectroscopy (TERS)*, J. Biophoton. **3**, 455 (2010).

[101] P. Hermann, A. H. V. L. G. H. L. Moeller, N. Bannertb, and D. Naumann, *Evaluation of tip-enhanced raman spectroscopy for characterizing different virus strains*, Analyst **136**, 1148 (2011).

[102] A. McQuillan, P.J.Hendra, and M. Fleischmann, *Raman spectroscopic investigation of silver electrodes*, J. Electroanal. Chem. **65**, 933 (1975).

[103] M. Fleischmann, P. Hendra, A. J. McQuillan, R. L. Paul, and E. S. Reid, *Raman spectroscopy at electrode-electrolyte interfaces*, J. Raman Spectrosc. **4**, 269 (1976).

[104] D. L. Jeanmaire and R. P. V. Duyne, *Surface Raman electrochemistry Part 1-Heterocyclic, aromatic, and aliphatic-amines adsorbed on the anodized silver electrode*, J. Electroanal. Chem. **84**, 1 (1977).

[105] B. Sharma, R. R. Frontiera, A.-I. Henry, E. Ringe, and R. P. V. Duyne, *SERS: Materials, applications, and the future*, Materials Today **15**, 16 (2012).

[106] D. Richards, R. G. Milner, F. Huang, and F. Festy, *Tip-enhanced Raman microscopy: Practicalities and limitations*, J. Raman Spectrosc. **34**, 663 (2003).

[107] S. L. McCall and P. M. Platzman, *Raman scattering from chemisorbed molecules at surfaces*, Physical Review B **22**, 1660 (1980).

[108] M. Moskovits, *Surface enhanced Spectroscopy*, Rev. Mod. Phys. **57**, 783 (1985).

[109] J. Billmann and A. Otto, *Electronic surface state contribution to surface enhanced Raman scattering*, Solid State Commun. **44**, 105 (1982).

[110] J. R. Lombardi, R. L. Birke, T. Lu, and J. Xu, *Charge transfer theory of surface enhanced Raman spectroscopy : Herzberg-Teller contributions*, J. Chem. Phys. **84**, 4174 (1986).

[111] L. Novotny, R. X. Bian, and X. S. Xie, *Theory of nanometric optical tweezers*, Phys. Rev. Lett. **79**, 645 (1997).

[112] A. V. Ermushev, B. V. Mchedlishvili, V. A. Oleinikov, and A. V. Petukhov, *Surface enhancement of local optical fields and the lightning-rod effect*, Quantum Electronics **23**, 435 (1993).

[113] M. Zhang, R. Wang, Z. Zhu, J. Wang, and Q. Tian, *Experimental research on the spectral response of tips for tip-enhanced Raman spectroscopy*, J. Opt. **15**, 055006 (2013).

[114] T. Schmid, L. Opilik, C. Blum, and R. Zenobi, *Nanoscale chemical imaging using tip-enhanced Raman spectroscopy: A critical review*, Angew. Chem., Int. Ed. **52**, 5940 (2013).

[115] A. B. Zrimsek, N. Chiang, M. Mattei, S. Zaleski, M. O. McAnally, C. T. Chapman, A.-I. Henry, G. C. Schatz, and R. P. V. Duyne, *Single-molecule chemistry with Surface- and Tip-enhanced Raman spectroscopy*, Chem. Rev. **117**, 7583 (2017).

[116] B. Pettinger, B. Ren, G. Picardi, R. Schuster, and G. Ertl, *Nanoscale probing of adsorbed species by tip-enhanced Raman spectroscopy*, Phys. Rev. Lett. **92**, 096101 (2004).

[117] T. Schmid, B. Yeo, W. Zhang, and R. Zenobi, in *Tip Enhancement*, edited by S. Kawata and V. Shalaev (Elsevier Science, ADDRESS, 2006), Chap. Use of tip-enhanced vibrational spectroscopy for analytical applications in chemistry, biology and materials science, pp. 115–155.

[118] A. L. Demming, F. Festy, and D. Richards, *Plasmon resonances on metal tips: Understanding tip-enhanced Raman scattering*, J. Chem. Phys. **122**, 187416 (2005).

[119] L. T. Nieman, G. M. Krampert, and R. E. Martinez, *An apertureless near-field scanning optical microscope and its application to surface-enhanced Raman spectroscopy and multiphoton fluorescence imaging*, Rev. Sci. Instrum. **72**, 1691 (2001).

[120] D. Roy, J. Wang, and C. Williams, *Novel methodology for estimating the enhancement factor for tip-enhanced Raman spectroscopy*, J. Appl. Phys. **105**, 013530 (2009).

[121] N. Kumar, S. Mignuzzi, W. Su, and D. Roy, *Tip-enhanced Raman spectroscopy: principles and applications*, EPJ Techniques and Instrumentation **2**, (2015).

[122] M. Futamata, Y. Maruyama, and M. Ishikawa, *Local electric field and scattering cross section of Ag nanoparticles under surface plasmon resonance by finite difference time domain method*, J. Phys. Chem. B **107**, 7607 (2003).

[123] L. Meng, T. Huang, X. Wang, S. Chen, Z. Yang, and B. Ren, *Gold-coated AFM tips for tip-enhanced Raman spectroscopy: theoretical calculation and experimental demonstration*, Opt. Express **23**, 13804 (2015).

[124] J. P. Kottmann, O. J. Martin, D. R. Smith, and S. Schultz, *Dramatic localized electromagnetic enhancement in plasmon resonant nanowires*, Chem. Phys. Lett. **341**, 1 (2001).

[125] D. Zhang, X. Wang, K. Braun, H.-J. Egelhaaf, M. Fleischer, L. Hennemann, H. Hintz, C. Stanciu, C. J. Brabec, D. P. Kern, and A. J.Meixnera, *Parabolic*

mirror-assisted tip-enhanced spectroscopic imaging for non-transparent materials, J. Raman Spectrosc. **40**, 1371 (2009).

[126] Z. Yang, J. Aizpurua, and H. Xu, *Electromagnetic field enhancement in TERS configurations*, J. Raman Spectrosc. **40**, 1343 (2009).

[127] N. Hayazawa, Y. Inouye, Z. Sekkat, and Sato, *Near-field Raman scattering enhanced by a metallized tip*, Chem. Phys. Lett. **335**, 369 (2001).

[128] N. Hayazawa, Y. Inouye, Z. Sekkat, and S. Kawata, *Near-field Raman imaging of organic molecules by an apertureless metallic probe scanning optical microscope*, J. Chem. Phys. **117**, 1296 (2002).

[129] M. S. Anderson and W. T. Pike, *A Raman-atomic force microscope for apertureless-near-field spectroscopy and optical trapping*, Rev. Sci. Instrum. **73**, 1198 (2002).

[130] V. Poborchii, T. Tada, and T. Kanayama, *Subwavelength-resolution Raman microscopy of Si structures using metal-particle-topped AFM probe*, Japanese Journal of Applied Physics **44**, 202 (2005).

[131] K. L. A. Chan and S. G. Kazarian, *Tip-enhanced Raman mapping with top-illumination AFM*, Nanotechnology **22**, 175701 (2011).

[132] M. A. Lieb and A. J. Meixner, *A high numerical aperture parabolic mirror as imaging device for confocal microscope*, Opt. Express **8**, 458 (2001).

[133] C. Stanciu, M. Sackrow, and A. Meixner, *High NA particle- and tip-enhanced nanoscale Raman spectroscopy with a parabolic-mirror microscope*, J. Microsc. **229**, 247 (2008).

[134] R. Dorn, S. Quabis, and G. Leuchs, *Sharper focus for a radially polarized light beam*, Phys. Rev. Lett. **91**, 233901 (2003).

[135] N. Davidson and N. Bokor, *High-numerical-aperture focusing of radially polarized doughnut beams with a parabolic mirror and a flat diffractive lens*, Opt. Lett. **29**, 1318 (2004).

[136] G. Binnig, H. Rohrer, C. Gerber, and E. Weibel, *Tunneling through a controllable vacuum gap*, Appl. Phys. Lett. **40**, 178 (1982).

[137] G. Binning, H. Rohrer, C. Gerber, and E. Weibel, *Surface studies by scanning tunneling microscopy*, Phys. Rev. Lett. **49**, 57 (1982).

[138] M. D. Kirk, J. Nogami, A. A. Baski, D. B. Mitzi, A. Kapitulnik, T. H. Geballe, and C. F. Quate, *The origin of the superstructure in $Bi_2Sr_2CaCu_2O_{8+\delta}$ as revealed by scanning tunneling microscopy*, Science **242**, 1673 (1988).

[139] T. Matsumoto, H. Tanaka, T. Kawai, and S. Kawai, *STM-imaging of a $SrTiO_3$ (100) surface with atomic-scale resolution*, Surf. Sci. Lett. **278**, 153 (1992).

[140] H. F. Hess, R. B. Robinson, R. C. Dynes, J. M. V. Jr., and J. V. Waszczak, *Scanning-tunneling-microscope observation of the Abrikosov flux lattice and the density of states near and inside a fluxoid*, Phys. Rev. Lett. **62**, 214 (1989).

[141] K. Ikeda, K. Takamuku, R. I. H. Kubota, and N. Koshizuka, *A low-temperature ultrahigh vacuum scanning tunneling microscope system and tunneling spectra of the Bi2212 superconductor*, Rev. Sci. Instrum. **64**, 2221 (1993).

[142] C. Renner and O. Fischer, *Non BCS IV characteristics of superconducting $Bi_2Sr_2CaCu_2O_{8+\delta}$ single crystals*, Physica C **235**, 53 (1994).

[143] O. Fischer, M. Kugler, I. M.-Aprile, and C. Berthod, *Scanning tunneling spectroscopy of high-temperature superconductors*, Rev. Mod. Phys. **79**, 353 (2007).

[144] Q. Fan, W. H. Zhang, X. Liu, Y. J. Yan, M. Q. Ren, R. Peng, H. C. Xu, B. P. Xie, J. P. Hu, T. Zhang, and D. L. Feng, *Plain s-wave superconductivity in single-layer FeSe on $SrTiO_3$ probed by scanning tunnelling microscopy*, Nature Physics **11**, 946 (2015).

[145] C. F. Hirjibehedin, C. P. Lutz, and A. J. Heinrich, *Spin coupling in engineered atomic structures*, Science **312**, 1021 (2006).

[146] C. Hanneken, F. Otte, A. Kubetzka, B. Dupé, N. Romming, K. von Bergmann, R. Wiesendanger, and S. Heinze, *Electrical detection of magnetic skyrmions by tunnelling non-collinear magnetoresistance*, Nature Nanotechnology **10**, 1039 (2015).

[147] I. Swart, T. Sonnleitner, J. Niedenfuehr, and J. Repp, *Controlled lateral manipulation of molecules on insulating films by STM*, Nano Lett. **12**, 1070 (2012).

[148] J. Yang, D. Sordes, M. Kolmer, D. Martrou, and C. Joachim, *Imaging, single atom contact and single atom manipulations at low temperature using the new ScientaOmicron LT-UHV-4 STM*, Eur. Phys. J. Appl. Phys. **73**, 10702 (2016).

[149] P. Avouris, R. Walkup, A. Rossi, H. Akpati, P. Nordlander, T. Shen, G. Abeln, and J. Lyding, *Breaking individual chemical bonds via STM induced excitations*, Surf. Sci. **363**, 368 (1996).

[150] O. Stetsovych, M. Todorovic, T. K. Shimizu, C. Moreno, J. W. Ryan, C. P. Leon, K. Sagisaka, E. Palomares, V. Matolin, D. Fujita, R. Perez, and O. Custance, *Atomic species identification at the (101) anatase surface by simultaneous scanning tunnelling and atomic force microscopy*, Nature Communications **6**, 7265 (2015).

[151] G. Binnig, C. F. Quate, and C. Gerber, *Atomic force microscope*, Phys. Rev. Lett. **56**, 930 (1986).

[152] https://amyhallr.wordpress.com/2013/03/15/atomic-force microscopy/.

[153] H. Edwards, L. Taylor, and W. Duncan, *Fast, high-resolution atomic force microscopy using a quartz tuning fork as actuator and sensor*, J. Appl. Phys. **82**, 980 (1997).

[154] A. G. T. Ruiter, K. O. van der Werf, J. A. Veerman, M. F. Garcia-Parajo, W. H. J. Rensen, and N. F. van Hulst, *Tuning fork shear-force feedback*, Ultramicroscopy **71**, 149 (1998).

[155] K. Karrai and I. Tiemann, *Interfacial shear force microscopy*, Phys. Rev. B **62**, 13174 (2000).

[156] K. Karrai and R. D. Grober, *Piezoelectric tip-sample distance control for near field optical microscopes*, Appl. Phys. Lett. **66**, 1842 (1995).

[157] T. Ichimura, S. Fujii, P. Verma, T. Yano, Y. Inouye, and S. Kawata, *Subnanometric near-field Raman investigation in the vicinity of a metallic nanostructure*, Phys. Rev. Lett. **102**, 186101 (2009).

[158] S. S. Kharintsev, G. G. Hoffmann, P. S. Dorozhkin, G. D. With, and J. Loos, *Atomic force and shear force based tip-enhanced Raman spectroscopy and imaging*, Nanotechnology **18**, 315502 (2007).

[159] N. K. Zanjani, S. Vedraine, and F. L. Labarthet, *Localized enhancement of electric field in tip-enhanced Raman spectroscopy using radially and linearly polarized light*, Opt. Express **21**, 25271 (2013).

[160] T.-X. Huang, S.-C. Huang, M.-H. Li, Z.-C. Zeng, X. Wang, and B. Ren, *Tip-enhanced Raman spectroscopy: tip-related issues*, Anal. Bioanal.Chem. **407**, 8177 (2015).

[161] B. S. Yeo, T. Schmid, W. Zhang, and R. Zenobi, *Towards rapid nanoscale chemical analysis using tip-enhanced Raman spectroscopy with Ag-coated dielectric tips*, Anal. Bioanal.Chem. **387**, 2655 (2007).

[162] N. Hayazawa, T. Yano, and S. Kawata, *Highly reproducible tip-enhanced Raman scattering using an oxidized and metallized silicon cantilever tip as a tool for everyone*, J. Raman Spectrosc. **43**, 1177 (2012).

[163] K. Dickmann, F. Demming, and J. Jersch, *New etching procedure for silver scanning tunneling microscopy tips*, Rev. Sci. Instrum. **67**, 845 (1996).

[164] M. Iwami, Y. Uehara, and S. Ushioda, *Preparation of silver tips for scanning tunneling microscopy imaging*, Rev. Sci. Instrum. **69**, 4010 (1998).

[165] M. Li, R. Lv, S. Huang, Y. Dai, Z. Zeng, L. Wang, and B. Ren, *Electrochemical fabrication of silver tips for tip-enhanced Raman spectroscopy assisted by a machine vision system*, J. Raman Spectrosc. **47**, 808 (2016).

[166] P. A. Hodgson, Y. Wang, A. A. Mohammad, and P. Kruse, *Note: Electrochemical etching of silver tips in concentrated sulfuric acid*, Rev. Sci. Instrum. **84**, 026109 (2013).

[167] B. Ren, G. Picardi, and B. Pettinger, *Preparation of gold tips suitable for tip-enhanced Raman spectroscopy and light emission by electrochemical etching*, Rev. Sci. Instrum. **75**, 837 (2004).

[168] L. Billot, L. Berguiga, M. de la Chapellea, Y. Gilbert, and R. Bachelot, *Production of gold tips for tip-enhanced near-field optical microscopy and spectroscopy: analysis of the etching parameters*, Eur. Phys. J. Appl. Phys. **31**, 139 (2005).

[169] C. Williams and D. Roy, *Fabrication of gold tips suitable for tip-enhanced Raman spectroscopy*, J. Vac. Sci. Technol. B **26**, 1761 (2008).

[170] M. Eisele, M. Krüger, M. Schenk, A. Ziegler, and P. Hommelhoff, *Note: Production of sharp gold tips with high surface quality*, Rev. Sci. Instrum. **82**, 026101 (2011).

[171] I. U. Vakarelski and K. Higashitani, *Single-nanoparticle-terminated tips for scanning probe microscopy*, Langmuir **22**, 2931 (2006).

[172] T. Kalkbrenner, M. Ramstein, J. Mlynek, and V. Sandoghdar, *A single gold particle as a probe for apertureless scanning near-field optical microscopy*, J. Microsc. **202**, 72 (2001).

[173] I. Barsegova, A. Lewis, A. Khatchatouriants, A. Manevitch, A. Ignatov, N. Axelrod, and C. Sukenik, *Controlled fabrication of silver or gold nanoparticle near-field optical atomic force probes: Enhancement of second-harmonic generation*, Appl. Phys. Lett. **81**, 3461 (2002).

[174] L. Novotny and N. van Hulst, *Antennas for light*, Nature Photonics **5**, 83 (2011).

[175] P. J. Schuck, D. P. Fromm, A. Sundaramurthy, G. S. Kino, and W. E. Moerner, *Improving the mismatch between light and nanoscale objects with gold bowtie nanoantennas*, Phys. Rev. Lett. **94**, 017402 (2005).

[176] J. N. Farahani, D. Pohl, H.-J. Eisler, and B. Hecht, *Single quantum dot coupled to a scanning optical antenna: A tunable superemitter*, Phys. Rev. Lett. **95**, 017402 (2005).

[177] S. Berweger, J. M. Atkin, R. L. Olmon, , and M. B. Raschke, *Adiabatic tip-plasmon focusing for nano-Raman spectroscopy*, J. Phys. Chem. Lett. **1**, 3427 (2010).

[178] A. Weber-Bargioni, A. Schwartzberg, M. Cornaglia, A. Ismach, J. J. Urban, Y. Pang, R. Gordon, J. Bokor, M. B. Salmeron, D. F. Ogletree, P. Ashby, S. Cabrini, and P. J. Schuck, *Hyperspectral nanoscale imaging on dielectric substrates with coaxial optical antenna scan probes*, Nano Lett. **11**, 1201 (2011).

[179] N. R. Wilson and J. V. Macpherson, *Carbon nanotube tips for atomic force microscopy*, Nat. Nanotechnol. **4**, 483 (2009).

[180] D. Hoch, Master's thesis, Technische Universität München, 2015.

[181] D.-C. Chen, *Portable alignment device for an off-axis parabolic mirror optical axis adjustment*, Int. J. Precis. Eng. Manuf. **13**, 33 (2012).

[182] Y. H. Lee, *Alignment of an off-axis parabolic mirror with two parallel He-Ne laser beams*, Opt. Eng. **31**, 2287 (1992).

[183] D. Roy, C. M. Williams, and K. Mingard, *Single-crystal gold tip for tip-enhanced Raman spectroscopy*, J. Vac. Sci. Technol. B **28**, 631 (2010).

[184] Z. C. Feng, A. J. Mascarenhas, W. J. Choyke, and J. A. Powell, *Raman scattering studies of chemical-vapor-deposited cubic SiC films of (100) Si*, J. Appl. Phys. **64**, 3176 (1988).

[185] C. Ambrosch-Draxl, H. Auer, R. Kouba, and E. Y. Sherman, *Raman scattering in $YBa_2Cu_3O_7$: A comprehensive theoretical study in comparison with experiments*, Phys. Rev. B **65**, 064501 (2002).

[186] H. Kezuka, T. Masaki, N. Hosokawa, K.Hirata, and K. Ishibashi, *Refractive index of high-T_c YBCO superconductors*, Physica C: Superconductivity **185**, 999 (1991).

[187] T. Deschamps, A. Kassir-Bodon, C. Sonneville, J. Margueritat, C. Martinet, D. de Ligny, A. Mermet, and B. Champagnon, *Permanent densification of compressed silica glass: a Raman-density calibration curve*, J. Phys.: Condens. Matter **25**, 025402 (2013).

[188] N. Chelwani, D. Hoch, D. Jost, B. Botka, J.-R. Scholz, R. Richter, M. Theodoridou, F. Kretzschmar, T. Böhm, K. Kamarás, and R. Hackl, *Off-axis parabolic mirror optics for polarized Raman spectroscopy at low temperature*, Appl. Phys. Lett. **110**, 193504 (2017).

[189] A. Perali, C. Castellani, C. D. Castro, and M. Grilli, *d-wave superconductivity near charge instabilities*, Phys. Rev. B **54**, 16216 (1996).

[190] C. Pfleiderer, *Superconducting phases of f-electron compounds*, Rev. Mod. Phys. **81**, 1551 (2009).

[191] E. Fradkin, S. A. Kivelson, and J. M. Tranquada, *Colloquium: Theory of intertwined orders in high temperature superconductors*, Rev. Mod. Phys. **87**, 457 (2015).

[192] P. Dai, *Antiferromagnetic order and spin dynamics in iron-based superconductors*, Rev. Mod. Phys. **87**, 855 (2015).

[193] D. J. Scalapino, *A common thread: The pairing interaction for unconventional superconductors*, Rev. Mod. Phys. **84**, 1383 (2012).

[194] M. Guarise, B. D. Piazza, M. M. Sala, G. Ghiringhelli, L. Braicovich, H. Berger, J. N. Hancock, D. van der Marel, T. Schmitt, V. N. Strocov, L. J. P. Ament, J. van den Brink, P.-H. Lin, P. Xu, H. M. Rønnow, and M. Grioni, *Measurement of magnetic excitations in the two-dimensional antiferromagnetic $Sr_2CuO_2Cl_2$ insulator using resonant X-ray scattering: Evidence for extended interactions*, Phys. Rev. Lett. **105**, 157006 (2010).

[195] B. D. Piazza, M. Mourigal, M. Guarise, H. Berger, T. Schmitt, K. J. Zhou, M. Grioni, and H. M. Rønnow, *Unified one-band Hubbard model for magnetic and electronic spectra of the parent compounds of cuprate superconductors*, Phys. Rev. B **85**, 100508(R) (2012).

[196] M. Rübhausen, O. A. Hammerstein, A. Bock, U. Merkt, C. T. Rieck, P. Guptasarma, D. G. Hinks, and M. V. Klein, *Doping dependence of the electronic interactions in Bi-2212 cuprate superconductors: Doped antiferromagnets or antiferromagnetic Fermi liquids?*, Phys. Rev. Lett. **82**, 5349 (1999).

[197] A. M. Zhang, J. H. Xiao, Y. S. Li, J. B. He, D. M. Wang, G. F. Chen, B. Normand, Q. M. Zhang, and T. Xiang, *Two-magnon Raman scattering in $A_{0.8}Fe_{1.6}Se_2$ systems (A=K, Rb, Cs and Tl): Competition between superconductivity and antiferromagnetic order*, Phys. Rev. B **85**, 214508 (2012).

[198] G. H, N. H. Sung, M. Höppner, B. J. Kim, B. Keimer, and M. L. Juan, *Two-Magnon Raman Scattering and Pseudospin-Lattice Interactions in Sr_2IrO_4 and $Sr_3Ir_2O_7$*, Phys. Rev. Lett. **116**, 136401 (2016).

[199] F. Michaud, F. Vernay, and F. Mila, *Theory of inelastic light scattering in spin-1 systems: Resonant regimes and detection of quadrupolar order*, Phys. Rev. B **84**, 184424 (2011).

[200] W. Prestel, Phd thesis, Technische Universität München, 2012.

[201] W. E. Pickett, *Electronic structure of the high-temperature oxide superconductors*, Rev. Mod. Phys. **61**, 433 (1989).

[202] E. Dagotto, *Correlated electrons in high-temperature superconductors*, Rev. Mod. Phys. **66**, 763 (1994).

[203] R. Hackl and W. Hanke, *Towards a better understanding of superconductivity at high transition temperatures*, Eur. Phys. J. Special Topics **188**, 3 (2010).

[204] A. Damascelli, Z. Hussain, and Z. X. Shen, *Angle-resolved photoemission studies of the cuprate superconductors*, Rev. Mod. Phys. **75**, 473 (2003).

[205] D. C. Johnston, J. P. Stokes, D. P. Goshorn, and J. T. Lewandowski, *Influence of oxygen defects on the physical properties of* La_2CuO_{4-y}, Phys. Rev. B **36**, 4007 (1987).

[206] T. Timusk and B. Statt, *The pseudogap in high-temperature superconductors: an experimental survey*, Rep. Prog. Phys. **62**, 61 (1999).

[207] B. Keimer, A. Aharony, A. Auerbach, R. J. Birgeneau, A. Cassanho, Y. Endoh, R. W. Erwin, M. A. Kastner, and G. Shirane, *Néel transition and sublattice magnetization of pure and doped* La_2CuO_4, Phys. Rev. B **45**, 7430 (1992).

[208] H. Das and T. S. Dasgupta, *Electronic structure of* La_2CuO_4 *in the T and T' crystal structures using dynamical mean field theory*, Phys. Rev. B **79**, 134522 (2009).

[209] T. Böhm, Master's thesis, Technische Universität München, 2012.

[210] P. W. Anderson, *New approach to the theory of superexchange interactions*, Phys. Rev. **115**, 2 (1959).

[211] N. S. Headings, S. M. Hayden, R. Coldea, and T. G. Perring, *Anomalous high-energy spin excitations in the high-*T_c *superconductor-parent antiferromagnet* La_2CuO_4, Phys. Rev. Lett. **105**, 247001 (2010).

[212] R. R. P. Singh, P. A. Fleury, K. B. Lyons, and P. E. Sulewski, *Quantitative determination of quantum fluctuations in the spin-1/2 planar antiferromagnet*, Phys. Rev. Lett. **62**, 2736 (1989).

[213] D. Reznik, P. Bourges, H. F. Fong, L. P. Regnault, J. Bossy, C. Vettier, D. L. Milius, I. A. Aksay, and B. Keimer, *Direct observation of optical magnons in* $YBa_2Cu_3O_{6.2}$, Phys. Rev. B **53**, R14741 (1996).

[214] A. W. Sandvik, S. Capponi, D. Poilblanc, and E. Dagotto, *Numerical calculations of the B_{1g} Raman spectrum of the two-dimensional Heisenberg model*, Phys. Rev. B **57**, 8478 (1998).

[215] A. A. Katanin and A. P. Kampf, *Theoretical analysis of magnetic Raman scattering in La_2CuO_4: Two-magnon intensity with the inclusion of ring exchange*, Phys. Rev. B **67**, 10040 (2003).

[216] T. Tohyama, H. Onodera, K. Tsutsui, and S. Maekawa, *Resonant two-magnon Raman scattering and photoexcited states in two-dimensional Mott insulators*, Phys. Rev. Lett. **89**, 257405 (2002).

[217] S. Chakravarty, B. I. Halperin, and D. R. Nelson, *Low-temperature behavior of two-dimensional quantum antiferromagnets*, Phys. Rev. Lett. **60**, 1057 (1988).

[218] D. Pekker and C. Varma, *Amplitude/Higgs modes in condensed matter Physics*, Ann. Rev. Cond. Mat. Phys. **6**, 269 (2015).

[219] P. W. Higgs, *Broken symmetries and the masses of gauge bosons*, Phys. Rev. Lett. **13**, 508 (1964).

[220] M. Endres, T. Fukuhara, D. Pekker, M. Cheneau, P. Schauss, C. Gross, E. Demler, S. Kuhr, and I. Bloch, *The Higgs amplitude mode at the two-dimensional superfluid/Mott insulator transition*, Nature **487**, 454 (2012).

[221] R. Sooryakumar and M. V. Klein, *Raman scattering by superconducting-gap excitations and their coupling to charge-density waves*, Phys. Rev. Lett. **45**, 660 (1980).

[222] P. B. Littlewood and C. M. Varma, *Gauge-invariant theory of the dynamical interaction of charge density waves and superconductivity*, Phys. Rev. Lett. **47**, 811 (1981).

[223] T. Cea and L. Benfatto, *Nature and Raman signatures of the Higgs amplitude mode in the coexisting superconducting and charge-density-wave state*, Phys. Rev. B **90**, 224515 (2014).

[224] C. Rüegg, B. Normand, M. Matsumoto, A. Furrer, D. F. McMorrow, K. W. Krämer, H. U. Güdel, S. N. Gvasaliya, H. Mutka, and M. Boehm, *Quantum magnets under pressure: Controlling elementary excitations in $TlCuCl_3$*, Phys. Rev. Lett. **100**, 205701 (2008).

[225] R. Matsunaga and R. Shimano, *Nonlinear terahertz spectroscopy of Higgs mode in s-wave superconductors*, Phys. Scr. **92**, 024003 (2017).

[226] S. Sugai, H. Suzuki, Y. Takayanagi, T. Hosokawa, and N. Hayamizu, *Carrier-density-dependent momentum shift of the coherent peak and the LO phonon mode in p-type high-T_c superconductors*, Phys. Rev. B **68**, 184504 (2003).

[227] M. V. Klein and S. B. Dierker, *Theory of Raman scattering in superconductors*, Phys. Rev. B **29**, 4976 (1984).

[228] T. P. Devereaux and A. P. Kampf, *Raman scattering in cuprate superconductors*, International Journal of Modern Physics B **11**, 2093 (1997).

[229] E. Y. Sherman, O. V. Misochko, and P. Lemmens, in *Spectroscopy of high-T_c superconductors: A theoretical view*, edited by N. Plakida (Taylor and Francis, London, ADDRESS, 2003).

[230] A. Erb, E. Walker, and R. Flükiger, *$BaZrO_3$: the solution for the crucible corrosion problem during the single crystal growth of high-T_c superconductors $REBa_2Cu_3O_{7-\delta}$: RE=Y, Pr*, Physica C **245**, 245 (1995).

[231] A. Erb, E. Walker, and R. Flükiger, *The use of $BaZrO_3$ crucibles in crystal growth of the high-T_c superconductors progress in crystal growth as well as in sample quality*, Physica C **258**, 9 (1996).

[232] C. Kendziora, M. C. Martin, J. H. anb L. Mihaly, and L. Forro, *Wide-range oxygen doping of $Bi_2Sr_2CaCu_2O_{8+\delta}$*, Phys. Rev. B **48**, 3531 (1993).

List of publications

1. **N. Chelwani**, D. Hoch, D. Jost, B. Botka, J.-R. Scholz, R. Richter, M. Theodoridou, F. Kretzschmar, T. Böhm, K. Kamarás & R. Hackl. Off-axis parabolic mirror optics for polarized Raman spectroscopy at low temperature. *Appl. Phys. Lett.* **110**, 193504 (2017).

2. **N. Chelwani**, A. Baum, T. Böhm, M. Opel, F. Venturini, L. Tassini, A. Erb, H. Berger, L. Forró, & R. Hackl. Magnetic excitations and amplitude fluctuations in insulating cuprates. *Phy. Rev. B* **97**, 024407 (2018).

Acknowledgment

During my PhD tenure at the Walther-Meissner-Institute, I have gained an amazing experience. The presented work would have not been possible without the contribution from numerous people. I would like to take this opportunity to express my gratitude, in particular, to:

- *Prof. Dr. Rudolf Gross* for being a great doctoral advisor. Thank you very much for giving me the opportunity to pursue my PhD at the Walther-Meissner-Institute. I value your support and guidance throughout my stay at the WMI.

- *Dr. Rudi Hackl* for being a supportive supervisor. Your valuable guidance and the art to deal with the problems have always motivated me to work with the most challenging project. Your magnanimous time and appreciation were sometimes all that kept me going and making progress with the TERS setup. Thank you for making me a part of the Raman group and sharing your experiences and knowledge with me. I will cherish all your personal and professional support for the lifetime.

- My former and current group members *Dr. Bernhard Muschler, Dr. Hans-Martin Eiter, Dr. Florian Kretzschmar, Dr. Bea Botka, Dr. Thomas Böhm, Andreas Baum, Daniel Jost, Andreas Walter, Michael Rehm, and Ramez Hossenian Ahangharnejhad* for the pleasant atmosphere in the Raman group and for many productive discussions.

- *David Hoch, Roland Richter,* and *Maria Theodoridou* for their important contributions to this dissertation via their master and bachelor theses. My special thanks to *David Hoch* for being a great companion during the TERS mission.

- *Prof. Dr. Andreas Erb* for providing the samples and the facilities to anneal the samples in the crystal laboratory.

- *Dr. Matthias Opel* for his help in sorting the old data of YBCO sample and for arranging many get-together events in WMI.

- Colleagues from other groups, in particular, *Dr. Frank Deppe, Dr. Stephan Geprägs, Dr. Mathias Althammer, Peter Eder, and Max Häberlein* for their help in every possible way and creating positive atmosphere. I thoroughly enjoyed talking with all of you personally at different occasions.

- *Dr. Katalin Kamarás* for providing me the initial platform to gain knowledge in the field of spectroscopy. Thank you very much for taking utmost care regarding my comfortable stay in Budapest.

- My group members from the Wigner Research Centre for Physics, in particular, *Dr. Zsolt Szekrényes*, *Dr. Áron Pekker*, *Dr. Éva Kováts*, *Dr. Hajnalka Mária Tóháti*, and *Dr. Katalin Németh* for gracefully accommodating me in their research group. Special thanks to *Dr. Zsolt Szekrényes* for his help in the administrative tasks.

- *Prof. Dr. B. S. Chandrasekhar* for his willingness to help me in any possible ways. I appreciate your time to go through the first draft of my thesis.

- *Dr. Toni Helm* for always being a caring friend. Thank you very much Toni for taking timely updates regarding my progress and always assuring me that everything will be fine.

- *Dr. Christoph Zollitsch* for being a trustworthy friend and listening to me patiently. I always felt comfortable sharing my thoughts with you especially at the end of thesis.

- Colleagues from the workshop for their support and useful advice regarding our TERS setup.

- *Ulrich Guggenberger* for sharing his knowledge and ideas related to electronics and allowing me to use various electronic devices for our customized TERS system.

- *Emel Dönertas* and *Ludwig Ossiander* for their guidance to complete the administrative formalities with ease.

- *Sybilla Plöderl* and *Maria Botta* for their time during the coffee breaks to discuss about the world beyond physics.

- Dearest *Bhagwanji* and *Didiji*, my fervent gratitude towards your consistent support and eternal love. You have been my utmost pillar of strength, energy, and positivity whenever I got weary. You have taught me to salute the time by moving on in life. Thank you for making me realize that a certain darkness is necessary for the stars to shine. I dedicate this thesis to you and your pious blessings.

- My loving parents *Brijlal Chelwani* and *Poonam Chelwani*, brother *Neelesh,* sister-in-law *Sampana,* sister *Naina,* brother-in-law *Jatin,* and my nephew *Anant* for their everlasting love and care. I believe whatever I am today is because of you all. Your love has made me to overcome all the challenges of life. Thank you very much for spreading positivity around me.

- My dear parents-in-law for their love and moral support. Thank you very much for your constant encouragement which has helped me to reach to this stage.

- Finally, and most of all, I would like to take this chance to express my gratitude towards my wife *Mahima* and our little angel *Vedanshi*. Mahima, thank you very much for your unconditional love and encouragement. Your immense patience and understanding have supported me to complete this research work. Vedanshi, thank you for coming into our lives. During this time, your presence has helped me to see the brighter side of every situation. You really are precious to me. Stay blessed!